Temporal Variability Processes in Discs and Shells around Compact Objects

CAMK PAN

Author: Ananda Deepika Bollimpalli

Advisor: Prof. Włodzimierz Kluźniak

CENTRUM ASTRONOMICZNE IM. MIKOŁAJA KOPERNIKA
POLSKIEJ AKADEMII NAUK

A thesis submitted in partial fulfillment of the requirements for the degree of
Doctor of Philosophy
in
Astronomy

July, 2020

Dedicated to
My family for making me who I am today.

Abstract

Compact objects – white dwarfs, neutron stars and black holes – are the brightest lighthouses in the cosmos serving as a navigational aid for astronomers on their journey to understand the depths of the Universe. In this thesis, we investigate the origins of the various variability features observed in accretion discs and shells present around the compact objects. For this, we adapt analytic, semi-analytical and general relativistic magnetohydrodynamical (GRMHD) simulations approaches, based on what best suits the problem.

In Paper I, we explore the disc-instability outbursts in two Symbiotic star (SS) systems, RS Oph and Z And, which have white dwarfs as the accreting object. Using a one dimensional (1D) semi-analytic code, we study the thermal and viscous evolution of large size, standard thin discs present in these systems. Our findings suggest that (i) The disc-instability outbursts could trigger the recurrent novae observed in these systems, thereby causing the short recurrence time scales observed in these systems (ii) The 'combination nova' mechanism proposed for the observed outbursts in Z And can be ruled out and instead the mass-transfer enhancement from the secondary could be the key.

In Paper II and Paper III, we perform a purely analytical study of the radial oscillations of levitating atmospheres around near-Eddington luminous neutron stars, with possible relevance to the burst oscillations observed during the Type-I X-ray bursts. In these two papers, we found that (i) the eigenfrequencies of these oscillations typically lie within 300–600 Hz, i.e., the observed range of burst oscillation frequencies; (ii) radiation drag introduces a characteristic frequency maximum through damping of oscillations, which plays a vital role in determining the stellar parameters; (iii) given the luminosity and the flux observations, we can estimate the mass and radius of the neutron star to within a few percent accuracy and determine the distance to the source to less than one percent error. The errors are remarkably small, compared to the estimates from any other currently available methods and therefore can potentially put better constraints on the equation of state.

In Paper IV, we use GRMHD simulations to investigate the aperiodic variability observed in the black hole binaries over a wide range of time scales – a few milliseconds to seconds. Theoretical models explain this variability as the inward propagating fluctuations of mass accretion rate on viscous timescales, although confirmations from the numerical simulations of magnetized accretion flows are required for a better understanding of the underlying variability process. Using a set of five exceptionally long GRMHD simulations of geometrically thick, optically thin, black hole accretion flows as test-beds, we show evidence for the inward propagating fluctuations in these simulations by establishing strong radial coherence and reproducing the other observed variability features – linear rms-flux relation, lognormal distribution of flux, and frequency-dependent time lags between different energy bands.

Streszczenie

(Abstract in Polish)

Obiekty zwarte – białe karły, gwiazdy neutronowe i czarne dziury – są najjaśniejszymi "latarniami morskimi" w kosmosie, służące astronomom jako pomoc nawigacyjna podczas ich podróży ku zrozumieniu głębi Wszechświata. W tej pracy badamy pochodzenie różnych cech zmienności obserwowanych w dyskach akrecyjnych i powłokach obecnych wokół obiektów zwartych. W tym celu stosujemy rachunki analityczne, półanalityczne i symulacje magnetohydrodynamiczne w ogónej teorii względności (GRMHD, ang.: general relativistic magnetohydrodynamics), opierając się na tym, co najlepiej pasuje do problemu.

W Paper I, analizujemy wybuchy powodowane niestabilnościami dysku akrecyjnego w dwóch gwiazdach symbiotycznych (SS, ang.: symbiotic star), RS Oph i Z And, w których obiektem akreującym są białe karły. Używając jednowymiarowego (1D) kodu półanalitycznego, badamy ewolucję termiczną i lepką dużych, standardowych, cienkich dysków akrecyjnych obecnych w tych systemach. Nasze odkrycia sugerują, że (i) wybuchy powodowane niestabilnościami dysku akrecyjnego mogą wywołać nowe powrotne obserwowane w tych układach, powodując tym samym krótkie skale czasowe wybuchów obserwowanych w tych układach (ii) mechanizm „nowej kombinacyjnej" (ang.: combination nova) zaproponowany dla obserwowanych wybuchów w Z And można odrzucić, a zamiast tego kluczowe może być zwiększenie transferu masy z towarzysza.

W Paper II i Paper III, przeprowadzamy całkowicie analityczne badania oscylacji radialnych atmosfer lewitujących wokół świecących prawie-Eddingtonowsko gwiazd neutronowych, z możliwym odniesieniem do tzw. oscylacji wybuchów (ang.: burst oscillations) obserwowanych podczas rozbłysków rentgenowskich typu I. W tych dwóch pracach stwierdziliśmy, że (i) częstości własne tych oscylacji zazwyczaj mieszczą się w zakresie 300–600 Hz, co odpowiada obserwowanemu zakresowi częstotliwości oscylacji wybuchów towarzyszących rozbłyskom rentgenowskm typu I; (ii) opór promieniowania wprowadza charakterystyczne maksimum częstotliwości poprzez tłumienie oscylacji, co odgrywa istotną rolę w określaniu parametrów gwiazd; (iii) biorąc pod uwagę jasność i obserwacje strumienia promieniowania, możemy oszacować masę i promień gwiazdy neutronowej z kilkunastoprocentową dokładnością i określić odległość do źródła z błędem mniejszym niż jeden procent. Te błędy pomiaru są niezwykle małe w porównaniu z oszacowaniami otrzymywanymi z innych obecnie dostępnych metod, a zatem mogą potencjalnie lepiej ograniczać równanie stanu.

W Paper IV, używamy symulacji GRMHD do badania aperiodycznej zmienności obserwowanej w czarnych dziurach w układach podwójnych w szerokim zakresie skal czasowych – od kilku milisekund do sekund. Modele teoretyczne wyjaśniają tę zmienność jako unoszone przez przepływ fluktuacje tempa akrecji w lepkościowych skalach czasowych, chociaż dla lepszego zrozumienia fundamentalnego procesu zmienności wymagane jest potwierdzenie tej hipotezy w symulacjach numerycznych magnetohydrodynamicznych przepływów akrecyjnych. Używając zestawu pięciu wyjątkowo długich symulacji GRMHD geometrycznie grubych, optycznie cienkich, przepływów akrecyjnych wokół czarnej dziury do przetestowania modelu teoretycznego, pokazujemy dowody na propagację w kierunku czarnej dziury fluktuacji w tych symulacjach takie jak ustanowienie silnej koherencji radialnej i odtworzenie innych obserwowanych cech zmienności – liniowego związku między średnią dyspersją (rms, ang.: root mean square) a strumieniem promieniowania, normalnego rozkładu logarytmu strumienia, oraz zależnych od częstotliwości opóźnień czasowych między różnymi pasmami energii.

Acknowledgements

Contents

Part I

Introduction

Chapter 1

Introduction

Watching the night sky blazing with stars is surely fun and has always fascinated humans. Even before the invention of the telescope, humans have discovered that not all of the stars shine steadily and the night sky is highly variable, e.g., stars periodically change brightness over time (variable star, Mira), and sudden brightening events like supernovae (SN 1006, SN 1054 that produced the Crab Nebula, SN 1572 in Cassiopeia observed by Tycho Brahe [1], [2]). Under the "typical" dark sky conditions, our naked eye can only see stars with brightness up to +6 apparent magnitude[1], and only in the spectral range of 400-800 nm, i.e the optical part of the electromagnetic spectrum. The night sky harbours many other objects which emit enormous energy in the high spectral end – UV, X-rays and γ-rays. The first X-ray satellite *Uhuru* discovered the now famous X-ray emitting black hole, Cygnus X-1. This source was unknown to mankind, although its location in the sky is close to the bright star $\eta - Cygni$ of the northern constellation *Cygnus*, known since the second century. With advancing telescope technology, many more observations of bright sources and their bewildering variety of variability are discovered, leaving more puzzles for astronomers and a growing need for theoretical models that go hand-in-glove with the observations. Now, at the dawn of the multi-messenger era, it is at least widely accepted that the rapidly variable, highly-energetic events are always associated with compact objects (white dwarfs, neutron stars, and black holes). In the four published articles that constitute this thesis, we attempt to model and understand the various kinds of time variability observed in the compact object systems – periodic, quasi-periodic, aperiodic – in the light of accretion discs and shells around these objects.

In this chapter, we start with a brief introduction to the compact objects and the broad classification of binary systems in which they are found (Section 1.1). We then discuss the different types of time variability observed in the light curves of these systems, which sets the background for the motivation of this thesis work (Section 1.2). Since accretion is the main source of power in these binaries, we provide an overview of accretion process (Section 1.3) and then briefly discuss the physical processes in the accretion discs that cause the observed time variability. We also discuss the shells that could form around the compact stars under special circumstances and their role in inducing time variability in the observed light curves. With the motivation of this thesis at hand, we conclude this chapter with an overview of the other chapters that contain published works (Section 1.5).

---

[1] A measure of the brightness of an object when observed from the Earth, with brighter objects having lower magnitude, e.g., the Sun's apparent magnitude is -26.74 [3].

1.1 Compact objects

Compact objects – white dwarfs, neutron stars and black holes – are the remnants of stellar evolution, created when nuclear fuel can no longer generate enough thermal pressure to resist gravitational collapse. While white dwarfs are supported by the degenerate pressure of electrons, the neutron degeneracy pressure balances the gravitational forces in the neutron stars. If the star finds no means to resist the gravitational pull, it collapses into a singularity, forming a black hole. With masses comparable to normal stars yet with extremely small radii, compact objects have high compactness (quantified as M/R). Their high surface potentials imply that gravity plays an important role, and the general relativistic effects are significant, particularly for neutron stars and black holes. Because of their high compactness and large densities, understanding the nature of these objects and their interior structures helps us improve our knowledge of the fundamental forces of interactions of matter. For more details on compact objects, refer to [4].

Excluding the supermassive black holes at the centers of galaxies, the majority of compact objects detected exist in gravitationally bound binary systems, where the compact object together with its companion star orbit a common center of mass. The companion star could be a main-sequence star or an evolved star, or another compact object. Due to the gravity of the compact object, matter may be transferred from the companion to the compact object through a process called accretion. We now know that the majority of bright compact object binaries and the supermassive black holes at the galactic centers are powered by accretion. A common way of mass transfer from the companion is through Roche lobe overflow in which matter is transferred through a Lagrangian point when the companion fills its Roche lobe. This can happen either when the companion star swells up or when the two components approach each other. Another way of mass transfer is through stellar winds that drive away matter from the companion star's surface, which are then captured by the compact object.

In general, based on the nature of the compact object and the companion star, the close binary systems can be classified and sub-classified into the following:

- **Cataclysmic variable (CV)**. These are semi-detached binary systems with a companion star (typically a late-type main sequence star or a brown dwarf) transferring matter to an accreting white dwarf through Roche-lobe overflow. Accretion flow in these systems is well modeled by standard thin discs (see Section 1.3.1). The typical orbital periods of CVs lie between 1-10 hours[2] and thereby these systems harbour small discs ($\sim 10^{10}$–10^{11} cm in radial extent).

- **Symbiotic Star (SS)**. Symbiotic binaries or SSs are the widest interacting binary systems known, with the white dwarf or neutron star accreting from a red giant companion, either through stellar wind or via Roche lobe overflow [5]. The orbital periods of symbiotic stars range from years to decades, with the possible standard thin disc sizes of $\sim 10^{12} - 10^{13}$ cm.

  - **Burning SS**. These are SSs in which white dwarfs maintain quasi-steady luminosity ($\sim 10^3 L_\odot$, Mürset, Nussbaumer, Schmid, *et al.* [6]) by stably burning hydrogen on their envelopes, i.e, hydrogen is burnt at the same rate as it is accreted. Most of the classical symbiotic stars fall under this category (e.g., Z And).

  - **Non-burning SS**. In cases where the hydrogen is accreted at a rate lower than its steady burning rate, hydrogen simply accumulates on the surface, until a thermonuclear runaway

---

[2]Note that a period gap exists between 2 and 3 hours, where only a small number of CVs are detected.

is triggered. With no shell burning, the persistent luminosity of the white dwarfs in these systems is generated from accretion (given by equation 1.2). Some examples include symbiotic recurrent novae (such as RS Oph, T CrB in their quiescence state) and jet-producing binaries (e.g., CH Cyg and R Aqr).

- **X-ray binary (XRB)**. In these binary systems, the compact object is a neutron star or black hole, while the companion can be a main sequence star, supergiant or a white dwarf. The typical luminosities of these sources are around 10^{34-38} erg/sec, constituting the majority of bright X-ray sources in the Galaxy. Historically, X-ray binaries have been further classified into two types based on the mass of the donor [7], [8]:

  - **Low-mass X-ray binary (LMXB)** is an XRB with a companion star (usually K or M type stars or a white dwarf) of mass $\lesssim 1 M_\odot$. In this case, mass transfer occurs via Roche lobe overflow, leading to the formation of an accretion disc. The generally observed spectra of LMXBs show blackbody like radiation, indicating a thin disc, but some LMXBs, particularly ones with an accreting black hole in low-luminosity states, are dominated by the non-thermal component, suggesting an ADAF structure (see Section 1.3.1).

  - **High-mass X-ray binary (HMXB)** is an XRB with companion star (usually O type or B type stars) of mass $\gtrsim 10 M_\odot$. Most of these systems are wind-fed accretors, but some binaries have mass transfer through Roche-lobe overflow. Well known examples include Cygnus X-1, a black hole HMXB and Cen X-3, an X-ray pulsar. There are also a handful of XRBs, whose Roche-lobe filling companions have mass within $1-3\ M_\odot$, and are refereed to as Intermediate Mass X-ray Binaries (IMXBs).

  Recent discoveries have identified a subclass of HMXBs whose luminosities (assuming isotropic emission) are comparable to or above the Eddington limit of stellar mass black holes ($\sim 10^{39}$ erg/sec). These sources are called Ultraluminous X-ray sources (ULXs), and their high luminosities are thought to be produced mostly from super-Eddington accretion onto stellar mass objects. A handful of the ULXs detected so far (e.g., NGC 7793 P13, NGC 5907, NGC 300 ULX1) also show pulsations, suggesting that the accretor is a neutron star. Detailed review on ULXs is available in Kaaret, Feng, and Roberts [9] and Atapin [10].

1.2 Types of temporal variability

An important property of these compact object binaries is the wide range of intensity variations (a few to several orders of magnitude) observed over an enormous range of timescales in almost the entire range of electromagnetic spectrum. A detailed analysis of the timing properties in various energy bands provides a great extent of information about the nature of the accreting object and its physical environment. Thus, timing analysis has become a vital tool in the study of the compact object systems. Below we discuss some of the important variability phenomena commonly observed in these systems.

1.2.1 Outbursts

Many disc-accreting systems such as CVs and LMXBs exhibit outbursts that recur at regular intervals. During these outbursts the intensity of the light curve increases by few orders of magnitude. Depending on the nature of the compact object and the triggering mechanism, the duration of the outburst and the recurrence time-scales vary. A major fraction of CVs undergo dwarf-novae outbursts, which have a brightness amplitude of around 2-5 magnitude and last between a few days to 20 days, with a recurrence period of 10 days to few years. It is now widely accepted that the triggering mechanism for these outbursts is the disc instability (see Lasota [11] and references therein). The same mechanism is also known to cause outbursts in neutron star and black hole LMXBs with the typical outburst and recurrence timescales varying between few months to years (called soft X-ray transients, McClintock and Remillard [12]). More details on the disc instability model are provided in the next section (1.3.2).

Nuclear burning of H/He on the surface of the compact objects can also trigger outbursts. The best known examples among white dwarfs are recurrent novae outbursts in SSs (e.g., outbursts in RS Oph, T CrB), with 2 to 10 magnitudes of brightness amplitude, that last for several days, and recur at at a rate of 10–100 years [13]. These outbursts are thought to be powered by the thermonuclear runaway on the surface of the accreting white dwarfs, where the increasing temperatures due to the hydrogen nuclear burning in turn boosts up the nuclear burning rate. However, it is not completely understood how the white dwarf accretes enough mass required to trigger thermonuclear runaway in such short recurrence times. The same thermonuclear runaway also triggers Classical Novae (Symbiotic Novae) outbursts that are single observed eruptions in CVs (SSs) with 6 to 19 magnitudes of brightness amplitude that lasts from several days to years. A rather poorly understood class of outbursts are classical symbiotic outbursts (or Z And type) that occur in successions of a few, non-uniform eruptions, separated by long recurrence periods (~ 10 yr) and have optical amplitudes of several magnitudes. The origin of the outbursts is not yet clear, but the currently existing models include a sudden increase in the mass transfer rate from the red giant [14], photospheric expansion of the white dwarf surface [15], shell flashes [16] and accretion disc-instability [17], or a combination of both [18].

Most neutron star LMXBs consisting of a weakly magnetized neutron star (magnetic field of the order of $\sim 10^8$ G), exhibit 'bursting' behaviour, in which their X-ray luminosity increase by an order of magnitude. Such events, termed as X-ray bursts, are categorized into two classes: Type-I and Type-II [19]. Type-I X-ray bursts are characterized by a rapid rise in intensity followed by a slow decline, lasting for $\sim 10 - 100$ seconds. Even in the period between the bursts (typically a few hours to days), these sources produce persistent X-ray emission. Type-I X-ray bursts, are also called as thermonuclear bursts as they are produced by thermonuclear flashes triggered on the surface of the neutron star [20]. Whereas, Type-II bursts are most likely caused by the changes in the accretion rate or thermal-viscous instabilities in the accretion disc [21]. Thus the Type-I and Type-II X-ray bursts share similarities with the recurrent novae and dwarf novae outbursts, respectively.

1.2.2 Burst Oscillations

During the Type-I X-ray bursts, neutron stars often reach Eddington luminosities [19]. The Fourier-timing analysis of these bursts show large amplitude, high coherence oscillations in X-ray brightness with frequencies in the 300–600 Hz range, termed as burst oscillations [22]. These oscillations are commonly detected during the decay phase of the outburst, however they can also be observed at other times, i.e., rise or peak [20]. In most burst oscillation sources, as the burst progresses, an increasing

frequency drift by a few Hz is observed as the flux decreases during the outburst decay. It is generally agreed that the burst oscillations in the rise phase are due to the rotational modulation of the hot spot corresponding to flame propagation on the stellar surface. However, there is no clear understanding on the origin of the oscillations in the decay phase (see for example, Watts [23] for a detailed review on burst oscillations). In Chapters 2 and 3 we explore another possibility of understanding the frequencies of burst oscillations, particularly related to the outburst tail, in the context of the radial oscillations of 'levitating atmospheres'.

1.2.3 Broad-band variability

The X-ray light curves of XRBs, particularly in the low-luminosity hard states, are dominated by strong, aperiodic variability (flicker-type noise) on time-scales of milliseconds to seconds [24]. The power spectrum shows a continuous band of power present over a wide range of frequencies, that varies inversely with the frequency. The observed light-curves also display various characteristic features like a log-normal distribution and a linear rms-flux relation, which indicate that the underlying variability process is stochastic and multiplicative in nature. The variability is thought to be intrinsic to the accretion process. When comparing the light curves measured in two different energy bands, say hard (typically for photon energies $\gtrsim 2$ keV) and soft ($\sim 0.1 - 2$ keV) energy bands, one may notice the following features. (i) Strong coherence which drops off at higher frequencies, and (ii) positive time lags (few milliseconds to few seconds for a typical stellar mass black hole) which are also frequency-dependent. These features are well explained by a phenomenological model based on the inward propagating fluctuations of mass accretion rate, but much remains puzzling about what drives these fluctuations (see section 1.3.3). It is worth noting that similar broad-band variability is also observed in other accreting systems in other spectral ranges: neutron star systems (in X-rays [25]), accreting white dwarfs (in optical/UV band [26], [27]) and young stellar objects (in IR/optical band [28]) .

In the following section, we review the basics of accretion and then discuss the details of the physical processes that trigger the outbursts, oscillations, and aperiodic variability.

1.3 Accretion onto compact objects

Accretion is a vital process in which the surrounding matter is gravitationally captured by the compact object. During this process, some of the gravitational potential energy of the accreting material is converted into radiative energy. The energy thus released by accretion of a mass m onto an object with mass M and radius R_* is

$$\Delta E = \eta m c^2, \tag{1.1}$$

where η is the radiative efficiency for accretion, depending on the compactness of the accreting object to within a factor of a few, $\eta \sim (G/c^2)M/R_*$. When compared to the energy released from the nuclear fusion reactions, with $\eta \sim 0.007$, the energy released in the accretion process onto a neutron star or black hole ($\eta \sim 0.1$) is much higher, making accretion one of the most efficient processes for energy release in the Universe. For white dwarfs ($\eta \sim 0.0002$), nuclear burning is more efficient, however, accretion plays a significant role on the observable timescales.

The simplest form of accretion would be a spherically symmetric, radial infall of matter onto the compact object in Newtonian gravity. In such a case, assuming that the entire energy of the infalling

material is radiated away at the accretor's surface, the accretion luminosity is given by

$$L_{\text{acc}} = \frac{GM\dot{M}}{R_*} = \eta\dot{M}c^2. \tag{1.2}$$

The radiated photons carrying momentum, exert an outward force on the surrounding gas. For a gas with opacity κ, the radiation force acting on the gas at a radius r from the center is given by

$$f_{\text{rad}} = \frac{L\kappa}{4\pi cr^2}, \tag{1.3}$$

The inward gravitational force on the gas (per unit mass) is GM/r^2, which exactly balances the outward radiation force, when the luminosity of the object reaches the Eddington limit:

$$L_{\text{Edd}} = \frac{4\pi cGM}{\kappa}. \tag{1.4}$$

For a fully ionized hydrogen gas, the opacity is mostly due to Thomson-electron-scattering ($\kappa \sim 0.4\,\text{cm}^2\,\text{g}^{-1}$), in which case $L_{\text{Edd}} \approx 1.3 \times 10^{38}(M/M_\odot)\,\text{erg/s}$. Following equation 1.2, the corresponding limit on the accretion rate is

$$\dot{M} \leq \dot{M}_{\text{Edd}} = \frac{L_{\text{Edd}}}{\eta c^2} \tag{1.5}$$

Note that equation 1.4 gives the luminosity limit in Newtonian gravity, in which both the gravitational and radiation force have the same radial dependence; thus the super-Eddington nature of the star is preserved at all radii. However, because of the gravitational redshift this is no longer the case in general relativity and we will discuss more about this in Section 1.4.

1.3.1 Accretion discs

In the case of close binary systems, matter ejected from the outer layers of the companion star already carries angular momentum. Thus, under the gravitational attraction of the compact object, matter is pulled towards the equatorial plane of the binary system, forming disc like structures – termed as accretion discs. The material in the disc spirals inwards as it looses its angular momentum due to the shear stresses caused by the viscosity and turbulent motion of the gas. Both the energy dissipated in this process of angular momentum transfer, and the compression of gas due to strong gravity heats up the matter, a fraction of which is radiated away. Most of the energy release happens close to the compact object, where all the stored gravitational binding energy of the accreted gas is released in the form of high-energy radiation, typically observed in X-rays. The illustration in Figure 1.1 captures all the key components of an interacting binary systems with accretion discs, like LMXBs, CVs and some SSs.

Our understanding of accretion physics came with the Shakura-Sunyaev model [29] which describes geometrically thin ($H/R << 1$) and optically thick ($\tau >> 1$) accretion discs at sub-Eddington mass accretion rates (i.e., $\dot{M} < \dot{M}_{\text{Edd}}$). Here H is the disc height at a radius R from the center, and τ is the optical depth. These discs are radiatively efficient, emitting thermal blackbody-like radiation. At further low accretion rates ($\dot{M} << \dot{M}_{\text{Edd}}$), the accretion flow becomes comparatively thick (still $H/R < 1$), and optically thin ($\tau << 1$), often referred to as advection-dominated accretion flows (ADAFs). On the other hand, for the higher mass accretion rates ($\dot{M} \gtrsim \dot{M}_{\text{Edd}}$), one can have geometrically thick and optically thick structures – advective discs (or slim discs, with H/R<1) and Polish doughnuts
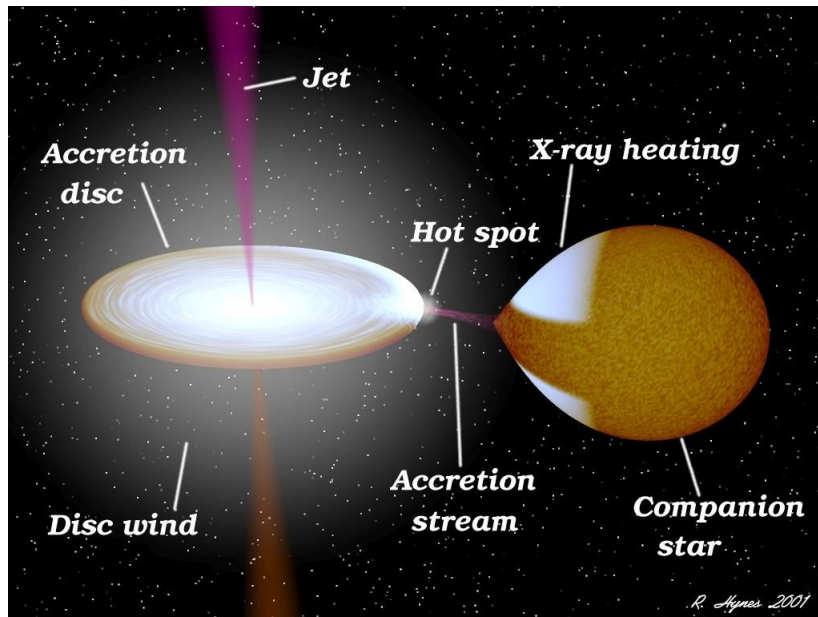
Figure 1.1: An artist impression of a low-mass X-ray binary, although accreting CVs and SSs look similar. Credit: NASA/ R. Hynes

(with H/R > 1). Further details on accretion discs can be found in Pringle [30] and Abramowicz and Fragile [31].

Most of the early-developed disc models for different accretion flows were based on the α-viscosity prescription, initially proposed by Shakura and Sunyaev [29] in their model to account for the unknown source of turbulence that aids in angular momentum transport. The model assumes that the shear stress is linearly related to the total pressure through a constant, viscosity parameter, α ($0 < \alpha < 1$). Years later, Balbus and Hawley [32] showed that the weakly magnetized plasma in accretion flows is susceptible to the magneto-rotational instability (MRI, [33]) that causes turbulence; thus providing the physical origin of stress from first principles. Since then a lot of work has gone into simulating different accretion flow structures of magnetized plasma based on MRI, for both Newtonian potential and in general relativity.

The behaviour of an accretion disc is mainly governed by three most important timescales – dynamical timescale, thermal timescale and viscous timescale.

- **Dynamical timescale,** $t_{\mathrm{dyn}} \sim R/v_\phi$, gives the orbital timescale of the disc. For geometrically thin discs, this also gives the timescale over which pressure force adjusts to hydrostatic equilibrium in the vertical direction ($\sim H/c_{\mathrm{s}} \sim R/v_\phi \sim t_{\mathrm{dyn}}$).

- **Thermal timescale,** $t_{\mathrm{th}} \sim \alpha^{-1} t_{\mathrm{dyn}}$, gives the timescale over which the disc re-adjusts back to thermal equilibrium, if dissipation rate is altered.

- **Viscous timescale** $t_{\mathrm{visc}} \sim \alpha^{-1}(H/R)^{-2} t_{\mathrm{dyn}}$, measures the timescale on which the local surface density in the disc varies.

Since $\alpha < 1$, and if $H/R < 1$, we have $t_{\mathrm{dyn}} < t_{\mathrm{th}} < t_{\mathrm{visc}}$. This clear difference in the timescales allows us to distinguish between different types of instabilities and oscillations that cause the various types of observed variability. For example, the disc-instability outbursts in CVs (see section 1.2.1) last for a few days, which is too long to be related to the dynamical or thermal timescales. The outburst periods are

mostly determined by the viscous timescales, which play a dominant role in the propagation of fronts in the disc-instability model (see Section 1.3.2). Similarly, the measured time lags between the hard and soft X-ray bands for the broad-band variability (see Section 1.2.3) can only be associated with the viscous timescales of stellar mass black holes and are thus well explained by the inward propagating fluctuations in the disc (see Section 1.3.3). These lags are on the order of few milliseconds, unlike in CVs, as the viscous timescale increases with mass and the disc extends to much smaller radii in black hole systems.

Although the standard thin disc model assumes that the discs are steady with radially uniform mass accretion rate, they are in fact susceptible to thermal and viscous instabilities. The thermal instability occurs when small perturbations in the disc temperature disrupt the energy balance, and the perturbations grow further on thermal timescales. Similarly, viscous instabilities occur when small perturbations in the surface density (or mass accretion rate) grow exponentially on viscous timescales. Standard thin discs with $H/R << 1$ are susceptible to both these instabilities which occur when rapid changes in opacity happen in a gas-pressure dominated disc. This scenario is well known to be responsible for the outbursts in dwarf novae and soft X-ray transients (discussed in section 1.2.1), and are well modeled by the disc-instability model which we describe below in section 1.3.2. Also, standard thin discs dominated by radiation-pressure are shown to be susceptible to thermal and viscous instabilities [34], [35]. However, recent numerical simulations have shown that a strong net magnetic flux in the disc can thermally stabilize the disc [36], [37] and significantly modify their vertical structure; such discs are referred to as 'elevated' or 'puffy' discs, which still have $H/R \lesssim 1$ but with dominant accretion of matter occurring above the disc midplane.

Another class of disc solutions with $H/R < 1$ are ADAFs (see, e.g., the review by Yuan and Narayan [38]). Unlike the standard thin discs, which are geometrically thin and optically thick, ADAFs are geometrically thick ($H/R \sim 0.5$) and optically thin. In these flows, the dissipated energy heats the gas which is then advected along with the flow. Hence these flows are radiatively inefficient, and emit power-law, non-thermal radiation due to the Compton scattering of hot electrons. The process of advective cooling, also stabilizes ADAFs against the thermal and viscous instabilities. With these properties, ADAFs can consistently account for the observations of a number of low-luminosity hard states of black-hole X-ray binaries (see, e.g., the review by Done, Gierliński, and Kubota [39]) and low-luminosity active galactic nuclei, including Sgr A* [40], [41] which cannot be explained by a luminous, standard thin disc. Long-term X-ray observations show that even in the low-luminosity quiescence state, black hole XRBs exhibit rapid aperiodic variability (see Section 1.2.3) thought to arise from *propagating fluctuations*. We discuss this in Section 1.3.3

1.3.2 The disc-instability model of dwarf-novae outbursts

Under the thermal equilibrium conditions, the rate at which the disc is locally heated due to viscous dissipation (Q^+) balances the cooling rate (Q^-) due to emission at that radius. For standard thin discs, the solutions of a thermal equilibrium state traces an S-shaped curve on the (Σ, T_{eff}) plane (where Σ and T_{eff} are the surface density and effective temperature of the disc at a given radius, respectively). While the upper and lower branches of the S-curve are in a stable equilibrium, the middle branch is unstable since

$$\frac{\mathrm{d}\log Q^+}{\mathrm{d}\log T_c} > \frac{\mathrm{d}\log Q^-}{\mathrm{d}\log T_c}, \quad (1.6)$$
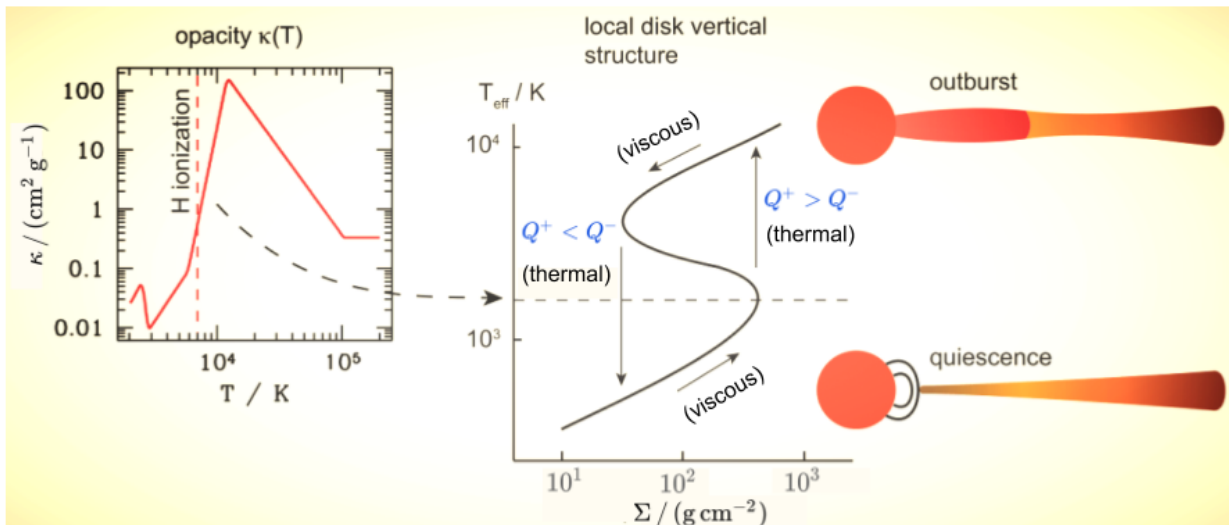
Figure 1.2: Disc instability due to hydrogen ionization. For a given radius, a strongly temperature-dependent opacity at $T \sim 10^4$ K (left panel) results in thermal equilibrium solutions ($Q^+ = Q^-$) that trace an "S"- shaped curve in the plane of surface density vs effective temperature (middle panel). A global outburst in the disc (right panel) is then possible, depending upon the conditions in the neighbouring annuli. Credit: [42]

where T_c is the disc midplane temperature. Therefore, any perturbations in the temperature from the middle branch leads to a "limit-cycle" behaviour where the disc oscillates between the hot and cold states (i.e, the upper and lower branches).

The illustration in Figure 1.2 well summarizes this "limit-cycle" behaviour. During the quiescent state, the disc builds up mass due to steady mass transfer rate from the companion, increasing both Σ and T_c. Once the disc temperatures reach roughly 10^4 K, the opacity rises rapidly due to hydrogen ionization, leading to an unstable equilibrium (equation 1.6). Thus any further small increase in the temperature will cause the heating rate to exceed the cooling rate, triggering the thermal instability. Since viscous stresses are proportional to pressure, an increase in temperature causes an increase in mass accretion rate, thereby triggering viscous instability. The resulting sudden jump in the local density and the steep temperature gradients diffuse and propagate as heating fronts, which are similar to combustion waves. Under appropriate conditions, this local thermal-viscous instability can lead to a global instability, where the local heating fronts propagate inwards (and outwards) on viscous timescales to trigger instability in the adjacent disc annuli. This outsets the rise of the outburst, and the mass accretion rate throughout the disc increases as the heating fronts propagate and the disc reaches a hot state. When the outward propagating front reaches disc regions with hydrogen recombination temperatures, the sudden drop in opacity once again triggers thermal instability. This time a cooling front, similar to the heating front, propagates inwards as the disc returns to the cold, quiescent state.

1D time-dependent numerical models have been developed for evolving the standard thin discs
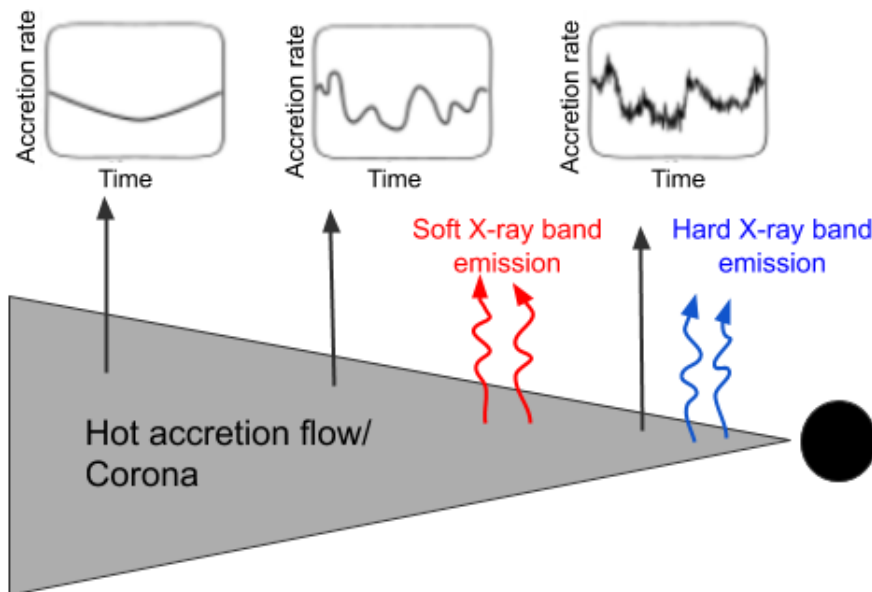
Figure 1.3: Propagating fluctuations in ADAFs.

to study the outburst properties [43]. The models assume different values of the α-viscosity parameter for discs in quiescent (α of the order of 0.01) and outburst ($\alpha \geq 0.1$) states to reproduce the brightness amplitudes in the observed light curves. These effective values of α agree with measured values of MRI-driven α (0.1-0.3 when MRI peaks and 0.01-0.1 when MRI saturates) from global 3D magnetohydrodynamic simulations [44]. Although MRI simulations that can resolve the propagation of heating and cooling fronts would be very illuminating, such simulations are challenging with the current computational resources.

Several works in the past based on the disc–instability model have successfully reproduced the outbursts in most of the CVs, and LMXBs (see Lasota [11] and references therein). However, disc instabilities in SSs remained unexplored until recently [45], primarily for the reason that SSs harbour large accretion discs[3] that are challenging to evolve and second, most of the outbursts in SSs are thought to be triggered by thermonuclear burning (due to their high brightness amplitudes). An important question is whether or not disc instabilities exist in these systems and if so, what role do they play in triggering or modulating the outbursts observed in these systems. In Chapter 2 (Paper I) we explore this very question, by studying the disc instabilities in two classic SSs: RS Oph, a recurrent nova and Z And, a classic symbiotic star.

1.3.3 Propagating fluctuations

As we discussed earlier in Section 1.3.1, turbulence in the accretion flow, plays a key role in transporting angular momentum and driving accretion. Lyubarskii [46] proposed that the turbulence could also generate fluctuations in the mass accretion rate, which propagates inwards by modulating the fluctuations occurring at smaller radii. This is the basic idea of the propagating fluctuations model, based on which many other models emerged. These models assume that either the fluctuations are driven at local viscous timescales or that only those fluctuations whose frequency is less than the local viscous

---

[3]Usually, around $10^{12} - 10^{13}$ cm in radial extent, a few orders of magnitude larger than the discs in CVs.

frequency, propagate inwards. Thus the origin of the low-frequency fluctuations are associated with larger radii, while high-frequency fluctuations are associated with the inner radii. The propagating fluctuations model readily explains the broad-band variability and other important variability features observed in X-ray binaries (see Section 1.2.3). As the fluctuations propagate, the accretion rate, and by that the flux emission from the inner disc regions, carries the imprints of the fluctuations generated from the wide range of radii associated over a broad-range of timescales – giving a continuous band of power over a wide range of frequencies. The multiplicative nature of the coupling of fluctuations gives rise to a lognormal distribution of flux and the linear rms-flux relation. Moreover, the fluctuations generated at outer radii first appear in the softer energy bands, and later propagate inwards to appear in the hard-energy bands. This leads to positive time lags between the hard and soft-energy bands and if the flux emissivity is more concentrated towards the hard-energy bands, it automatically introduces the observed frequency-dependency in the lags. The basic idea of the model is pictured in Figure 1.3.

The model assumes that the fluctuations in the α-viscosity parameter will drive fluctuations in the mass accretion rate, and the fluctuations are required to be preserved as they propagate in – none of which is guaranteed in the real astrophysical flows with MRI-driven turbulence. Thus to better understand the physical process driving these fluctuations, it is first important to test this model using numerical simulations, as they are capable of evolving accretion flows close to reality and then check if the observational features could be reproduced. This motivates our Paper IV, where we use general relativistic magnetohydrodynamic (GRMHD) simulations of ADAFs to test the model, since the broad-band variability is seen more prominently in the low-luminosity states, which have ADAF structures.

1.4 Levitating atmospheres

The Eddington limit derived in the Section 1.3 (see equation 1.4), ignores the relativistic effects which play a vital role for compact object systems. In general relativity, photons are subjected to gravitational redshift phenomena, in which case the expression for Eddington luminosity is modified to $L_{\text{Edd}}(1+z)$ [47], where $1+z = [1 - 2GM/(rc^2)]^{-1/2}$ is the redshift factor. Note that the relativistic Eddington limit has radial dependence, implying that for a star with a given luminosity, there exists a finite radius, (say r_0) at which the gravitational and radiation forces are in balance. This radius termed as the Eddington Capture sphere (ECS), can be expressed in terms of the Eddington parameter, $\lambda \equiv L_\infty/L_{\text{Edd}}$, as $r_0 = 2GM/[c^2(1-\lambda^2)]$ and L_∞ is the stellar luminosity measured at infinity. For any $r < r_0$, radiation forces dominate while gravity dominates at all $r > r_0$. Thus, for a star radiating at super-Eddington luminosities, a spherical shell of matter in hydrostatic balance, called "levitating" atmosphere, can form at r_0 above the stellar surface. These atmospheres could deflect the gravitationally lensed light rays by the compact object, thus significantly affecting the object's appearance in the observations [48].

An important question is how stable are these atmospheres? Any perturbed object under the action of restoring forces is subject to oscillations. The frequencies of various oscillation modes in thin discs have been considered as a successful explanation for the high frequency, quasi-periodic oscillations (QPOs) observed in the X-ray binaries (see, e.g., McClintock and Remillard [12], Wagoner [49], and Kato [50]). Similarly, for the levitating shells, Abarca and Kluźniak [51] investigated the oscillations in the radial fundamental mode, whose frequency is not only comparable to the burst oscillation frequencies (observed during the Type-I X-ray bursts), but also increases as the luminosity
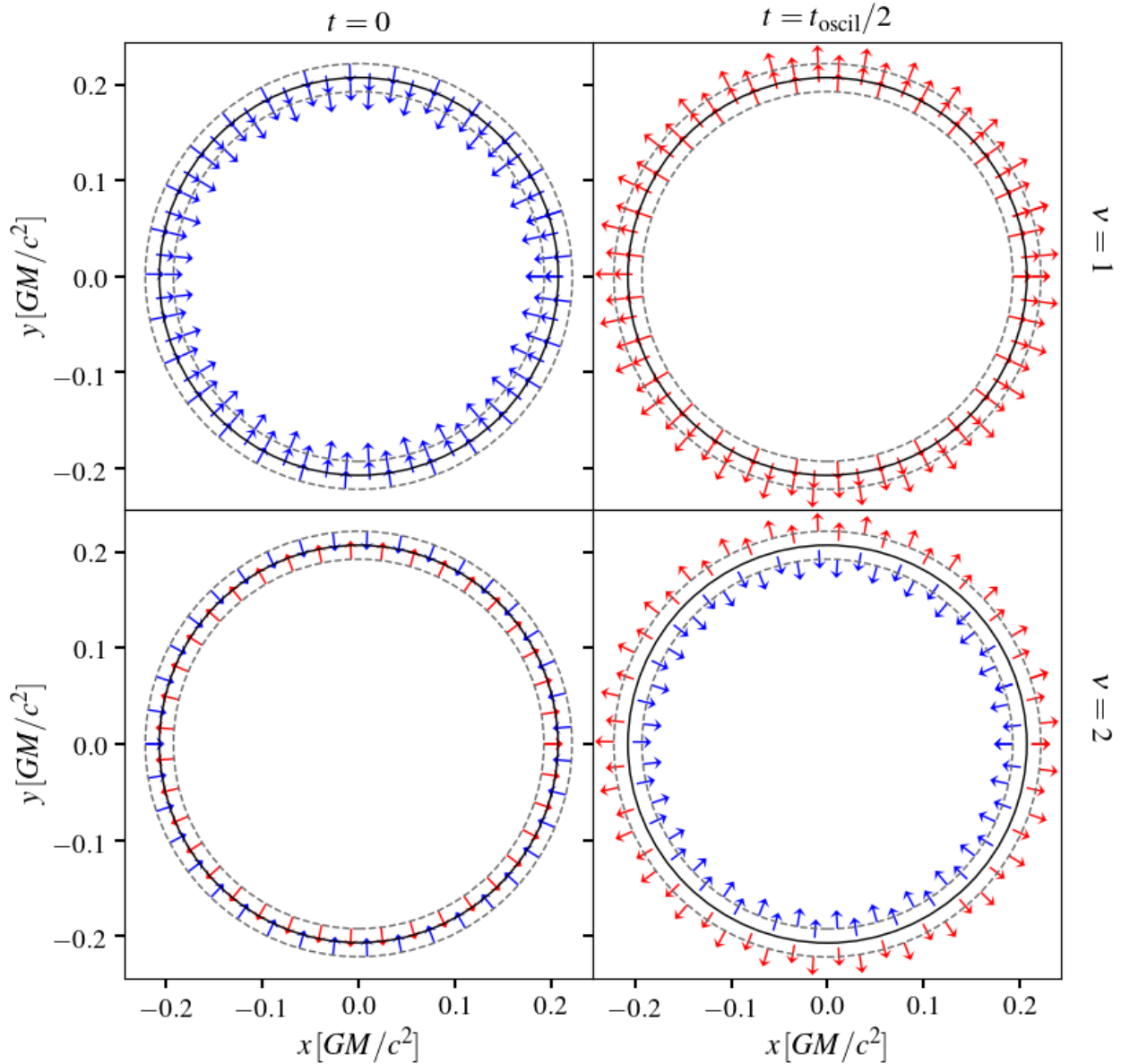
Figure 1.4: A two-dimensional projection of oscillations of an optically thin, geometrically thin levitating atmosphere located around a star with $\lambda = 0.85$. The solid circle represents the ECS, while the dashed circles on either side mark the edges of the atmosphere. The radial velocity vectors in the atmosphere for the fundamental mode ($\nu = 1$, top panel) and breathing mode ($\nu = 2$, bottom panel) at an initial time $t = 0$ (left panel) and half an oscillation period later (right panel) are shown. The blue and red colour of the velocity vectors distinguishes the motion towards and away from the star, respectively. Horizontal and vertical axes are in Cartesian coordinates, arbitrarily scaled for enlarged visibility of the atmosphere.

decreases. However this particular mode was found to be overdamped when the radiation drag on the particles is considered. Since the neutron star radiates at near-Eddington luminosity during the Type-I X-ray burst, these levitating atmospheres could indeed be relevant to burst oscillations. Therefore, in Chapters 3 and 4, we explore the stability of other possible modes of oscillation, with and without including the radiation drag, to see if they could provide a possible explanation for the burst oscillations, particularly for the ones observed in the outburst tail.

Figure 1.4 gives an idea of the oscillations in an optically and geometrically thin levitating atmosphere for the two lowest oscillation modes - the radial and breathing modes. The radial mode is the fundamental mode of oscillations, in which the entire atmosphere oscillates radially, with no nodes. The next higher mode is the breathing mode, in which the atmosphere oscillates towards and away from the ECS, with a node located at the ECS.

1.5 Motivation and thesis overview

The main motivation of the thesis lies in understanding the nature of different variability features observed in compact object systems, in the light of accretion discs and shells present around these objects. In this thesis we took analytic, semi-analytical and GRMHD simulation approaches, based on what best suits the problem.

Here we provide a brief summary of each chapter, in connection to the open ended questions and concepts reviewed in the previous sections.

Paper I: Disc instabilities and nova eruptions in symbiotic systems: RS Ophiuchi and Z Andromedae [Bollimpalli et. al., MNRAS 481, 5422-5435, 2018]

In this paper, we studied the disc instabilities in SSs, with particular emphasis on two systems, RS Oph and Z And. We used the 1D time-dependent numerical code developed by Hameury, Menou, Dubus, *et al.* [43][4] to solve the standard disc equations in the radial dimension of a geometrically thin, optically thick disc in order to follow its thermal and viscous evolution. Our findings suggest that the RS Oph outbursts are recurrent 'combination nova events' where a series of dwarf nova outbursts can trigger the recurrent nova eruptions. This might explain the puzzling observations of the RS Oph light-curve such as the increase in pre-outburst luminosity and varying X-ray flux at different epochs during the quiescence. In general, combination nova events scenario could also potentially explain the problem we discussed in Section 1.2.1, i.e., short recurring timescales compared to their estimated accretion rates from observations. For Z And, we explored the possibility of disc-instability outbursts responsible for its complex light curve and only found that they are probably of no importance. Our results also rule out the hypothesis of the 2000-2002 outburst of Z And being a 'combination nova' event (as proposed in Sokoloski, Kenyon, Espey, *et al.* [18]). We instead suggest that the enhancement of mass transfer from the companion star could be the key, which may or may not trigger disc-instability outbursts.

---

[4]With some additional modifications like boundary conditions, as discussed in the paper, that enable us to evolve the large accretion discs.

Paper-II: Radial modes of levitating atmospheres around Eddington-luminosity neutron stars [Bollimpalli & Kluźniak, MNRAS 472, 3298-3303, 2017]

In this paper, we study the radial oscillations of levitating atmospheres under the optically thin limit in Newtonian formalism. We assumed that the atmosphere is geometrically thin and radiation drag is neglected. Thereby, the derived normal mode oscillations are undamped and depend only on the atmosphere's polytropic index. The eigenfrequencies fall in the observed range of 300–600 Hz for burst oscillation frequencies and also decrease with increasing luminosity, similar to the frequency drift observed in the burst oscillations as the burst progresses.

Paper III: Atmospheric oscillations provide simultaneous measurement of neutron star mass and radius [Bollimpalli et. al., MNRAS 487, 5129-42, 2019]

In this paper, we extended our work in Paper II to studying atmospheric oscillations in full general relativity, including the radiation drag and found that the oscillation frequency has a characteristic maximum. The key result of this work is that the frequency of these oscillations depends only on the stellar parameters and luminosity which allows the direct measurement of the mass and radius, given the observations of maximum frequency and flux. In fact, with this method, it could be possible also to directly determine the distance to the neutron star with an accuracy of about one percent. Such high accuracy measurements of mass and radius of neutron star would have profound implications for constraining the equation of state of dense matter.

Paper IV: Looking for the underlying cause of black hole X-ray variability in GRMHD simulations [Bollimpalli et. al., MNRAS 496, 3808-28, 2020]

As discussed in section 1.3.3, the aperiodic variability and the other characteristic features observed in black-hole X-ray binaries are well explained by the propagating fluctuations model. However this is only a phenomenological model and it is not obvious that the MRI-driven turbulence in the real accretion flows can drive these fluctuations. In order to check this, we analyse the data from five different GRMHD simulations of ADAFs performed using different codes to look for hints of propagating fluctuations in the simulation data. We found that despite the differences in the initial setups and outcomes of these simulations, the accretion rate shows evidence for inward propagating fluctuations indicating their robust nature. We found a) a strong radial coherence below the viscous frequency, b) variability at smaller radii lagging variability at larger radii, c) linear rms-flux relation derived from the power spectra. and d) a log-normal distribution – all which are consistent with the observations. When combining the mass fluxes from the simulations with an assumed emissivity profile, we also find broad agreement with observed power spectra and time lags, including a recovery of the frequency dependency of the time lags.

Bibliography

[1] D. H. Clark and F. R. Stephenson, "The Historical Supernovae," *NATO Advanced Science Institutes (ASI) Series C*, M. J. Rees and R. J. Stoneham, Eds., ser. NATO Advanced Science Institutes (ASI) Series C, vol. 90, 1982, pp. 355–370.

[2] P. Murdin and L. Murdin, *Supernovae.* 1985.

[3] J. B. Hearnshaw, "Origins of the Stellar Magnitude Scale," S&T, vol. 84, p. 494, 1992.

[4] S. L. Shapiro and S. A. Teukolsky, *Black Holes, White Dwarfs and Neutron Stars: The Physics of Compact Objects.* 1986.

[5] U. Munari, "The symbiotic stars," in *The Impact of Binary Stars on Stellar Evolution*, ser. Cambridge Astrophysics. Cambridge University Press, 2019, 77–91. DOI: 10.1017/9781108553070.008.

[6] U. Mürset, H. Nussbaumer, H. M. Schmid, and M. Vogel, "Temperature and luminosity of hot components in symbiotic stars.," A&A, vol. 248, p. 458, 1991.

[7] P. A. Charles and M. J. Coe, "Optical, ultraviolet and infrared observations of x-ray binaries," in *Compact Stellar X-ray Sources*, W. Lewin and M. van der Klis, Eds., ser. Cambridge Astrophysics. Cambridge University Press, 2006, 215–266. DOI: 10.1017/CBO9780511536281.006.

[8] J. Casares, P. G. Jonker, and G. Israelian, "X-Ray Binaries," in *Handbook of Supernovae*, A. W. Alsabti and P. Murdin, Eds. 2017, p. 1499. DOI: 10.1007/978-3-319-21846-5_111.

[9] P. Kaaret, H. Feng, and T. P. Roberts, "Ultraluminous x-ray sources," ARA&A, vol. 55, no. 1, 303–341, 2017, ISSN: 1545-4282. DOI: 10.1146/annurev-astro-091916-055259.

[10] K. Atapin, "Ultraluminous X-ray Sources," *PoS*, vol. APCS2018, p. 038, 2019. DOI: 10.22323/1.342.0038.

[11] J.-P. Lasota, "The disc instability model of dwarf novae and low-mass x-ray binary transients," *New Astronomy Reviews*, vol. 45, no. 7, 449–508, 2001, ISSN: 1387-6473. DOI: 10.1016/s1387-6473(01)00112-9.

[12] J. E. McClintock and R. A. Remillard, "Black hole binaries," in *Compact stellar X-ray sources.* 2006, vol. 39, pp. 157–213.

[13] K. Mukai, "Recurrent Novae - A Review," *Acta Polytechnica CTU Proceedings*, vol. 2, pp. 246–251, 2015. arXiv: 1407.4526 [astro-ph.HE].

[14] S. J. Kenyon and R. F. Webbink, "The nature of symbiotic stars.," ApJ, vol. 279, pp. 252–283, 1984. DOI: 10.1086/161888.

[15] J. Iben I., "Hot accreting white dwarfs in the quasi-static approximation," ApJ, vol. 259, pp. 244–266, 1982. DOI: 10.1086/160164.

[16] S. J. Kenyon and J. W. Truran, "The outbursts of symbiotic novae.," ApJ, vol. 273, pp. 280–288, 1983. DOI: 10.1086/161367.

[17] W. J. Duschl, "Accretion disk models for symbiotic stars. I - Stationary accretion disks. II - Time-dependent accretion disks," A&A, vol. 163, no. 1-2, pp. 56–66, 1986.

[18] J. L. Sokoloski, S. J. Kenyon, B. R. Espey, C. D. Keyes, S. R. McCandliss, A. K. H. Kong, J. P. Aufdenberg, A. V. Filippenko, W. Li, C. Brocksopp, and et al., "A "combination nova" outburst in z andromedae: Nuclear shell burning triggered by a disk instability," ApJ, vol. 636, no. 2, 1002–1019, 2006, ISSN: 1538-4357. DOI: 10.1086/498206.

[19] W. H. G. Lewin, J. van Paradijs, and R. E. Taam, "X-Ray Bursts," Space Sci. Rev., vol. 62, no. 3-4, pp. 223–389, 1993. DOI: 10.1007/BF00196124.

[20] D. K. Galloway, M. P. Muno, J. M. Hartman, D. Psaltis, and D. Chakrabarty, "Thermonuclear (type i) x-ray bursts observed by therossi x-ray timing explorer," *The Astrophysical Journal Supplement Series*, vol. 179, no. 2, 360–422, 2008, ISSN: 1538-4365. DOI: 10.1086/592044.

[21] J. A. Hoffman, H. L. Marshall, and W. H. G. Lewin, "Dual character of the rapid burster and a classification of X-ray bursts," Nature, vol. 271, no. 5646, pp. 630–633, 1978. DOI: 10.1038/271630a0.

[22] T. Strohmayer and L. Bildsten, "New views of thermonuclear bursts," in *Compact stellar X-ray sources*. 2006, vol. 39, pp. 113–156.

[23] A. L. Watts, "Thermonuclear burst oscillations," ARA&A, vol. 50, no. 1, 609–640, 2012, ISSN: 1545-4282. DOI: 10.1146/annurev-astro-040312-132617.

[24] M. van der Klis, "Rapid aperiodic variability in X-ray binaries.," *X-ray Binaries*, 1995, pp. 252–307.

[25] R. Wijnands and M. van der Klis, "The broadband power spectra of x-ray binaries," ApJ, vol. 514, no. 2, 939–944, 1999, ISSN: 1538-4357. DOI: 10.1086/306993.

[26] S. Scaringi, E. Körding, P. J. Groot, P. Uttley, T. Marsh, C. Knigge, T. Maccarone, and V. S. Dhillon, "Discovery of fourier-dependent time lags in cataclysmic variables," MNRAS, vol. 431, no. 3, 2535–2541, 2013, ISSN: 0035-8711. DOI: 10.1093/mnras/stt347.

[27] M. Van de Sande, S. Scaringi, and C. Knigge, "The rms–flux relation in accreting white dwarfs: Another nova-like variable and the first dwarf nova," MNRAS, vol. 448, no. 3, 2430–2437, 2015, ISSN: 0035-8711. DOI: 10.1093/mnras/stv157.

[28] S. Scaringi, T. J. Maccarone, E. Körding, C. Knigge, S. Vaughan, T. R. Marsh, E. Aranzana, V. S. Dhillon, and S. C. C. Barros, "Accretion-induced variability links young stellar objects, white dwarfs, and black holes," *Science Advances*, vol. 1, no. 9, e1500686, 2015, ISSN: 2375-2548. DOI: 10.1126/sciadv.1500686.

[29] N. I. Shakura and R. A. Sunyaev, "Reprint of 1973A&A....24..337S. Black holes in binary systems. Observational appearance.," A&A, vol. 500, pp. 33–51, 1973.

[30] J. E. Pringle, "Accretion discs in astrophysics," ARA&A, vol. 19, pp. 137–162, 1981. DOI: 10.1146/annurev.aa.19.090181.001033.

[31] M. A. Abramowicz and P. C. Fragile, "Foundations of black hole accretion disk theory," *Living Reviews in Relativity*, vol. 16, no. 1, 2013, ISSN: 1433-8351. DOI: 10.12942/lrr-2013-1.

[32] S. A. Balbus and J. F. Hawley, "A Powerful Local Shear Instability in Weakly Magnetized Disks. I. Linear Analysis," ApJ, vol. 376, p. 214, 1991. DOI: 10.1086/170270.

[33] S. Chandrasekhar, "The Stability of Non-Dissipative Couette Flow in Hydromagnetics," *Proceedings of the National Academy of Science*, vol. 46, no. 2, pp. 253–257, 1960. DOI: 10.1073/pnas.46.2.253.

[34] N. I. Shakura and R. A. Sunyaev, "A theory of the instability of disk accretion on to black holes and the variability of binary X-ray sources, galactic nuclei and quasars.," MNRAS, vol. 175, pp. 613–632, 1976. DOI: 10.1093/mnras/175.3.613.

[35] B. Mishra, P. C. Fragile, L. C. Johnson, and W. Kluźniak, "Three-dimensional, global, radiative grmhd simulations of a thermally unstable disc," MNRAS, vol. 463, no. 4, 3437–3448, 2016, ISSN: 1365-2966. DOI: 10.1093/mnras/stw2245.

[36] B. Mishra, M. C. Begelman, P. J. Armitage, and J. B. Simon, "Strongly magnetized accretion discs: Structure and accretion from global magnetohydrodynamic simulations," MNRAS, vol. 492, no. 2, 1855–1868, 2019, ISSN: 1365-2966. DOI: 10.1093/mnras/stz3572.

[37] D. Lančová, D. Abarca, W. Kluźniak, M. Wielgus, A. Sądowski, R. Narayan, J. Schee, G. Török, and M. Abramowicz, "Puffy accretion disks: Sub-eddington, optically thick, and stable," ApJ, vol. 884, no. 2, p. L37, 2019, ISSN: 2041-8213. DOI: 10.3847/2041-8213/ab48f5.

[38] F. Yuan and R. Narayan, "Hot accretion flows around black holes," ARA&A, vol. 52, no. 1, 529–588, 2014, ISSN: 1545-4282. DOI: 10.1146/annurev-astro-082812-141003.

[39] C. Done, M. Gierliński, and A. Kubota, "Modelling the behaviour of accretion flows in x-ray binaries," *The Astronomy and Astrophysics Review*, vol. 15, no. 1, 1–66, 2007, ISSN: 1432-0754. DOI: 10.1007/s00159-007-0006-1.

[40] M. J. Rees, M. C. Begelman, R. D. Blandford, and E. S. Phinney, "Ion-supported tori and the origin of radio jets," Nature, vol. 295, no. 5844, pp. 17–21, 1982. DOI: 10.1038/295017a0.

[41] R. Narayan, R. Mahadevan, J. E. Grindlay, R. G. Popham, and C. Gammie, "Advection-dominated accretion model of Sagittarius A*: Evidence for a black hole at the galactic center," ApJ, vol. 492, no. 2, 554–568, 1998, ISSN: 1538-4357. DOI: 10.1086/305070.

[42] P. J. Armitage, "Dynamics of protoplanetary disks," ARA&A, vol. 49, no. 1, 195–236, 2011, ISSN: 1545-4282. DOI: 10.1146/annurev-astro-081710-102521.

[43] J.-M. Hameury, K. Menou, G. Dubus, J.-P. Lasota, and J.-M. Huré, "Accretion disc outbursts: A new version of an old model," MNRAS, vol. 298, no. 4, 1048–1060, 1998, ISSN: 1365-2966. DOI: 10.1046/j.1365-8711.1998.01773.x.

[44] W. Ju, J. M. Stone, and Z. Zhu, "Global mhd simulations of accretion disks in cataclysmic variables (cvs). ii. the relative importance of mri and spiral shocks," ApJ, vol. 841, no. 1, p. 29, 2017, ISSN: 1538-4357. DOI: 10.3847/1538-4357/aa705d.

[45] R. D. Alexander, G. A. Wynn, A. R. King, and J. E. Pringle, "Disc instability in RS Ophiuchi: a path to Type Ia supernovae," MNRAS, vol. 418, no. 4, pp. 2576–2583, 2011. DOI: 10.1111/j.1365-2966.2011.19647.x.

[46] Y. E. Lyubarskii, "Flicker noise in accretion discs," MNRAS, vol. 292, no. 3, pp. 679–685, 1997. DOI: 10.1093/mnras/292.3.679.

[47] M. A. Abramowicz, G. F. R. Ellis, and A. Lanza, "Relativistic Effects in Superluminal Jets and Neutron Star Winds," ApJ, vol. 361, p. 470, 1990. DOI: 10.1086/169211.

[48] A. Rogers, "Gravitational lensing of rays through the levitating atmospheres of compact objects," *Universe*, vol. 3, no. 1, p. 3, 2017, ISSN: 2218-1997. DOI: 10.3390/universe3010003.

[49] R. V. Wagoner, "Relativistic diskoseismology," *Physics Reports*, vol. 311, no. 3-5, 259–269, 1999, ISSN: 0370-1573. DOI: 10.1016/s0370-1573(98)00104-5.

[50] S. Kato, *Oscillations of Disks*. 2016, vol. 437. DOI: 10.1007/978-4-431-56208-5.

[51] D. Abarca and W. Kluźniak, "Radial oscillations of a radiation-supported levitating shell in eddington luminosity neutron stars," MNRAS, vol. 461, no. 3, 3233–3238, 2016, ISSN: 1365-2966. DOI: 10.1093/mnras/stw1432.

Part II

Variability in White dwarfs: Disc-instability outbursts

Chapter 2

Paper I: Disc instabilities and nova eruptions in symbiotic systems: RS Ophiuchi and Z Andromedae

Disc instabilities and nova eruptions in symbiotic systems: RS Ophiuchi and Z Andromedae

D. A. Bollimpalli,[1,4]★ J.-M. Hameury[2,4]★ and J.-P. Lasota [1,3,4]★

[1]*Nicolaus Copernicus Astronomical Center, Polish Academy of Sciences, ul. Bartycka 18, PL 00-716 Warsaw, Poland*
[2]*Université de Strasbourg, CNRS, Observatoire Astronomique de Strasbourg, UMR 7550, 67000 Strasbourg, France*
[3]*Institut d'Astrophysique de Paris, CNRS et Sorbonne Université, UMR 7095, 98bis Bd Arago, 75014 Paris, France*
[4]*Kavli Institute for Theoretical Physics, Kohn Hall, University of California, Santa Barbara, CA 93106, USA*

ABSTRACT

Using the disc instability model for dwarf novae and soft X-ray transients, we investigate the stability of accretion discs in long-period binary systems. We simulate outbursts resulting from this thermal-viscous instability for two symbiotic systems, RS Ophiuchi and Z Andromedae. The outburst properties deduced from our simulations suggest that, although the recurrent nova events observed in RS Oph are caused by thermonuclear runaway at the white dwarf surface, these runaways are triggered by accretion disc instabilities. In quiescence, the disc builds up its mass, and it is only during the disc-instability outburst that mass is accreted on to the white dwarf at rates comparable to or larger than the mass-transfer rate. For a mass-transfer rate in the range 10^{-8} to $10^{-7}\,\mathrm{M_\odot\,yr^{-1}}$, the accretion rate and the mass accreted are sufficient to lead to a thermonuclear runaway during one of a series of a few dwarf nova outbursts, which are barely visible in the optical but easily detectable in the X-rays. In the case of Z And, persistent irradiation of the disc by the very hot white dwarf surface strongly modifies the dwarf nova outburst properties, making them significant only for very high mass-transfer rates, of the order of $10^{-6}\,\mathrm{M_\odot\,yr^{-1}}$, much higher than the expected secular mean in this system. It is thus likely that the so-called 'combination nova' outburst observed in the years 2000 to 2002 was triggered not by a dwarf-nova instability but by a mass-transfer enhancement from the giant companion, leading to an increase in nuclear burning at the accreting white dwarf surface.

Key words: accretion, accretion discs – binaries: symbiotic – stars: dwarf novae – stars: individual: RS Oph – stars: individual: Z And.

1 INTRODUCTION

Symbiotic stars are interacting binary systems in which a hot primary star accretes the matter lost by an evolved-giant, secondary star. In most known cases the primary is a white dwarf, but several systems with a neutron star primary have also been observed. These binary systems show several types of outburst. A small subset comprises objects observed as 'slow novae', whose outbursts last for decades; another subset is formed by recurrent novae, whose outbursts repeat on time-scales from several to several tens of years. Both types of nova outburst are known to result from thermonuclear runaway in the hydrogen-rich layer accumulated by accretion on the white dwarf surface. Table 1 lists the properties of Galactic recurrent novae, which have long orbital periods. The third type is that of classical symbiotic outbursts (hereinafter CSOs), and their

origin is still the subject of debate (see e.g. Sokoloski et al. 2006b, hereinafter S2006, and references therein).

In most cases, the companion giant star underfills its Roche lobe, and accretion on to the primary star occurs through stellar wind capture, which does not guarantee the presence of an extended disc. Despite that, dwarf-nova-type outbursts involving discs have been invoked as a possible source of, or a contributor to, CSOs (Duschl 1986a,b; Mikolajewska et al. 2002; Sokoloski et al. 2006b), and even as an explanation of the outbursts of one of the recurrent novae, RS Oph (King & Pringle 2009; Alexander et al. 2011).

The orbital periods of symbiotic stars range from years to decades, corresponding to binary separations ranging from 10^{13} to 10^{15} cm. Thus the accretion discs (if present) in such wide binary systems are subject to the thermal-viscous instability even for huge mass-transfer rates, since the critical accretion rate, below which the disc is unstable, increases with a 2.4 to 2.6 power of the disc radius (Lasota, Dubus & Kruk 2008).

The typical size of the accretion disc in a dwarf nova ranges from about 10^{10} to 10^{11} cm. Outbursts in such systems have been very well

★ E-mail: deepika@camk.edu.pl (DAB);
jean-marie.hameury@astro.unistra.fr (JMH); lasota@iap.fr (JPL)

Table 1. Galactic recurrent novae with long binary orbital periods.

Object	Outburst year	P_{rec} [yr]	P_{orb} [d]	M_{WD} [M$_\odot$]	m_{min} [mag]	m_{max} [mag]
T CrB	1866, 1946	<80	228	$\gtrsim$1.35	2.5	9.8
RS Oph	1898, 1907, 1933, 1945, 1958, 1967, 1985, 2006	<22	453.6	$\sim$1.35	4.8	11
V745 Sco	1937, 1989 ,2014	<52	510	$\gtrsim$1.35	9.4	18.6
V3890 Sgr	1962, 1990	<27	519.7	$\gtrsim$1.35	8.1	15.5

The table lists the basic parameters of a few Galactic recurrent novae. The years in which outbursts were observed and the recurrence period of the outburst are given in the second and third columns. The next two columns shows the binary orbital period and mass of the white dwarf, and the final two columns give the brightness in the *V* band measured during the outburst peak and quiescence. References: Schaefer (2010); Anupama (2013).

modelled by the disc instability model (DIM; see Lasota 2001, for a review of the model). There have not been many attempts to apply the DIM to the description of the large discs of symbiotic stars (SBs), with the notable exceptions of the work of Duschl (1986a,b) and Alexander et al. (2011). In two papers, Duschl (1986a,b) studied the stationary and time-dependent behaviour of accretion discs around a main-sequence star and suggested that the light-curves of SBs can be explained by disc instabilities. Since the accreting primary was a main-sequence star and the transition fronts were approximated as quasi-stationary, these models are not directly applicable to the study of outbursts in SBs as known at present (Sokoloski et al. 2017). The simplified code used by Alexander et al. (2011) in their study of RS Oph outbursts requires serious improvements in order to be able to describe the physics of accretion disc outbursts (Graham Wynn, private communication; see also Section 3.1.1). The DIM code developed by Hameury et al. (1998) and Dubus et al. (1999) has been used to describe outbursts of irradiated low-mass X-ray binary (LMXB) discs extending up to radii of a few times 10^{11} cm (Dubus 1998; Dubus, Hameury & Lasota 2001), but larger configurations have not yet been explored.

In this article we use our DIM code to test two hypotheses involving disc instabilities in the context of SBs. First, inspired by King & Pringle (2009) and Alexander et al. (2011), we examine the role of dwarf-nova-type instabilities in the 2006 outburst of the recurrent nova RS Oph. In particular, we test the hypothesis (Alexander et al. 2011; John Cannizzo, private communication) that the thermonuclear runaway in this and other similar systems could be triggered by a single dwarf-nova instability. Secondly, we address the 'combination nova' scenario (S2006), according to which a CSO observed in the prototypical SB Z And is caused by an increase of thermonuclear shell-burning triggered by accretion disc instability. We also study the possibility of 'pure' dwarf nova outbursts in shell-burning SBs. A direct comparison of the light-curves generated by the DIM code with the observational data is not appropriate because this would require the DIM code to be coupled with a code describing the thermonuclear runaway at the white dwarf surface. Instead, for each model we consider, we compare the model predictions of the general outburst characteristics (outburst duration and amplitude, recurrence time) with the observed values.

2 THE MODEL

We use the version of the DIM described by Hameury et al. (1998), with added heating due to stream impact and the dissipation by the tidal torques as described by Buat-Ménard, Hameury & Lasota (2001). The code we have developed solves the standard disc equations in the radial dimension (mass, angular momentum and energy conservation, see e.g. Lasota 2001) of a geometrically thin, opti-

cally thick disc in order to follow its thermal and viscous evolution. Since the disc is assumed to be geometrically thin, the radial and vertical dimensions decouple, and the viscous-heating as well as the radiative-cooling terms can be calculated as a function of local quantities (surface density, central disc temperature, radius) only. The code is implicit and uses an adaptive grid so that the heating and cooling fronts are well resolved; the inner and outer edges of the disc are allowed to vary in time (see below). Time derivatives are calculated using a Lagrangian scheme. The non-linear equations are solved using a generalized Newton–Raphson method.

The heating and cooling terms are calculated by solving the vertical structure of the accretion disc, assuming hydrostatic and thermal equilibrium. The equations are very similar to those used for the stellar structure. The main difference is the heating term, which is the result of viscous rather than nuclear processes. This enables us to determine the temperature profile, and in particular the central and effective temperature as a function of the local surface density Σ and radius, for a given viscosity parameter α. The disc is not necessarily in thermal equilibrium though. As noted by Hameury et al. (1998), this introduces an additional term into the heat transport equation, which is supposed to have the same behaviour as the viscous heating term; that is, it is proportional to pressure. The disc vertical structure can then be determined for any position and Σ when the disc is not in thermal equilibrium, but α is no longer given; the central temperature then becomes a free parameter. In order to speed up the resolution of the radial time-dependent equations, effective temperatures are pre-calculated on a grid in radius, Σ and central temperature, and trilinear interpolation is performed on this grid.

Throughout this paper, unless otherwise noted (model RSB-A, see Section 3), we take the Shakura–Sunyaev viscosity parameters to be $\alpha_c = 0.02$ for a cold neutral disc and $\alpha_h = 0.1$ when the disc is hot and ionized.

2.1 Disc irradiation

For irradiated discs we use the version of the code (IDIM) described by Dubus et al. (1999, 2001); Lasota et al. (2008) in the context of LMXBs and Hameury, Lasota & Dubus (1999) in the slightly different context of cataclysmic variables. Irradiation does not affect the time-dependent radial equations, but only modifies the vertical structure of the disc by changing the relationship $F_z = \sigma T_{eff}^4$ into $F_z + F_{irr} = \sigma T_{eff}^4$.

The flux F_{irr} irradiating the outer disc regions is written as

$$F_{irr} \equiv \sigma_{SB} T_{irr}^4 = \mathcal{C} \frac{L}{4\pi R^2}, \tag{1}$$

where R is the radial coordinate, σ_{SB} is the Stefan–Boltzmann constant, and $\mathcal{C} < 1$ is a constant encapsulating the irradiation geometry, albedo etc. This very simple description of disc irradiation gives satisfactory results when describing outer-disc irradiation in X-ray binaries, in particular in transient systems (Dubus et al. 2001; Tetarenko et al. 2018a). In this case, $L = L_{acc} = \eta \dot{M} c^2$, where η is the accretion radiation efficiency. The ratio of irradiation to accretion ('viscous') flux is, in the steady-state case,

$$\frac{F_{irr}}{F_{acc}} = \frac{4}{3} \mathcal{C} \eta \frac{R}{R_S F}, \tag{2}$$

where $R_S = 2GM_1/c^2$ is the Schwarzschild radius, M_1 being the primary mass, and

$$F_{acc} \equiv \sigma_{SB} T_{eff}^4 = \frac{3GM_1\dot{M}}{8\pi R^3}. \tag{3}$$

For $\mathcal{C} \approx 10^{-3}$ and $\eta \approx 0.1$, used in models of X-ray transients (Dubus et al. 2001), $F_{irr}/F_{acc} \approx 10^{-4} R/R_S$ and $T_{irr} > T_{eff}$ for $R > 10^4 R_S$. However, for white dwarfs $\eta \approx 10^{-5}$ to 10^{-3}, and even for very large discs, self-irradiation of the outer disc is never in practice important because it would require disc radii $R > 10^6$ to $10^8 R_S \approx 4 \times 10^{11}$ to 10^{13} cm. It is only for massive white dwarfs and $\mathcal{C} \approx 10^{-2}$ that self-irradiation of the outer region could play a role in the disc structure and evolution (see the discussion below in the case of RS Oph).

In some systems such as symbiotic stars and supersoft X-ray sources, however, the steady thermonuclear burning of matter accumulated at the white dwarf surface can be important and even dominate accretion disc irradiation. In this case,

$$\begin{aligned}\frac{F_{irr,*}}{F_{acc}} &\approx \frac{2}{3} \frac{\mathcal{C}L_*}{GM_1\dot{M}/R_*} \frac{R}{R_*} \\ &\approx 0.5 \left(\frac{M_\odot}{M_1}\right) \left(\frac{R}{10^8 cm}\right) \left(\frac{\mathcal{C}L_*}{10^{37} erg\, s^{-1}}\right) \left(\frac{10^{19} g\, s^{-1}}{\dot{M}}\right),\end{aligned} \tag{4}$$

where R_* is the white dwarf radius. In the symbiotic star Z And, for example, the steady luminosity of thermonuclear burning is about 10^3 $L_\odot$. So even for very high accretion rates, the outer-disc surface temperature is dominated by irradiation from the central source. Since constant irradiation is independent of the accretion rate, it impacts the whole disc outburst cycle because, in contrast to the accretion–self-irradiation case, irradiation is also present during quiescence. Notice that in equation (4), in contrast to equation (2), the ratio $F_{irr,*}/F_{acc}$ depends on the accretion rate and *decreases* with increasing $\dot{M}$.

It should be noted, however, that it is not clear under what conditions equation (1) applies to discs around white dwarfs, and in particular what value of $\mathcal{C}$ should be used. In X-ray binaries, for which there is direct evidence of outer-disc irradiation, a 'reasonable' value for $\mathcal{C}$ is about a few times 10^{-3} (Dubus et al. 1999; Coriat, Fender & Dubus 2012; see, however, Tetarenko et al. 2018b). Note that the $\mathcal{C}$ used here differs from the $\mathcal{C}$ as defined by Dubus et al. (1999) in that it does not include the efficiency parameter η.

Equation (1) assumes that the disc is irradiated by a point source. This assumption is no longer true close to the white dwarf, and irradiation has to be described (see e.g. Hameury et al. 1999) by

$$F_{irr,S} \equiv \sigma_{SB} T_{irr,*}^4 = (1 - \beta) \left[\sin^{-1} \rho - \rho\sqrt{1 - \rho^2}\right] \frac{T_*^4}{\pi}, \tag{5}$$

where the subscript $*$ refers to quantities measured at the white dwarf surface and $\rho = R/R_*$.

At large distances, $F_{irr,S}$ as given by equation (5) varies as R^{-3} and is much smaller than the value that would be obtained using

equation (1); conversely, close to the white dwarf, equation (1) underestimates the irradiation flux.

In what follows, when the ratio of the disc scale-height to the stellar radius $H/R_* > 1$, we use equation (1) to describe irradiation, whereas in the opposite case, $H/R_* < 1$, we use equation (5).

2.2 Boundary conditions

Since radiation pressure can be dominant during outbursts, and gravity could potentially vary within the extended disc photosphere, the usual photospheric boundary condition $\kappa P_g = 2/3 g_z$ is replaced (Hameury, Viallet & Lasota 2009) with

$$\kappa \left(P_g + \frac{1}{2} P_{rad}\right) = \frac{2}{3} g_z \left(1 + \frac{1}{\kappa\rho z}\right), \tag{6}$$

where κ is the Rosseland mean opacity, g_z is the vertical component of gravity, ρ is the density, and P_g and P_{rad} are the gas and radiation pressure respectively.

In all models, the disc is truncated at a magnetospheric radius given by

$$R_{mag} = 5.13 \times 10^8 \mu_{30}^{4/7} \left(\frac{M_1}{M_\odot}\right)^{-1/7} \left(\frac{\dot{M}_{acc}}{10^{16}\, g\, s^{-1}}\right)^{-2/7} cm, \tag{7}$$

where M_1 is the accretor mass in solar units, $\dot{M}_{acc}$ is the accretion rate on to the white dwarf, which differs from $\dot{M}_{tr}$ if the system is not steady, and μ_{30} is the white dwarf magnetic moment in units of 10^{30} G cm^3 (Frank, King & Raine 2002).

2.3 S-curves

On the Σ–T_{eff} plane, accretion disc steady-states, at a given radius, form the well-known 'S-curves'. The upper and lower branches are stable; the intermediate branch is thermally and viscously unstable. As noted earlier, these S-curves are calculated by solving the disc vertical structure. The bends in the S-curves define the critical values of the parameters at which the stability properties of a local disc ring are changing. The numerical fits to these values can be found in Appendix A.

Fig. 1 shows examples of such S-curves obtained for various radii. Fits to the critical surface densities, effective temperatures and corresponding accretion rates are given in Appendix A. These fits are valid for radii in the range 10^8 to 10^{12} cm and for α in the range 10^{-4} to 1. As can be seen, the S-curves do not look very different from those found for smaller discs; the extension to large radii does not change the overall shape of the S-curves, but merely increases typical surface densities and slightly decreases the corresponding effective temperatures. They do, however, differ quite significantly from those used by Alexander et al. (2011), as can be seen from a comparison with their fig. 1. We return to this point in Section 3.1.1. Note also that the extent of the unstable branch is dominated by the jump in the viscosity parameter (Hameury et al. 1998).

2.4 Light-curves

When calculating the light-curves, we include the contributions from the thermal emission of the white dwarf, the (irradiated) secondary star and the hot-spot where the mass-transfer stream hits the disc (see Schreiber, Hameury & Lasota 2003). For the shell-burning sources, we model their emission as that of a black-body with shell luminosity L_{nuc}. The contribution of the red giant is important and more difficult to evaluate, particularly because it may or may not
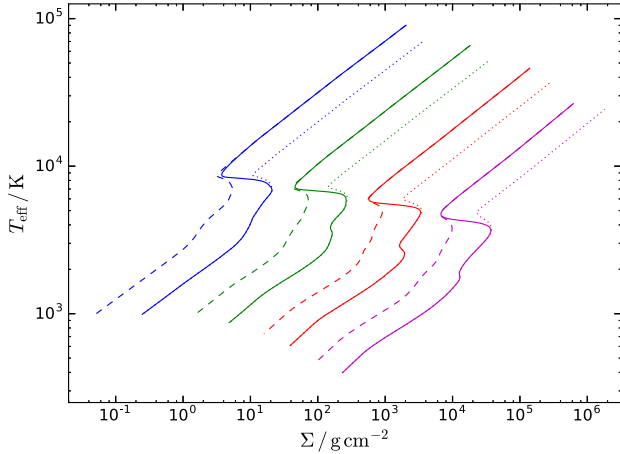
Figure 1. $\Sigma - T_{eff}$ S-curves computed for a 1.35 $M_{\odot}$ white dwarf are plotted for various radii. The four sets of curves (each set includes a dashed, a solid and a dotted), from left to right, represent the S-curves at radii $r = 10^9$, 10^{10}, 10^{11} and 10^{12} cm, respectively. Solid lines represent the S-curves attained from temperature-dependent α. Dashed and dotted lines represent S-curves for fixed $\alpha = 0.1$ and $\alpha = 0.01$ respectively (we use these values for a direct comparison with fig. 1 of Alexander et al. 2011; see Section 3).

fill its Roche lobe. Specific details for RS Oph and Z And are given in the corresponding sections below.

We also account for interstellar reddening, which decreases the observed optical fluxes; the visual extinction is $A_V = 3.1E(B - V)$, where $E(B - V)$ is the colour excess. For RS Oph, we take $E(B - V) = 0.73$ (Snijders 1987). For Z And, we consider the minimum $E(B - V) = 0.27$, as did S2006; values for $E(B - V)$ found in the literature are in the range of 0.27 to 0.35.

3 RS OPHIUCHI

RS Oph is a symbiotic recurrent nova with a recurrence time of about 20 yr. The binary has an orbital period of 453.6 d, a mass ratio $q \equiv M_2/M_1 = 0.6$, and an eccentricity $e = 0$ (Brandi et al. 2009). The low mass of the ejecta of the 2006 outburst (approximately in the range 10^{-7} to 10^{-6} $M_{\odot}$; Sokoloski et al. 2006a) and their high velocity (4000 km s^{-1}; Das, Banerjee & Ashok 2006; Anupama 2008) suggest a white dwarf mass close to the Chandrasekhar limit (see e.g. Yaron et al. 2005, for a study of the dependence of the ejecta characteristics on the system parameters). Other arguments also point towards a high-mass primary (Mikołajewska & Shara

2017). Therefore the mass of the K7 giant (Mürset & Schmid 1999) companion can be estimated to be $M_2 \approx 0.8$ $M_{\odot}$, the inclination is about 50°, and the orbital separation is $a \approx 2.2 \times 10^{13}$ cm.

Fig. 2 shows the long-term light-curve of RS Oph in the visual over the period 1982 to 2017, obtained using AAVSO data. The visual magnitude varies from 11–12 in quiescence to 4.8 at maximum. During weeks 6 to 10 of the last, 2006 outburst, RS Oph was a supersoft X-ray source with luminosity in the range 0.2 to 1.0 keV, close to the Eddington luminosity, and a temperature of the white dwarf photosphere close to 8×10^5 K (Nelson et al. 2008). Nuclear burning ended around day 69 after outburst. The nova shell ejected by RS Oph was asymmetrical and contained a jet-like structure. Although this feature of the outburst motivated King & Pringle (2009) to assert that it was not thermonuclear but resulted from a dwarf-nova instability, the clear signature of nuclear burning observed in RS Oph during the supersoft state makes such a possibility highly improbable.

The giant companion star is probably close to filling its Roche lobe. Estimates of the mass-loss rate vary from about 10^{-8} $M_{\odot}$ yr^{-1} (Iijima 2008) to 10^{-6} $M_{\odot}$ yr^{-1} (Evans et al. 2007). Recent estimates by Booth, Mohamed & Podsiadlowski (2016) give 5×10^{-7} $M_{\odot}$ yr^{-1}.

Until *Gaia* determined the parallax of RS Oph, which corresponds to a distance of 2.26 ± 0.27 kpc (Gaia Collaboration et al. 2018), the distance of 1.6 kpc to RS Oph based on Bode (1987) had usually been assumed, although distances as low as 540 pc (Monnier et al. 2006) and as high as 2.45 kpc (Rupen, Mioduszewski & Sokoloski 2008) had been claimed. For comparison with previous studies, we use here the value of 1.6 kpc, and discuss at the end of this section the impact of the updated distance. The quiescent accretion rate is variable. At day 241 after the 2006 outburst, when optical flickering had resumed, indicating the re-formation of an accretion disc, the accretion rate was estimated to be within 10^{-10} and 10^{-9} $M_{\odot}$ yr^{-1}, depending on the assumed model of mass-loss rate from the secondary (Worters et al. 2007). However, on days 537 and 744, X-ray observations suggest accretion rates between 7×10^{-11} and 5×10^{-9} $M_{\odot}$ yr^{-1}, depending on the emission model and assuming a distance of 1.6 kpc (Nelson et al. 2011). At the true *Gaia* distance of 2.26 kpc, the accretion rates would be respectively 1.4×10^{-10} and 1.0×10^{-8} $M_{\odot}$ yr^{-1}. The presence of an absorbed optically thick boundary layer would allow accretion rates up to 3.2×10^{-8} $M_{\odot}$ yr^{-1} (for a distance of 1.6 kpc; Nelson et al. 2011). However, observations by *ROSAT* PSPC of RS Oph 6 and 7 yr after the 1985 outburst implied quiescent accretion rates in the range of 10^{-12} to a few 10^{-11} $M_{\odot}$ yr^{-1} (Orio 1993; Orio, Covington & Ögelman 2001). Similar results were obtained by Mukai (2008) in 1997. Such low accretion rates have been considered as 'completely
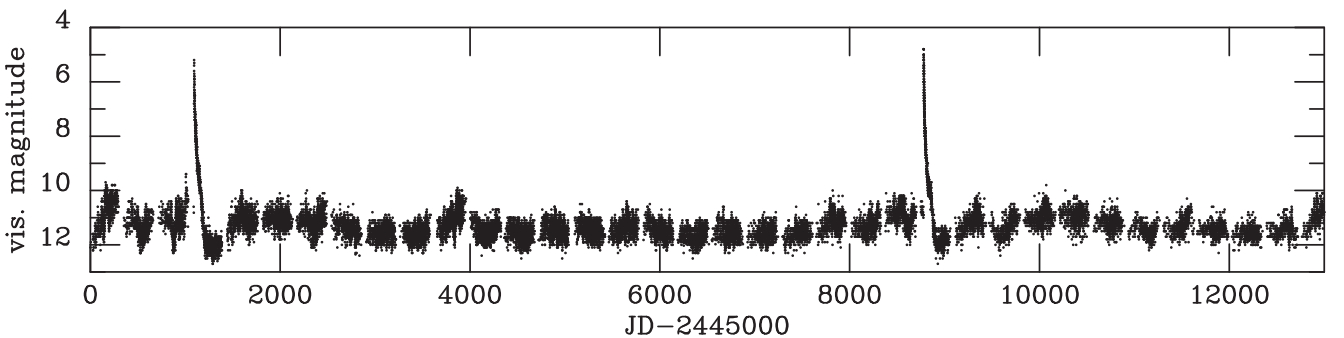
Figure 2. RS Oph visual light-curve (data from AAVSO).

Table 2. Models of RS Oph dwarf nova outbursts.

Model	$R_{in}(qsc)$ [10^{10} cm]	R_D [10^{10} cm]	$\dot{M}_{tr}$ [$M_\odot$ yr^{-1}]
RSB-6	0.215	256.25	10^{-6}
RSB-7	0.215	256.25	10^{-7}
RSB-8	0.215	256.25	10^{-8}
RSB-A*	1.0	253.56	10^{-6}

$R_{in}(qsc)$ is the inner disc radius during quiescence, R_D is the outer disc radius, and $\dot{M}_{tr}$ is the mass-transfer rate from the secondary. * Model closest to Alexander et al. (2011).

at odds with the short nova outburst recurrence time ($\sim$20 years)' (Nelson et al. 2011).

The reason is that a thermonuclear runaway recurrence time of 20 yr requires, for a white dwarf close to the Chandrasekhar limit, an average accretion rate of about 10^{-8} M$_\odot$ yr^{-1} (Yaron et al. 2005). Therefore the highest estimates of both the companion mass-loss rate and the accretion rate on the white dwarf are consistent with a nova outburst occurring every 20 yr. However, since these estimates are model- and distance-dependent, the consistency between the observed properties of RS Oph outbursts and the standard nova-outburst model cannot be assumed with certainty. Since the accretion disc, the presence of which seems to be confirmed by the observed optical flickering and by the necessity of a high accretion efficiency, may extend to a distance large enough to make it thermally and viscously unstable, it is worth investigating whether this instability gives rise to large-scale outbursts and whether these outbursts, if they occur, can drop enough mass on to the white dwarf to trigger a thermonuclear runaway while having, according to the DIM, very low quiescent accretion rates. We also want to test the claim by Alexander et al. (2011) that RS Oph outbursts do not have their origin in thermonuclear runaway but are caused by stable hydrogen-burning at the white dwarf surface, with the burning triggered by dwarf nova outbursts recurring every 20 yr.

3.1 Dwarf nova outbursts of RS Oph

It is not always realized that the presence of a thermally and viscous unstable disc is only a necessary condition for the occurrence of dwarf-nova-type outbursts. For example, accretion discs in active galactic nuclei, even when unstable, do not show large-scale outbursts, for reasons explained by Hameury et al. (2009). It is therefore not obvious a priori what the response of a very large disc to a thermal-viscous instability will be. To study this problem, we calculated a series of models, the parameters of which are given in Table 2.

3.1.1 Unirradiated discs

First, we consider three models for a system with parameters appropriate for RS Oph (RSB-6, RSB-7, RSB-8), corresponding to three different mass-transfer rates from the secondary of 10^{-6}, 10^{-7} and 10^{-8} M$_\odot$ yr^{-1}. To these three models we add RSB-A, which is the closest we could come to the model considered by Alexander et al. (2011).

In all models the mass of the white dwarf is 1.35 M$_\odot$ (see e.g. Hachisu, Kato & Luna 2007) and the assumed distance is 1.6 kpc. In order to be compatible with Alexander et al. (2011), we assume the secondary's temperature to be 3500 K (Schaefer 2009). In order to have a truncated disc, we assume arbitrarily a white dwarf magnetic moment of 2×10^{30} G cm^3. Truncation of the inner disc is necessary
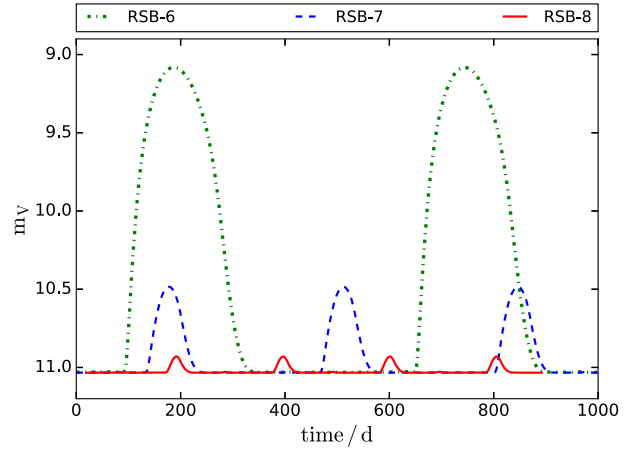
Figure 3. Optical light-curves for the models RSB-6 (dash–dotted green curve), RSB-7 (dashed blue curve) and RSB-8 (solid red curve).

to avoid multiple small outbursts, which are inevitable when the inner disc radius is as small as that of a 1.35 M$_\odot$ white dwarf radius and are a numerical nuisance.

Since the giant companion to RS Oph is not supposed to fill its Roche lobe, the structure of the accretion flow in this system is not clear. In particular, what is the size of the accretion disc that apparently is present during quiescence? For the assumed binary parameters the circularization radius for the Roche-lobe-filling case is $R_{circ}^{RL} = 2.37 \times 10^{12}$ cm (Lubow & Shu 1975), while in the case of wind accretion it is $R_{circ}^{W} < 2.2 \times 10^{11} \lambda(a)^{-4}$ cm, where $\lambda \approx 1$ (Frank et al. 2002). In our code, the average outer disc radius is determined by the tidal torque

$$\mathcal{T}_{tid} = c_{tid} \Omega_{orb} r \nu \Sigma \left(\frac{r}{a}\right)^5, \tag{8}$$

where ν is the kinematic viscosity coefficient and c_{tid} is a numerical coefficient that modulates the tidal truncation radius and provides an average value of the disc outer radius, R_D, when the disc is steady. Here we use $c_{tid} = 3.0 \times 10^9$ such that R_D is of the order of 10^{12} cm, which is appropriate for both cases of mass transfer from the giant companion.

We also simulate the RS Oph system using the same parameters as Alexander et al. (2011), referred to as model RSB-A in Table 2. The masses of the white dwarf and of the secondary are identical to those in RSB-6, -7 and -8, but, in order to have the same circularization radius, $R_c \approx 1.74 \times 10^{12}$ cm, and disc size (slightly larger than R_c) as in their work, we assume the orbital period to be 287.5 d. As in Alexander et al. (2011), the disc is truncated at a fixed inner radius of 10^{10} cm. We also use $\alpha_c = 0.01$ as in their model.

Fig. 3 shows the light-curves obtained for the three models considered here, and Table 3 provides the main outburst characteristics for the RS Oph dwarf nova outbursts. As the mass-transfer rate increases, the recurrence time between outbursts increases and the outbursts last longer too. In none of the models do heating fronts reach the disc outer edge, and the outer radius of the disc does not vary during the outbursts, in contrast to what is seen in smaller discs. During quiescence the typical accretion rate on to the white dwarf is $\dot{M}_{in} \gtrsim 10^{-12}$ M$_\odot$yr^{-1}. The larger the mass-transfer rate, the larger the peak value of $\dot{M}_{in}$ of an outburst. Fig. 4 shows the time variations of the visual magnitude, the mass accretion rate (a proxy for the X-ray emission), and the total disc mass for model RSB-6, which has the longest recurrence time. The small intermediate

Table 3. Disc outburst properties for RS Oph models.

Model	$\dot{M}_{in}$ (qsc) $[\mathrm{M}_\odot\mathrm{yr}^{-1}]$	$\dot{M}_{in}$ (peak) $[\mathrm{M}_\odot\mathrm{yr}^{-1}]$	m_V (qsc)	m_V (peak)	ΔM $[\mathrm{M}_\odot]$	τ_{rec} [d]	τ_{ob} [d]	$R_{f,max}$ $[10^{10}$ cm]
RSB-6	3.8×10^{-12}	4.15×10^{-6}	11.03	9.08	10^{-6}	556	258	56
RSB-7	3.8×10^{-12}	6.3×10^{-7}	11.03	10.48	6.8×10^{-8}	335	115	27
RSB-8	3.8×10^{-12}	9.3×10^{-8}	11.03	10.9	4.5×10^{-9}	205	50	12.7
RSB-A	4.5×10^{-12}	9.6×10^{-6}	11.03	8.25	3.35×10^{-6}	1190	260	70

The first column lists the model reference, the second and third ones give the minimum quiescent and outburst peak of the mass accretion rate. The fourth and fifth columns give the apparent visual magnitude during quiescence and outburst peak respectively. The sixth column gives an estimate of the amount of mass accreted on to the white dwarf during one outburst. The next two columns denote the recurrence time for the outburst and the outburst duration, respectively. The last column gives the largest distance reached by the heating fronts.
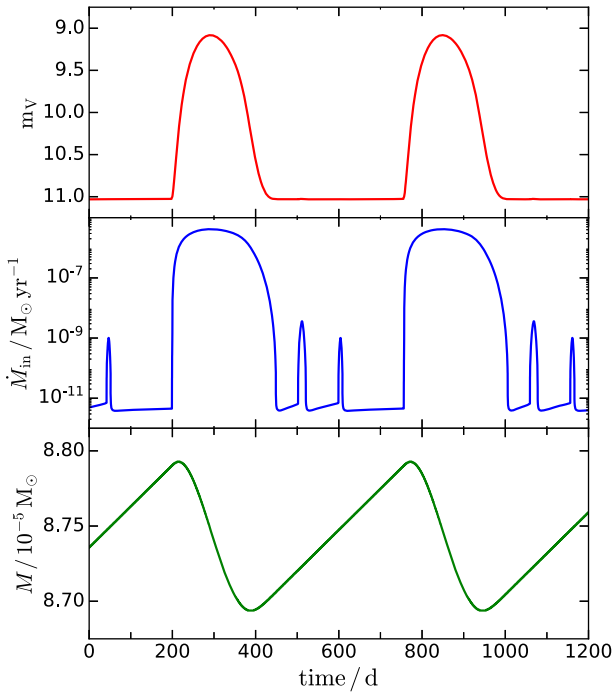
Figure 4. From top to bottom: visual magnitude, accretion rate on to the white dwarf, and disc mass for model RSB-6.

outbursts are not detectable in visible light, but could be marginally detectable in the X-rays.

Since the peaks of $\dot{M}_{in}$, listed in Table 3, are more than three orders of magnitude larger than in quiescence, most of the mass is accreted on to the white dwarf during outbursts only. Table 3 also shows that the visual amplitude of the outbursts is much smaller than the amplitude observed in RS Oph: less than 2 versus 6.5 mag. Furthermore, the recurrence times of the outbursts for models RSB-6, RSB-7 and RSB-8 (from 0.5 to 1.5 yr) are much shorter than the observed 20 yr. Therefore, contrary to the suggestion of King & Pringle (2009), the DIM as such cannot account for the recurrent outbursts of RS Oph.

Finally, we comment on model RSB-A. Our results are very different from those of Alexander et al. (2011): the recurrence time we obtain is shorter than what they obtained for a mass-transfer rate of $10^{-6}\,\mathrm{M}_\odot\,\mathrm{yr}^{-1}$ by a factor of 4, and their outburst duration is longer; as a consequence, in their case the mass accreted on to the white dwarf in a single outburst is an order of magnitude larger than the value of $3 \times 10^{-6}\,\mathrm{M}_\odot$ that we obtain for model RSB-A. These differences may be attributed to the way the disc's vertical structure is treated. Alexander et al. (2011) assume that the disc

is vertically isothermal, and the cooling rates are computed using a one-zone approximation. This approximation is no longer valid if the opacities vary significantly with height in the disc, which is the case during outbursts. Moreover, their effective temperatures are computed with a relationship that holds only for large optical depths (they use $T_{eff} = T_c\tau^{-1/4}$), which is inconsistent with their estimate for the cooling term. In our models, we fully solve the vertical structure. A comparison of our Fig. 1, where we plot the S-curves for RS Oph computed using the same parameters as Alexander et al. (2011), with their fig. 1 illustrates the substantial differences between the two approaches. For example, the Alexander et al. (2011) effective temperatures at the critical surface densities are lower than ours by factors of 3 to 4. This significantly alters the results. It should also be noted that truncating the disc at 10^{10} cm is rather excessive. Magnetic truncation would imply a magnetic moment larger than 3×10^{33} G cm^3, that is, large enough for pulsations at the spin period to be observed.

3.2 'Combination recurrent nova' outbursts of RS Oph

One should still examine the possibility that, by dropping enough mass on the white dwarf surface, dwarf nova outburst(s) trigger a nova outburst. To start a thermonuclear runaway (TNR) in a system with RS Oph parameters, it is necessary to accumulate a mass of $M_{ign} \approx 4 \times 10^{-7}\,\mathrm{M}_\odot$ on the white dwarf surface (Wolf et al. 2013).

We considered this possibility for our three typical models.

RSB-6: In this model, the mass accreted by the white dwarf during a single outburst, $\Delta M \approx 10^{-6}\,\mathrm{M}_\odot$, is larger than M_{ign}, so that one dwarf nova outburst could, in principle, trigger a nova event. The mass M_{ign} is accumulated during the first 90 d of the disc outburst but, by the time this critical mass has been accreted, $\dot{M}_{in}$ exceeds the stable nuclear burning limit, which is $\dot{M}_{stable} = 6 \times 10^{-8}\,\mathrm{M}_\odot\,\mathrm{yr}^{-1}$ (Wolf et al. 2013). $\dot{M}_{in}$ also exceeds the limit $\dot{M}_{RG} = 3\dot{M}_{stable}$ above which hydrogen can be burned as quickly as it is accreted, so that the hydrogen mass increases; therefore, a TNR can occur only during the decay from the outburst maximum, as soon as the accretion rate falls below $\dot{M}_{stable}$, which happens at day 140 after the outburst is triggered. The early phases of the outburst, corresponding to a change in visual magnitude of about 2, could be just visible in the optical (Adamakis et al. 2011) but would be easy to detect in the X-rays because the accretion rate increases by six orders of magnitude. Of course, for such a scenario to work, the rate at which mass is transferred to the disc must be of the order of $10^{-6}\,\mathrm{M}_\odot\,\mathrm{yr}^{-1}$, which implies that most of the mass lost by the companion must end up in the accretion disc. This is far from being guaranteed, but this tight requirement could be relaxed if disc self-irradiation were taken into account, allowing more mass to be accreted with a lower accretion rate (see below).

Table 4. Disc outburst properties for RS Oph irradiated models.

Model	$\dot{M}_{in}$ (qsc) [$M_\odot yr^{-1}$]	$\dot{M}_{in}$ (peak) [$M_\odot yr^{-1]}$]	m_V (qsc)	m_V (peak)	ΔM [$M_\odot$]	τ_{rec} [d]	τ_{ob} [d]	$R_{f,max}$ [10^{10} cm]
RSB-6-I	1.25×10^{-12}	4.05×10^{-6}	11.03	9.09	5.08×10^{-6}	1340	538	72.7
RSB-7-I	1.45×10^{-12}	1.17×10^{-6}	11.03	10.15	3.9×10^{-7}	1530	305	43
RSB-8-I	1.44×10^{-12}	1.1–2.4×10^{-7}	11.03	10.85	1.5–3.9×10^{-8}	935-1335	135-140	16.8-22.5

Columns are the same as in Table 3

The quiescent accretion rate corresponds to 1991, 1992 *ROSAT* PSPC and 1997 *ROSAT* post-1985 outburst observations. The higher post-2006 accretion rates observed by *Chandra* and *XMM–Newton* could coincide with 'mini-outbursts' observed in the model light-curve. The main problem with this scenario is that, because each dwarf nova outburst is able to trigger a TNR, the recurrence time is very short, of the order of 1.5 yr, which is more than an order of magnitude shorter than observed.

RSB-7: For this model, M_{ign} is accumulated during six dwarf nova outbursts in about 5 yr. The quiescent accretion rate is the same as in RSB-6, because of the same disc truncation. Between thermonuclear eruptions, the accretion rate would increase due to dwarf nova outbursts that, in this case, are unable to trigger TNRs. They would be invisible in the optical but could be detected in the X-rays.

RSB-8: For this model, M_{ign} is accumulated during 80 dwarf nova outbursts during a period of around 45 yr. As for the preceding model, these disc outbursts would be unobservable in the optical, but the increased accretion rate could be detected through X-ray observations during most of the 50 d of activity.

We conclude that a model with an accretion rate between those of RSB-7 and RSB-8 (a mass-loss rate from the companion of a few times 10^{-8} $M_\odot$ yr^{-1}) can explain most of the properties of the RS Oph recurrent nova outbursts. The mass necessary for a TNR is accumulated during 20 yr in a series of 15 to 20 dwarf nova outbursts. Such a scenario has the advantage of naturally explaining the discrepant X-ray observations at different quiescent epochs of the RS Oph outburst cycle: low values correspond to the quiescent disc phase, while high X-ray luminosities correspond to one of the dwarf nova outbursts.

3.3 *Self-irradiated discs*

We note from the results of the previous section that the accretion rate at the inner edge becomes quite high during outbursts, and can therefore lead to significant irradiation effects in the outer parts of the accretion disc (see equation 2), because the white dwarf is massive. Here we consider irradiation using equation (1) for the entire disc. This is appropriate because irradiation effects are important only in the outer disc. We consider models similar to the three that we discussed above – RSB-6-I, RSB-7-I, RSB-8-I – with the irradiation coefficient $\mathcal{C} = 0.005$. The results are shown in Table 4, and the light-curves (*V* magnitude) are shown in Fig. 5.

RSB-6-I: $\dot{M}_{in}$ at maximum is almost the same as in the unirradiated case, but the outburst lasts longer and the mass deposited on the white dwarf during an outburst is five times larger. The recurrence time is 2.5 times longer than for RSB-6, but this is still not consistent with the observations; roughly five outbursts are expected to occur in a 20-yr span, and each outburst can trigger a TNR. As before, one can therefore reject this model.
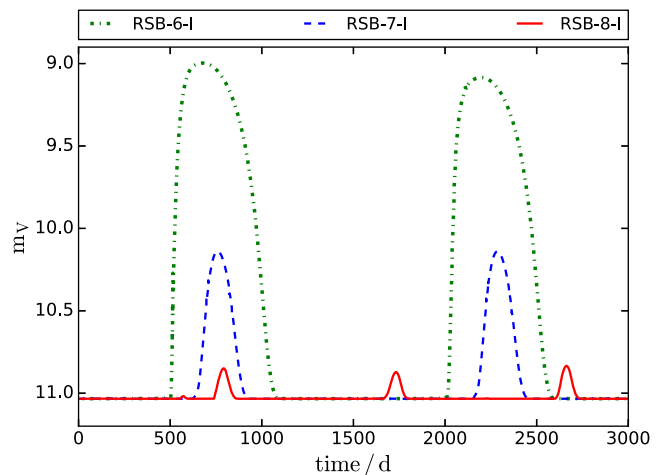
Figure 5. Optical light-curves for irradiated models of RS Oph: RSB-6-I (dash–dotted green curve), RSB-7-I (dashed blue curve) and RSB-8-I (solid red curve).

RSB-7-I: Irradiation has a significant impact in this model. The $\dot{M}_{in}$ peak is roughly 1.85 times that obtained for RSB-7. The mass deposited on the white dwarf during an outburst is very close to M_{ign} and could trigger a recurrent nova, in contrast to RSB-7 for which at least six outbursts were required to accrete the same mass. The recurrence time is 4.5 times longer than for RSB-7, but because of the increased accumulated mass during a single outburst, roughly four to five outbursts are expected to occur in a 20-yr span. Each outburst can again trigger a TNR. For this reason, this model also conflicts with the observations.

RSB-8-I: Irradiation effects are the strongest of the three models we considered. Here, we obtain a cycle of slightly different outbursts – hence the range given in Table 4 for this model. These outburst properties, however, do not vary by more than a factor of 2. Both the peak accretion rate and the mass accreted during an outburst are an order of magnitude larger than in the case of RSB-8, but the mass accreted during a single outburst is clearly less than the ignition mass. Now 18 outbursts are required to accrete the ignition mass, and a recurrent nova can be triggered once every 55 yr. Although more mass is accreted when irradiation is taken into account, the recurrence time is also significantly increased, and the time required to trigger a recurrent nova is similar to in the RSB-8 case.

We therefore conclude that, as for the unirradiated case, if dwarf nova outbursts are to be recurrent nova triggers, the mass-transfer rate must lie in the range from 10^{-7} to 10^{-8} $M_\odot$ yr^{-1}. This is therefore a general conclusion, independent of the magnitude of the irradiation effect.
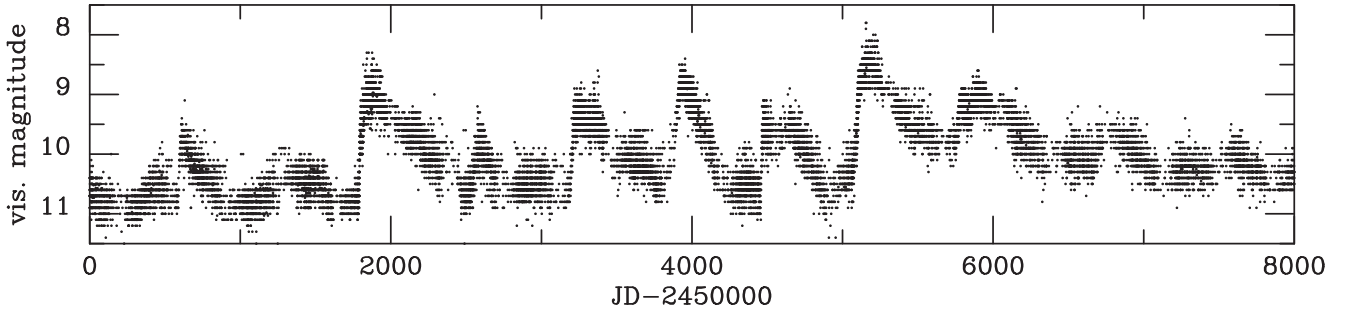
Figure 6. Z And visual light-curve (data from AAVSO).

3.4 Are dwarf novae needed to trigger RS Oph TNR outbursts?

Finally, we should check whether a more conventional scenario, not involving dwarf nova outbursts, can explain the RS Oph recurrent nova outbursts. A steady accretion rate of 2×10^{-8} M$_\odot$ yr^{-1} is sufficient to accumulate the mass M_{ign} corresponding to the RS Oph parameters. A disc in a system with RS Oph binary parameters is stable if the rate at which it is fed mass satisfies the inequality $\dot{M}_{\text{tr}} > \dot{M}_{\text{crit}}^+$, where the stable hot-disc minimal accretion rate is (equation A5)

$$\dot{M}^+ = 1.44 \times 10^{-10} \alpha_{\text{h}}^{-0.008} m_{\text{wd}}^{-0.88} R_{\text{D},10}^{2.67} \ \text{M}_\odot \ \text{yr}^{-1}; \tag{9}$$

m_{wd} is the white dwarf mass in solar units, and $R_{\text{D},10}$ is the outer disc radius in units of 10^{10} cm. For $\dot{M}_{\text{tr}} > 2 \times 10^{-8}$ M$_\odot$ yr^{-1}, an accretion disc with an outer radius $R_\text{D} < 7.4 \times 10^{10}$ cm is stable with respect to the thermal-tidal instability. This is quite small, but marginally possible if accretion occurs via a wind (the circularization radius must be smaller than the disc size). In such a scenario there would be no direct explanation for the low accretion rate deduced from *ROSAT* and *ASCA* observations, and one would be left with speculations of the type presented by Mukai (2008), who suggested that RS Oph might be a fast rotator with essentially no boundary layer. Note that this scenario is inconsistent with our assumption of a significant magnetic field.

3.5 *Gaia* revised distance

We finally comment on the recently updated distance of $2.26 \pm .27$ kpc by *Gaia* (Gaia Collaboration et al. 2018), a 40 per cent increase with respect to the distance we have used here. With this new distance, the optical magnitude of the entire light-curve would increase by 0.7 mag, all model parameters being kept at their previous values. In order to still account for the observed quiescent luminosity, the secondary temperature has to be increased to 3800 K; the outburst amplitude is then reduced by a factor of less than 2, all other parameters being unaltered. The (undetected) dwarf nova outbursts of RS Oph would thus be slightly fainter, but the total mass accreted on to the white dwarf surface as well as the sequence of dwarf nova outbursts and nova eruptions remain exactly the same as previously and our conclusions for RS Oph remain unaltered.

4 Z ANDROMEDAE

Z And is a classical symbiotic star consisting of an $M_1 = 0.65 \pm 0.28$ M$_\odot$ (Schmid & Schild 1997) white dwarf and a giant secondary with mass ratio $M_2/M_1 \approx 2.0$. Its orbital period is 759 d (Formiggini & Leibowitz 1994) and the inclination is $59^{+1}_{-2}{}^\circ$

(Skopal & Shagatova 2012). Until recently, the distance to Z And was estimated to be 1.2 ± 0.5 kpc (Kenny 1995), but the recent parallax measured by *Gaia* (Gaia Collaboration et al. 2018) puts Z And at a distance of 1.95 ± 0.078 kpc. As for RS Oph, we use here the old value of 1.2 kpc for comparison with previous studies, and comment at the end of this section on the impact of increasing the distance by 70 per cent. The presence of a magnetized (10^4 to 10^6 G) primary is deduced from observations of persistent optical pulsations at a period of 28 min (Sokoloski & Bildsten 1999).

As in most classical symbiotic stars, the white dwarf in Z And (the hot component) exhibits a quasi-steady luminosity component of about 10^3 L$_\odot$ attributed to thermonuclear shell-burning of hydrogen at a rate of a few times 10^{-8} M$_\odot$ yr^{-1} (see e.g. S2006). Symbiotic stars undergo outbursts, the most common of which are *classical symbiotic outbursts*, whose origin is unknown. Their high peak luminosities exclude dwarf-nova-type outbursts, while their high repetition frequency rules out TNRs of the recurrent-nova type. In contrast to recurrent novae, white dwarfs in these symbiotic systems have low masses, precluding short recurrence times.

Fig. 6 shows the visual light-curve of Z And from 1995 to 2017, obtained using AAVSO data. The light-curve is complex and displays a variety of outbursts of different amplitudes and durations, which are not necessarily caused by the same mechanism.

In 1997, the Z And light-curve showed a low-amplitude (about 1 mag) outburst in the *V* light, with a rise-time shorter than about 20 d followed by a decay lasting about 200 d (first outburst in Fig. 6). The asymmetric outburst shape prompted S2006 to suggest that the 1997 outburst was caused by a dwarf-nova-type instability of the outside-in type; that is, with an outburst starting in the outer disc regions (see e.g. Buat-Ménard et al. 2001). A more powerful outburst was observed in 2000 to 2002, when after a rise similar to the 1997 event the brightness kept increasing to reach a 2 mag amplitude in optical, corresponding to a bolometric luminosity of about 10^4 L$_\odot$ (second outburst in Fig. 6, starting at JD $\approx$ 2451800). If accretion-powered, this high-state would correspond to an accretion rate of $\dot{M} \gtrsim 10^{-5}$ M$_\odot$ yr^{-1}. Such a high accretion rate would have to be sustained for a full year during which the system maintained a luminosity close to its maximum (S2006). Since this seems unlikely, S2006 proposed that this event is a 'combination nova' outburst, in which a dwarf nova outburst triggered increased shell nuclear burning. In order to test S2006's hypothesis we calculate models of disc outbursts in Z And using our DIM code, adapted to the physical properties of this system.

4.1 Dwarf nova outbursts of Z And

As in the case of RS Oph, it is not clear how in Z And the mass lost by the giant companion forms an accretion disc around the white

dwarf. The orbital separation of Z And is $a = 3.053 \times 10^{13}$ cm, which corresponds to a circularization radius of $R_{\rm circ} = 2.085 \times 10^{12}$ cm. In the case of wind accretion, the circularization radius would be 1.34×10^{10} cm, assuming that the wind speed is equal to the escape speed from the giant, $\lambda(a) \approx 1$.

Since the critical accretion rate at $R_{\rm circ}$ is (equation A5) 2.95×10^{-4} M$_\odot$ yr^{-1}, a non-irradiated disc in Z And is thermally and viscously unstable for all realistic (less than 10^{-4} M$_\odot$ yr^{-1}) mass-transfer rates. However, outbursts of Z And should differ in several aspects from those observed in normal dwarf novae.

First, the presumed radius of the accretion disc in Z And, $R_{\rm D} \approx 1.4$–2.8×10^{12} cm (S2006), is one or two orders of magnitude larger than that in dwarf novae, which, as noted by Duschl (1986b), can have dramatic effects on the heating and cooling front propagation (see e.g. Menou et al. 2000; Dubus et al. 2001, and Section 3.1 about RS Oph).

Secondly, the disc is irradiated by a constant white dwarf surface luminosity of about 10^3 L$_\odot$, corresponding to an effective temperature of 150 000 K, while temperatures of white dwarfs in dwarf novae are an order of magnitude lower (see e.g. Urban et al. 2000). Finally, the observed visual light-curves have a major contribution from the giant companion (Duschl 1986b; Kenyon 1986), and the duration of the outbursts is shorter than the orbital period, which might provide an additional source of variability.

Thirdly, according to S2006, the asymmetric shape of the 1997 outburst light-curve suggests an *outside-in* event (i.e. an outburst in which the heating front propagates inwards from the outer disc regions) if it is interpreted as a dwarf nova outburst (Smak 1984). It should be noted, however, that 'fast-rise–slow-decay' light-curves can also be produced by outbursts starting near the inner disc radius. This happens, for example, in the case of truncated and/or irradiated discs. In addition, outside-in outbursts are unlikely to occur in very large discs.[1] The criterion for an outside-in outburst can be written (Lasota 2001) as

$$\dot{M}_{\rm tr} \gtrsim \frac{0.5}{\sqrt{\delta}} \dot{M}_{\rm crit}^-, \tag{10}$$

where $1 < \delta \lesssim 2$,

$$\dot{M}_{\rm crit}^- = 1.15 \times 10^{-5} \alpha_{\rm c}^{-0.02} \left(\frac{M_1}{{\rm M}_\odot} \right)^{-0.88} R_{D,12}^{2.65} \ {\rm M}_\odot \ {\rm yr}^{-1} \tag{11}$$

is the critical (maximal) accretion rate for a cold and stable accretion disc (equation A6), and $R_{D,12}$ is the disc radius in units of 10^{12} cm. For the Z And parameters, equation (10) implies rather unrealistically high mass-transfer rates, larger than about 10^{-5} M$_\odot$ yr^{-1}.

4.1.1 Non-irradiated disc

We will first check the S2006 suggestion that the disc instability model can explain the asymmetrical, 1-mag feature observed in 1997 in the visual light-curve of Z And. In order to separate and evaluate the various components contributing to the light-curve of a hypothetical dwarf-nova-type outburst of Z And, we first consider the case of a non-irradiated disc. We assume a white dwarf magnetic moment of 5.12×10^{31} G cm^3, which corresponds to a magnetic field close to 10^5 G. Our results do not depend significantly on the accretor's magnetic moment.

[1]Model outbursts for LMXB parameters are always of the inside-out type (Dubus et al. 2001).

In calculating the visual light-curves, we include the contribution of the giant companion in a different way from Schreiber et al. (2003). Their approach is well suited to a Roche-lobe-filling, low-mass companion but it is not applicable to the case of Z And. We considered separately the following two extreme simplified assumptions:

(a) The secondary luminosity does not change in response to irradiation. This is appropriate if for example the irradiated side is not facing the observer. The secondary contribution is fixed to be 10.8 mag.

(b) The response of the secondary luminosity to irradiation is maximal. This is appropriate if the irradiated side of the secondary is facing the observer, and if the secondary radius is as large as possible. In this case, we use the minimum acceptable secondary effective temperature, which we take to be 2900 K, and estimate the radius that would correspond to the Z And quiescent visual magnitude (10.5 mag); the secondary radius is then found to be 110 R$_\odot$, so the secondary fills 57 per cent of its Roche lobe.

We found that the two prescriptions produce very similar light-curves, and in what follows we present light-curves calculated using assumption (b) only.

We consider outburst models for three mass-transfer rates: ZAB-8, ZAB-7 and ZAB-6 for respectively $\dot{M}_{\rm tr} = 10^{-8}$, 10^{-7} and 10^{-6} M$_\odot$ yr^{-1}. We assume $\alpha_{\rm c} = 0.02$ and $\alpha_{\rm h} = 0.1$, and choose $c_{\rm tid}$ so that the outer disc radius is $R_{\rm D} = 2.37 \times 10^{12}$ cm. Following S2006, we assume a distance of 1.2 kpc, for the purpose of comparing our results with their work, although we shall later comment on the recently updated distances by *Gaia*.

The properties of these three models are presented in Table 5. It can be seen that only model ZAB-6 produces a visual amplitude not too different from 1 mag; however, the shape of the outburst light-curve is markedly different from that observed in 1997 in Z And. The rise-time (73 d) is three times longer than that observed, while the decay-time (118 d) is roughly half that observed. The light-curve shown in Fig. 7 is typical of an inside-out outburst, namely of an outburst starting in the inner disc region. Indeed, the inner disc radius during quiescence, given by equation (7) with $\mu_{30} = 51.2$ and $\dot{M}_{\rm acc} = 3.3 \times 10^{-11}$ M$_\odot$ yr^{-1}, is equal to $R_{\rm in} = 0.82 \times 10^{10}$ cm, whereas the heating front starts propagating at $R_{\rm trig} = 4.05 \times 10^{10}$ cm. While the inner disc edge reaches the white dwarf surface, this front propagates out to $R_{\rm f,max} = 40 \times 10^{10}$ cm, far from the outer disc rim. The outermost disc regions are not affected by the fronts, and the outer disc radius remains fixed because the amount of angular momentum deposited by the outburst is too small to affect it in a significant way.

Although the visual amplitude is small, the accretion rate at the inner edge increases by several orders of magnitude, by a factor of about 10^5 in the case of model ZAB-6 (see Fig. 8). At maximum, the inner edge is squeezed by accretion on to the white dwarf surface (the white dwarf radius $R_{\rm WD} = 8.56 \times 10^8$ cm), and for this model the corresponding accretion luminosity reaches 2600 L$_\odot$, which should be emitted mostly in the extreme ultraviolet. This is consistent with the observed increase of the white dwarf temperature from 150 000 to 180 000 K during the 1997 outburst. The mass dropped on to the white dwarf during a ZAB-6 outburst is 5.6×10^{-7} M$_\odot$.

Since models ZAB-7 and ZAB-8 reproduce neither the shape nor the amplitude observed during the 1997 outburst, the only potential candidate for a model explanation of this event is ZAB-6, corresponding to an accretion rate of 10^{-6} M$_\odot$, which is two to three orders of magnitude larger than the mass-transfer rate considered to be typical of systems such as Z And (S2006). Therefore the 1997

Table 5. Outburst properties of Z And non-irradiated disc models.

Model	$\dot{M}_{\rm in}$ (qsc) [$M_\odot$ yr^{-1}]	$\dot{M}_{\rm in}$(peak) [$M_\odot$ yr^{-1}]	Δm_V	ΔM [$M_\odot$]	$R_{\rm trig}$ [10^{10} cm]	$R_{\rm f,max}$ [10^{10} cm]	$\tau_{\rm rise}$ [d]	$\tau_{\rm dec}$ [d]	$\tau_{\rm rec}$ [d]
ZAB-6	3.3×10^{-11}	3.4×10^{-6}	0.8	5.6×10^{-7}	4.05	40	73	118	355
ZAB-7	3.3×10^{-11}	5.2×10^{-7}	0.2	4.0×10^{-8}	2.15	19	30	46	208
ZAB-8	3.3×10^{-11}	8.4×10^{-8}	0.05	3.1×10^{-9}	1.5	10	14	18	143

The first column lists the models, the second column gives the value of the accretion rate during quiescence, the third column gives the accretion rate attained during the peak of the outburst. The fourth column gives the outburst amplitude in visual magnitudes. The next column contains an estimate of the amount of mass accreted on to the white dwarf during the outburst. The following two columns provide respectively the radii at which the heating front starts and finishes its propagation. The next two columns give the outburst rise and decay times observed in *V*. The final column gives the recurrence time between outbursts.
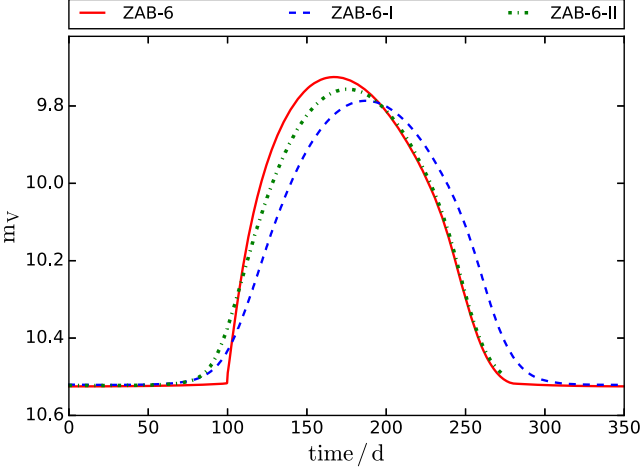
Figure 7. Visual light-curve of dwarf nova outbursts for the models ZAB-6 (solid red curve), ZAB-6-I (dashed blue curve) and ZAB-6-II (dash–dotted green curve). The properties of the light-curves are given in Tables 5 and 6.
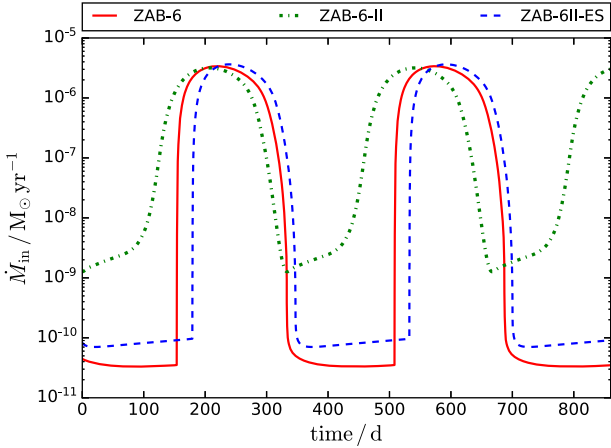
Figure 8. Accretion rate at the inner disc edge during outburst for models ZAB-6 (solid red curve), ZAB-6-II (dash–dotted green curve) and ZAB-6II-ES (dashed blue curve).

outburst would have to be related to an increase in the mass-transfer rate and could not be a pure dwarf nova outburst. It would be similar to dwarf nova *superoutbursts* according to the interpretation of Hameury, Lasota & Warner (2000) and Smak (2008).

The Z And accretion disc is irradiated, however, and its structure can be substantially affected by irradiation. We discuss the impact of irradiation in the next subsection.
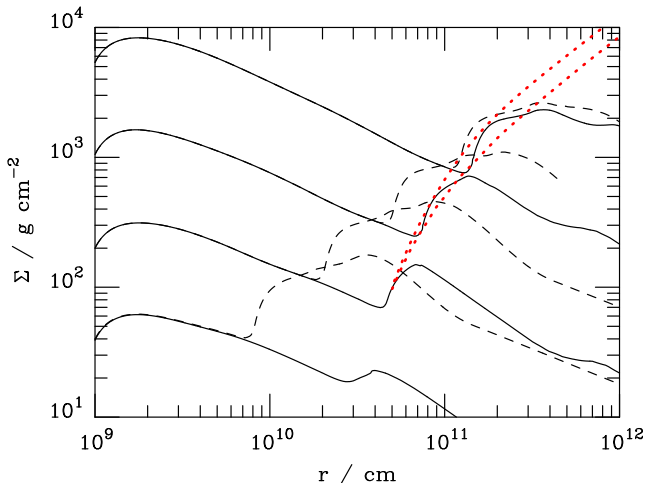
4.1.2 Irradiated discs

In this section we consider irradiation, under two different assumptions for the irradiation efficiency at the outer disc.

4.1.2.1. Fully irradiated discs. We first consider the case in which irradiation by both nuclear burning at the white dwarf surface and accretion modify the structure of the entire disc (i.e. both inner and outer regions). As mentioned in Section 2.1, when the disc scale-height *H* is such that $H/R_{\rm WD} < 1$, we use the extended source formula given by equation (5), with $T_{\rm irr,S}^4 = T_*^4 + T_{\rm eff}^4$ (Hameury et al. 1999). For $H/R_{\rm WD} > 1$ we use equation (1) with $L = L_* + L_{\rm acc}$.

We consider the same three mass-transfer rates as before, but with two sets of irradiation parameters: a strong irradiation case, ZAB-6-I, ZAB-7-I and ZAB-8-I with $1 - \beta = 0.03$ and $\mathcal{C} = 0.002$; and a weaker irradiation case, ZAB-6-II, ZAB-7-II and ZAB-8-II with $1 - \beta = 0.01$ and $\mathcal{C} = 0.001$. Since we do not have direct (or even indirect) information about disc irradiation in Z And or similar systems we use parameters similar to those used in modelling dwarf novae and X-ray transient systems. There is no guarantee that this choice is adequate, but, as we shall see, the results are fairly insensitive to irradiation parameters, at least as far as the main properties of the light-curves are concerned.

Constant irradiation of the outer disc has a different effect on disc stability from accretion self-irradiation, the luminosity of which is proportional to the accretion rate. A comparison of Fig. 9 with figures 8 and 9 of Dubus et al. (1999) shows that in both cases irradiation extends the radius of the hot stable portion of the disc, but in the case of constant irradiation this effect increases with decreasing accretion rate so that discs with accretion rates lower than about 10^{17} g s^{-1} are fully *thermally* stable. Our model ZAB-8-I (corresponding to an accretion rate of 6.3×10^{17} g s^{-1}) is locally unstable, but because of the stabilizing effects of the radial terms in the time-dependent energy-conservation equation (the term proportional to *J* in equation 7 of Dubus et al. 2001) no outburst is produced.

Outbursts in a disc irradiated by a constant-luminosity source (which dominates except at maximum in the ZAB-6 models) are different from those occurring in non-irradiated discs or in self-irradiated discs of soft X-ray transient sources. They consist of reflections of heating and cooling fronts travelling between two radii defined as $R_{\rm f,min}$ and $R_{\rm f,max}$. This can be seen in Fig. 10, for ZAB-6-I and ZAB-6-II, where the fronts propagate between $R_{\rm f,max}$ and $R_{\rm f,min}$, so that the cooling fronts never reach the inner disc radius shown by the dashed lines. This is a major difference from ZAB-6, in which the cooling front can propagate to the disc inner edge and bring the full disc into quiescence. As a result of the irradiation, the inner disc is kept hot during the whole outburst cycle, which produces cooling-front reflections, whereas, as in the non-irradiated case, the heating front is stopped well before reaching the disc outer rim. In contrast to the case of soft X-ray transients (Dubus et al. 2001),

Figure 9. Column density ($\Sigma(R)$) profiles of stationary discs around a 0.65 $M_\odot$ white dwarf irradiated by a constant luminosity $L = 4 \times 10^{36}$ erg s^{-1}. Disc irradiation is described by equation (1), with parameters $\mathcal{C} = 0.002$ and $\alpha = 0.1$. The accretion rates from bottom to top are 10^{16}, 10^{17}, 10^{18} and 10^{19} g s^{-1}. Dashed lines represent non-irradiated discs; full lines correspond to discs irradiated by a constant luminosity. The position of the critical column densities Σ^+ and Σ^- are marked by two dotted red lines intersecting at $r = 5 \times 10^{10}$ cm, $\Sigma = 100$ g cm^{-2}.
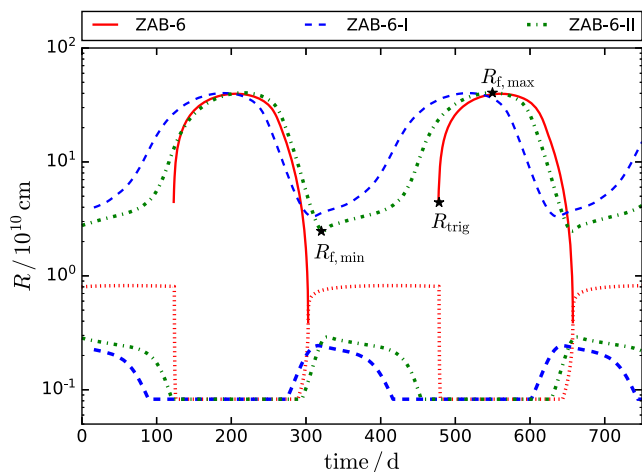
Figure 10. Position of heating/cooling fronts during outbursts for models ZAB-6, ZAB-6-I and ZAB-6-II (top red solid, blue dashed and green dash–dotted curves, respectively). The positions of the inner disc radius during the outburst for these models are also shown (bottom curves), using the same line-styles except for the ZAB-6 model (red dotted curve). The radius at which the instability is triggered, $R_{\rm trig}$, is marked for the second of the ZAB-6 outbursts. Similarly, the maximum radius $R_{\rm f,max}$ reached by the heating front and the minimum radius $R_{\rm f,min}$ reached by the cooling front are indicated for the second of the ZAB-6-II outbursts.

disc truncation does not suppress reflares because the irradiation is dominated by its constant component, independent of the accretion rate. Although the disc never fully enters into quiescence, the light-curve shows clear, well-separated outbursts, with quiescent intervals during which the optical light is dominated by the secondary, and it is thus possible to define the same parameters $\tau_{\rm rec}$, $\tau_{\rm rise}$, $\tau_{\rm dec}$ describing the outburst properties as previously.

The resulting visual light-curves (see Fig. 7 and Table 6 for the outburst parameters) for the case of the highest mass-transfer rate, $\dot{M}_{\rm tr} = 10^{-6}$ M$_\odot$ yr^{-1}, are similar to those obtained in the non-irradiated case, but more symmetric. Since the heating fronts reach similar radii, the peak accretion rate is roughly the same as for non-irradiated discs, and a comparable amount of mass is dropped by an outburst on to the white dwarf. The shape of the visual light-curves is even more unlike to that observed during the 1997 outburst of Z And. For lower mass-transfer rates, the outbursts we obtain are weaker than in the non-irradiated case and cannot really be qualified as outbursts. As before, in order to obtain the correct amplitude, the mass-transfer rate has to be increased by two orders of magnitude.

4.1.2.2. Inner disc irradiation only. One could reasonably argue that describing outer disc irradiation in Z And using the LMXB formalism adapted to the symbiotic case does not make much sense. First, even in the case of LMXBs it is not clear how and why their outer discs are irradiated (Tuchman, Mineshige & Wheeler 1990; Dubus et al. 1999; Tetarenko et al. 2018b), even if observations clearly show that they are (see e.g. van Paradijs & McClintock 1995). Secondly, in LMXBs the illuminating radiation is much harder than it is in the case of Z And. One could therefore argue that in the case of symbiotic systems the effect of outer disc irradiation is negligible. This is why we have made another test of the hypothesis that some symbiotic outbursts, those of Z And in particular, are dwarf nova outbursts or are triggered by them, using a different assumption about the irradiation effects. We now assume that irradiation is given by equation (5) throughout the disc, whatever the value of H/R_*, so that irradiation becomes very small for large radii. The irradiation flux now varies as R^{-3} for large values of R.

As before, we tried two cases: 'I', with $1 - \beta = 0.03$; and 'II', with $1 - \beta = 0.01$. However, since the results are almost indistinguishable we present in Table 7 results only for ZAB-6-II-ES, ZAB-7-II-ES and ZAB-8-II-ES, where 'ES' means that only inner disc irradiation is taken into account.

In contrast to the fully irradiated case, the cooling fronts are able to propagate to the inner disc radius; this is because, during decay, the inner disc radius becomes large and the irradiation flux, when calculated using equation (5), becomes small. This does not, however, lead to outbursts that differ in a very significant way from those obtained previously.

For the highest accretion rate (10^{-6} M$_\odot$ yr^{-1}), the model light-curves are very similar to that calculated for non-irradiated discs, as can be seen in Figs 7 and 8. They are also not much different from the light-curves obtained for a fully irradiated disc. This is not surprising, because the importance of constant irradiation diminishes with increasing accretion rate and because, owing to the low white dwarf accretion efficiency, self-irradiation is (almost) never dominant.

Differences in light-curves are more prominent for lower accretion rates, but these produce neither amplitudes nor shapes comparable to these observed.

4.2 Combination-nova outbursts of Z And

As noted above, S2006 suggest that the 2000 to 2002 eruption of Z And was powered by an increase in nuclear shell-burning on the white dwarf surface triggered by mass influx added by a dwarf nova outburst. They noticed that this event seems to begin like the 1997 outburst (which they assume to be a dwarf nova outburst), but

Table 6. Outburst properties of Z And irradiated disc models. I - fully irradiated discs.

Model	$\dot{M}_{\mathrm{in}}(\mathrm{qsc})$ [$M_\odot$ yr^{-1}]	$\dot{M}_{\mathrm{in}}(\mathrm{peak})$ [$M_\odot$ yr^{-1}]	Δm_{V}	ΔM [$M_\odot$]	$R_{\mathrm{in,qsc}}$ [10^{10} cm]	$R_{\mathrm{f,min}}$ [10^{10} cm]	$R_{\mathrm{f,max}}$ [10^{10} cm]	τ_{rise} [d]	τ_{dec} [d]	τ_{rec} [d]
ZAB-6-I	2.96×10^{-9}	2.98×10^{-6}	0.7	4.63×10^{-7}	0.24	3.3	40.2	122	123	335
ZAB-7-I	3.04×10^{-9}	2.65×10^{-7}	0.13	1.51×10^{-8}	0.23	3.6	16.1	65	57	129
ZAB-8-I	–	–	–	–	–	–	–	–	–	–
ZAB-6-II	2.02×10^{-9}	3.16×10^{-6}	0.76	4.98×10^{-7}	0.29	2.5	40.5	110	116	335
ZAB-7-II	1.61×10^{-9}	3.44×10^{-7}	0.16	2.11×10^{-8}	0.29	2.5	17.0	55	52	142
ZAB-8-II	2.05×10^{-9}	2.17×10^{-8}	0.0017	4.02×10^{-10}	0.25	2.9	6.7	20	20	44

Columns are the same as in Table 5.

Table 7. Outburst properties of Z And irradiated disc models. II – inner irradiation only.

Model	$\dot{M}_{\mathrm{in}}(\mathrm{qsc})$ [$M_\odot$ yr^{-1}]	$\dot{M}_{\mathrm{in}}(\mathrm{peak})$ [$M_\odot$ yr^{-1}]	Δm_{V}	ΔM [$M_\odot$]	$R_{\mathrm{in,qsc}}$ [10^{10} cm]	R_{trig} [10^{10} cm]	$R_{\mathrm{f,max}}$ [10^{10} cm]	τ_{rise} [d]	τ_{dec} [d]	τ_{rec} [d]
ZAB-6-II-ES	7.0×10^{-11}	3.63×10^{-6}	0.84	5.9×10^{-7}	0.67	4.17	40.2	64	108	352
ZAB-7-II-ES	7.0×10^{-11}	5.45×10^{-7}	0.22	4.17×10^{-8}	0.66	2.28	18.8	28	44	212
ZAB-8-II-ES	7.0×10^{-11}	8.11×10^{-8}	0.52	2.76×10^{-9}	0.66	0.87	8.8	13	17	139

Columns are the same as in Table 5

reaches a luminosity close to 10^4 L$_\odot$ and lasts for more than a year. In addition, observation of the ejection of an optically thick shell of material excludes a dwarf nova outburst and points to a milder version of a nova event. S2006 proposed that this was a disc-instability-triggered thermonuclear eruption and called it a 'combination nova'. They estimated from observations that the mass dropped on to the white dwarf during the 1997 outburst was approximately 10^{-7} M$_\odot$. The mass of the burning shell was about 2×10^{-5} M$_\odot$, and S2006 consider that adding 1 to 10 per cent of the shell mass should be sufficient to trigger a shell thermonuclear flash.

We do not address here the problems that such an interpretation poses for models of nuclear burning on the surface of a white dwarf mentioned by S2006 but consider only the viability of the dwarf nova component of the combination nova. As we have shown above, a dwarf nova outburst of a disc with Z And parameters can provide more than about 10^{-7} M$_\odot$ only if the mass-transfer rate is close to 10^{-6} M$_\odot$ yr^{-1}. Therefore such an outburst must be preceded by an increase of the mass-transfer rate by 2 orders of magnitude, because the long-term rate is supposed to be 10^{-8} M$_\odot$ yr^{-1}. However, although such outbursts would provide the mass increase necessary to trigger an enhanced thermonuclear burning shell on the white dwarf surface, the shape of their visual light-curves does not correspond well to observations. Therefore the hypothesis that the combination of dwarf nova and nova outbursts is an explanation of Z And symbiotic outbursts is not confirmed by model calculations of disc thermal-viscous instabilities. The fact that an increase in the mass supply to the disc is required to obtain the right energetics suggests that such an increase could be sufficient to trigger the outbursts of Z And, as proposed by Leibowitz & Formiggini (2008).

Use of the updated distance from *Gaia* supports this argument. With this new distance, the secondary has to be hotter than 3200 K for the quiescence magnitude to be around $V = 10.5$, assuming that the secondary still fills 57 per cent of its Roche lobe. The outburst amplitude is then reduced from 0.8 to 0.4 mag. If, on the other hand, we assume that the temperature is 2900 K as before, then the secondary must entirely fill its Roche lobe, and the outburst amplitude is about 0.6 mag. In both cases, the dwarf nova outbursts cannot explain the observed Z And outbursts, pointing towards other possibilities such as mass-transfer enhancement, as mentioned above.

5 CONCLUSIONS

We have studied the stability of accretion discs in symbiotic stars, which usually have long orbital periods, with particular emphasis on two systems, RS Oph and Z And. For the expected mass-transfer rates lower than 10^{-4} M$_\odot$yr^{-1}, their presumably large accretion discs (larger than 10^{12} cm) are prone to thermal-viscous instabilities and are thus expected to exhibit outbursts of the type observed in dwarf nova stars.

RS Oph

We have considered three models corresponding to three different mass-transfer rates, 10^{-6}, 10^{-7} and 10^{-8} M$_\odot$ yr^{-1}. None of these models reproduces the observed recurrence time and brightness amplitude of the recurrent nova outbursts. This rules out the possibility that these outbursts are in fact dwarf-nova-type outbursts, contrary to the suggestion by King & Pringle (2009), even in the case where their luminosity is increased as a result of steady hydrogen burning (Alexander et al. 2011). Note also that the peak accretion rate found by Alexander et al. (2011) exceeds the limit $\dot{M}_{\mathrm{RG}} = 3\dot{M}_{\mathrm{stable}}$ above which hydrogen can be burned as quickly as it is accreted; their outburst luminosity is therefore largely overestimated and TNRs are unavoidable.

We also considered the possibility that the disc instability outbursts can trigger a TNR on the white dwarf surface; as was proposed by S2006 in the case of Z And. For a mass-transfer rate of 10^{-6} M$_\odot$ yr^{-1}, we found that the mass of unburnt hydrogen accreted in a single outburst is sufficient to trigger a TNR, but the outbursts would then occur every 1.5 to 4 yr, instead of the observed 20 yr.

We found, however, that for mass-transfer rates of a few times $10^{-8} \, M_\odot \, \mathrm{yr}^{-1}$, the ignition mass can be accumulated on the white dwarf surface within roughly 20 yr. In this case, a series of dwarf nova outbursts can trigger the recurrent nova eruptions observed in RS Oph. This model might explain the pre-outburst luminosity increase observed in the light-curves of RS Oph outbursts (Adamakis et al. 2011) and explain the varying X-ray flux observed at different epochs of RS Oph quiescence. A recurrent-nova model not involving dwarf nova triggers requires a very small disc and does not explain the quiescent and pre-outburst observations. This suggests that RS Oph outbursts are recurrent 'combination nova events'.

Z And

We studied the possibility that, as suggested by S2006, some features of the complex Z And light-curve can be explained by dwarf nova outbursts. We found that for a mass-transfer rate of $10^{-6} \, M_\odot$ yr^{-1} the brightness amplitude of the disc instability outburst is close to 1 mag in the *V* band, which is very close to the amplitude of the 1997 outburst. However, the disc instability model totally fails to reproduce the observed shape of this outburst: the rise-time is far too long, and the outburst duration is too short. For lower mass-transfer rates, in addition to being the wrong shape, the outbursts are much fainter than observed.

Although we have shown that the 1997 feature was not caused by a dwarf nova outburst, we explored the possibility that the 2000-to-2002 outburst of Z And was, as suggested by S2006, a combination of a dwarf nova and nova outburst. We found that a single dwarf nova outburst can enhance nuclear burning on the white dwarf provided that the mass-transfer rates are close to $10^{-6} \, M_\odot \mathrm{yr}^{-1}$. Such steady high mass-transfer rates are most unlikely in this system. Reaching such a value requires a large (factor 10 at least) mass-transfer enhancement, which would in itself generate a significant brightening of the disc. Whether this enhancement leads to a disc instability or not is of little importance, and we therefore conclude that the initial component of the proposed 'combination nova' scenario is most likely the abrupt enhancement of the mass-transfer rate. Such an enhancement has been proposed by Bath & Pringle (1982) for explaining the outbursts of the symbiotic binary CI Cyg, and could be attributed for example to the magnetic activity at the surface of the companion, as suggested by Leibowitz & Formiggini (2008).

Dwarf nova outbursts may play a role in triggering RS Oph recurrent outbursts but are, most probably, of no importance in the case of Z And.

ACKNOWLEDGEMENTS

REFERENCES

Adamakis S., Eyres S. P. S., Sarkar A., Walsh R. W., 2011, MNRAS, 414, 2195

Alexander R. D., Wynn G. A., King A. R., Pringle J. E., 2011, MNRAS, 418, 2576

Anupama G. C., 2008, in Evans A., Bode M. F., O'Brien T. J., Darnley M. J., eds., ASP Conf. Ser. Vol. 401, RS Ophiuchi (2006) and the Recurrent Nova Phenomenon, Astron. Soc. Pac., San Francisco, p. 251

Anupama G. C., 2013, in Di Stefano R., Orio M., Moe M., eds, Proc. IAU Symp. Vol. 281, Binary Paths to Type Ia Supernovae Explosions, Kluwer, Dordrecht, p. 154

Bath G. T., Pringle J. E., 1982, MNRAS, 201, 345

Bode M. F., ed., 1987, RS Ophiuchi (1985) and the Recurrent Nova Phenomenon. VNU Science Press, Utrecht

Booth R. A., Mohamed S., Podsiadlowski P., 2016, MNRAS, 457, 822

Brandi E., Quiroga C., Mikołajewska J., Ferrer O. E., García L. G., 2009, A&A, 497, 815

Buat-Ménard V., Hameury J.-M., Lasota J.-P., 2001, A&A, 366, 612

Coriat M., Fender R. P., Dubus G., 2012, MNRAS, 424, 1991

Das R., Banerjee D. P. K., Ashok N. M., 2006, ApJ, 653, L141

Dubus G., 1998, PhD thesis. Univ. Paris VII Denis Diderot

Dubus G., Lasota J.-P., Hameury J.-M., Charles P., 1999, MNRAS, 303, 139

Dubus G., Hameury J.-M., Lasota J.-P., 2001, A&A, 373, 251

Duschl W. J., 1986a, A&A, 163, 56

Duschl W. J., 1986b, A&A, 163, 61

Evans A. et al., 2007, ApJ, 671, L157

Formiggini L., Leibowitz E. M., 1994, A&A, 292, 534

Frank J., King A., Raine D. J., 2002, Accretion Power in Astrophysics. 3rd edn, Cambridge Univ. Press , Cambridge

Gaia Collaboration, Brown A. G. A. Vallenari A., Prusti T., de Bruijne J. H. J., Babusiaux C., Bailer-Jones C. A. L., 2018, A&A, 616, A1

Hachisu I., Kato M., Luna G. J. M., 2007, ApJ, 659, L153

Hameury J.-M., Menou K., Dubus G., Lasota J.-P., Hure J.-M., 1998, MNRAS, 298, 1048

Hameury J.-M., Lasota J.-P., Dubus G., 1999, MNRAS, 303, 39

Hameury J.-M., Lasota J.-P., Warner B., 2000, A&A, 353, 244

Hameury J.-M., Viallet M., Lasota J.-P., 2009, A&A, 496, 413

Iijima T., 2008, in Evans A., Bode M. F., O'Brien T. J., Darnley M. J., eds., ASP Conf. Ser. Vol. 401, RS Ophiuchi (2006) and the Recurrent Nova Phenomenon. Astron. Soc. Pac., San Francisco, p. 115

Kenny H. T., 1995, PhD thesis. Univ. Calgary

Kenyon S. J., 1986, The Symbiotic Stars. Cambridge Univ. Press, Cambridge

King A. R., Pringle J. E., 2009, MNRAS, 397, L51

Lasota J.-P., 2001, New Astron. Rev., 45, 449

Lasota J.-P., Dubus G., Kruk K., 2008, A&A, 486, 523

Leibowitz E. M., Formiggini L., 2008, MNRAS, 385, 445

Lubow S. H., Shu F. H., 1975, ApJ, 198, 383

Menou K., Hameury J.-M., Lasota J.-P., Narayan R., 2000, MNRAS, 314, 498

Mikołajewska J., Shara M. M., 2017, ApJ, 847, 99

Mikolajewska J., Kolotilov E. A., Shenavrin V. I., Yudin B. F., 2002, in Gänsicke B. T., Beuermann K., Reinsch K., eds., ASP Conf. Ser. Vol. 261, The Physics of Cataclysmic Variables and Related Objects. Astron. Soc. Pac., San Francisco, p. 645

Monnier J. D. et al., 2006, ApJ, 647, L127

Mukai K., 2008, in Evans A., Bode M. F., O'Brien T. J., Darnley M. J., eds., ASP Conf. Ser. Vol. 401, RS Ophiuchi (2006) and the Recurrent Nova Phenomenon. Astron. Soc. Pac., San Francisco, p. 84

Mürset U., Schmid H. M., 1999, A&AS, 137, 473

Nelson T., Orio M., Cassinelli J. P., Still M., Leibowitz E., Mucciarelli P., 2008, ApJ, 673, 1067

Nelson T., Mukai K., Orio M., Luna G. J. M., Sokoloski J. L., 2011, ApJ, 737, 7

Orio M., 1993, A&A, 274, L41

Orio M., Covington J., Ögelman H., 2001, A&A, 373, 542

Rupen M. P., Mioduszewski A. J., Sokoloski J. L., 2008, ApJ, 688, 559

Schaefer B. E., 2009, ApJ, 697, 721

Schaefer B. E., 2010, ApJS, 187, 275

Schmid H. M., Schild H., 1997, A&A, 327, 219

Schreiber M. R., Hameury J.-M., Lasota J.-P., 2003, A&A, 410, 239

Skopal A., Shagatova N., 2012, A&A, 547, A45

Smak J., 1984, PASP, 96, 5

Smak J., 2008, AcA, 58, 55

Snijders M. A. J., 1987, Ap&SS, 130, 243

Sokoloski J. L., Bildsten L., 1999, ApJ, 517, 919

Sokoloski J. L., Luna G. J. M., Mukai K., Kenyon S. J., 2006a, Nature, 442, 276

Sokoloski J. L. et al., 2006b, ApJ, 636, 1002

Sokoloski J. L., Lawrence S., Crotts A. P. S., Mukai K., 2017, Proceedings of Accretion Processes in Cosmic Sources (APCS2016), 288, id. 21

Tetarenko B. E., Lasota J.-P., Heinke C. O., Dubus G., Sivakoff G. R., 2018a, Nature, 554, 69

Tetarenko B. E., Dubus G., Lasota J.-P., Heinke C. O., Sivakoff G. R., 2018b, MNRAS, 480, 2

Tuchman Y., Mineshige S., Wheeler J. C., 1990, ApJ, 359, 164

Urban J., Lyons K., Mittal R., Nadalin I., DiTuro P., Sion E., 2000, PASP, 112, 1611

van Paradijs J., McClintock J. E., 1995, X-ray Binaries, Cambridge Univ. Press, Cambridge, p. 58

Wolf W. M., Bildsten L., Brooks J., Paxton B., 2013, ApJ, 777, 136

Worters H. L., Eyres S. P. S., Bromage G. E., Osborne J. P., 2007, MNRAS, 379, 1557

Yaron O., Prialnik D., Shara M. M., Kovetz A., 2005, ApJ, 623, 398

APPENDIX A: CRITICAL VALUES OF EFFECTIVE TEMPERATURE, COLUMN DENSITY AND ACCRETION RATE

$$T_{\text{eff}}^{+} = 7122\, \alpha^{-0.002} m^{0.03} R_{10}^{-0.082}\ \text{K} \qquad \text{(A1)}$$

$$T_{\text{eff}}^{-} = 5665\, \alpha^{-0.005} m^{0.03} R_{10}^{-0.087}\ \text{K} \qquad \text{(A2)}$$

$$\Sigma^{+} = 7.983\, \alpha^{-0.784} m^{0.374} R_{10}^{1.122}\ \text{g cm}^{-2} \qquad \text{(A3)}$$

$$\Sigma^{-} = 12.16\, \alpha^{-0.835} m^{0.371} R_{10}^{1.113}\ \text{g cm}^{-2} \qquad \text{(A4)}$$

$$\dot{M}^{+} = 9.16 \times 10^{15}\, \alpha^{-0.008} m^{-0.88} R_{10}^{2.67}\ \text{g s}^{-1} \qquad \text{(A5)}$$

$$\dot{M}^{-} = 3.67 \times 10^{15}\, \alpha^{-0.02} m^{-0.88} R_{10}^{2.65}\ \text{g s}^{-1} \qquad \text{(A6)}$$

The '+' and '−' superscripts distinguish between the critical values for the upper and lower branch respectively. These fits are on average accurate to 1.5 per cent (T_{eff}^{+}), 3.5 per cent (T_{eff}^{-}), 6.9 per cent (Σ^{+}) and 10.3 per cent (Σ^{-}), for $10^{-2} < R_{10} < 100$ and $10^{-4} < \alpha < 1$ with maximum errors of 10, 12, 40 and 35 per cent respectively.

This paper has been typeset from a TEX/LATEX file prepared by the author.

Part III

Variability in Neutron stars: Oscillations of levitating shells

Chapter 3

Paper II: Radial modes of levitating atmospheres around Eddington luminosity neutron stars

Radial modes of levitating atmospheres around Eddington luminosity neutron stars

D. A. Bollimpalli[1,2]★ and W. Kluźniak[1,2]

[1]*Nicolaus Copernicus Astronomical Center, ul. Bartycka 18, PL-00-716 Warsaw, Poland*
[2]*KITP, University of California, Santa Barbara, CA 93106, USA*

ABSTRACT

We consider an optically thin radiation-supported levitating atmosphere suspended well above the stellar surface, as discussed recently in the Schwarzschild metric for a star of luminosity close to the Eddington value. Assuming the atmosphere to be geometrically thin and polytropic, we investigate the eigenmodes and calculate the frequencies of the oscillations of the atmosphere in Newtonian formalism. The ratio of the two lowest eigenfrequencies is $\sqrt{\gamma + 1}$, i.e. it only depends on the adiabatic index.

Key words: gravitation – stars: atmospheres – stars: neutron – stars: oscillations.

1 INTRODUCTION

Recent observations have mapped the existence of neutron stars with highly super-Eddington luminosities in ultraluminous X-ray source (ULX) systems NGC 7793 P13, NGC 5907, NuSTAR J09551+6940.8 (Bachetti et al. 2014; Israel et al. 2017a,b). It has long been known that neutron stars in X-ray binaries, A0538-66, SMC X-1 and GRO J1744−28, are unusually luminous (Coe et al. 1981; Skinner et al. 1982; Sazonov, Sunyaev & Lund 1997). Also, studies of X-ray bursts report that, during very energetic Type I X-ray bursts, the X-ray luminosity is close to the Eddington limit (Lewin, van Paradijs & van den Heuvel 1997). For neutron stars with such high luminosities, it is possible that close to the star's surface, radiative forces become dominant over gravity. Under such conditions a 'levitating atmosphere' may be formed, the properties of which were derived in the spherically symmetric case by Wielgus et al. (2015, 2016), and had previously been discussed for the approximately plane-parallel case in the context of near Eddington luminosity accretion discs by Fukue (1996), who termed them 'photon floaters'. An additional argument of the observational relevance for these levitating atmospheres has been afforded in a new study, in which they have been shown to affect the propagation of light rays from the central source, thereby affecting the observed appearance of the central object (Rogers 2017).

X-ray bursters exhibit high-frequency (300–600 Hz) 'burst oscillations' (Strohmayer 2001), which may be related to the Eddington luminosity of the sources. In bright X-ray bursts, neutron star often reaches near Eddington-limit luminosities during which the dominant radiation pressure drives the photospheric layers off the neutron star; this phenomenon is termed as photospheric radius expansion (PRE). Oscillations in the case of PRE bursts are observed during

the rise and decay phase of the burst (Muno et al. 2002). However, bursts without PRE also show evidence for oscillations (van Straaten et al. 2001). During the decay phase of the burst, frequency is observed to increase with time (Strohmayer & Bildsten 2006). While the source of these oscillations is still open for debate, here we try to understand if the radial oscillations of the levitating atmospheres could be relevant to such phenomena.

In this paper, we consider a radial perturbation of a spherically symmetric, optically thin levitating atmosphere. The goal is to analytically investigate the eigenmodes of the oscillations of the atmosphere. Abarca & Kluźniak (2016) have found the fundamental radial mode of oscillations of an optically thin levitating atmosphere. They have shown that including the radiation drag stabilizes the atmosphere against the radial perturbations that could excite the fundamental radial mode. Here, we would like to investigate all possible modes of radial oscillations for this given system. Assuming the atmosphere to be geometrically thin, we neglect the relativistic corrections and perform linear perturbation analysis in the Newtonian approximation. We then determine all the possible radial eigenmode solutions of the system. Our calculations are performed by perturbing the levitating atmospheres of Wielgus et al. (2015), which have the form of spherical shells, but the calculations should be equally valid for the plane-parallel case of the photon floaters of Fukue (1996), and have some application as well to the eigenmodes of other accretion structures with a reflection symmetry, such as the slender tori of Blaes, Arras & Fragile (2006).

Optically thin levitating atmospheres are especially likely to survive in the pulsating ULXs, which can be understood as slowly rotating neutron stars, a special case of extremely luminous X-ray pulsars (Bachetti et al. 2014), in which the super-Eddington accretion flow near the poles is confined by the strong stellar magnetic field (Basko & Sunyaev 1976; Mushtukov et al. 2017).

A study of optically thick atmospheres would have been more directly relevant to X-ray burst oscillations, however we are

★ E-mail: deepika@camk.edu.pl

hampered at present by the lack of a suitable analytic solution for the background equilibrium solution. The optically thick super-Eddington atmosphere solution (Wielgus et al. 2016) requires a proper treatment of the radiative transfer that has only been achieved numerically.

2 LEVITATING ATMOSPHERES

Abramowicz, Ellis & Lanza (1990) have studied the fully general relativistic radial motion of test particles in combined gravitational and radiation fields around a spherical, compact star radiating isotropically. They have shown that under these circumstances, a spherical shell of matter may form around the neutron star whose location varies with luminosity from the surface of the star to infinity. This surface is defined by the radius where the gravitational forces balance the radiative forces due to stellar luminosity. Unlike in the Newtonian theory, where both the gravity and radiative flux fall off as $1/r^2$, in general relativity, the radiative flux has a stronger radial dependence than the gravitational acceleration. Therefore, radiative forces may dominate over gravitational pull close to the surface of the compact star, while the gravitational forces take over at larger radii. A similar situation may obtain above nearly Eddington luminosity accretion disc, as discussed in several papers (Fukue 1996; Kitabatake & Fukue 2003; Itanishi & Fukue 2017).

For a star radiating at super-Eddington luminosities, gravitational forces will balance the radiation forces on a sphere at a particular radius from the star. It has been referred to as the 'Eddington capture sphere' (ECS; Stahl et al. 2012). A test particle moving with a reasonable velocity would bind to this sphere without falling on to the stellar surface also if initially in non-radial motion as the Poynting–Robertson radiation drag removes the angular momentum of the particle reducing it to zero (Bini, Jantzen & Stella 2009; Oh, Kim & Lee 2010; Stahl et al. 2013). The captured particles levitate above the stellar surface, as every point on ECS corresponds to an equilibrium state that is stable in radial direction (Abramowicz et al. 1990) and neutral in directions tangent to the sphere (Stahl et al. 2012). These properties of ECS result in an atmosphere in hydrostatic equilibrium, which is detached from the star and levitating above its surface (Wielgus 2016). In the case of an optically thin atmosphere, analytical solutions show that both the pressure and density fall steeply on either side of the ECS, while the peak value is attained at the ECS (Wielgus et al. 2015). The term 'levitation' was first introduced by Inogamov & Sunyaev (1999) in the context of the luminous equatorial accretion belt (boundary layer) formed at the interface of the neutron star surface and the accretion disc; the effective gravity in the boundary layer is further reduced by the rapid azimuthal motion of the fluid, so the balance considered by these authors was between gravity and three forces: pressure gradient, centrifugal and radiation forces. Our simplified treatment neglects rotation.

3 HYDROSTATIC EQUILIBRIUM CONFIGURATION

In the Schwarzschild metric around a neutron star of mass M, a local observer at a certain radius r measures the redshifted luminosity of the star $L(r)$ as

$$L(r) = L_\infty \left(1 - \frac{2r_g}{r} \right)^{-1}, \tag{1}$$

where L_∞ is the luminosity of the star measured at infinity and $r_g = GM/c^2$ is the gravitational radius. For a compact star of

radius R_* and luminosity L_*, we have $L_\infty = L_* \left(1 - \frac{2r_g}{R_*} \right)$. For convenience, we shall use the following parametrized luminosity throughout our calculations:

$$\lambda = L_\infty/L_{\mathrm{Edd}}, \tag{2}$$

where L_{Edd} is the Eddington luminosity.

We now consider a static atmosphere levitating above the surface of the neutron star radiating at super-Eddington luminosities. The equation of hydrostatic equilibrium for an optically thin atmosphere under relativistic formalism has been derived previously (Wielgus et al. 2015):

$$\frac{1}{\rho} \frac{\mathrm{d}p}{\mathrm{d}r} = -\frac{GM}{r^2 \left(1 - r_g/r \right)} \left[1 - \lambda \left(1 - \frac{2r_g}{r} \right)^{-1/2} \right]. \tag{3}$$

The first term on the right-hand side comes from the gravitational force, while the second term is related to the radiation force in an optically thin fluid. In deriving the above equation (3), it has been assumed that the atmospheric temperatures are non-relativistic, i.e. of the order of few keV. At such temperatures, one can neglect the internal energy and pressure of the fluid in comparison to the rest-mass energy density.

From the above equation, it follows that the gravitational force and the force due to radiation balance each other at radius

$$R_{\mathrm{ECS}} \equiv \frac{2r_g}{(1 - \lambda^2)}, \tag{4}$$

and the pressure gradient at this radius becomes zero, corresponding to the maximum pressure at R_{ECS}.

We consider barotropic fluid, $p = p(\rho)$, and in this case we assume it to be a polytrope. Therefore

$$p = K\rho^{1+1/n}, \tag{5}$$

where K is the polytropic constant and n is the polytropic index.

We may cast equation (3) in terms of an effective potential $\Phi(r)$, in such a way that upon its integration using equation (5), it results in the Bernoulli equation,

$$(n+1)\frac{p}{\rho} + \Phi(r) = \mathrm{const.} \tag{6}$$

We may evaluate this constant on the equilibrium surface, $r_0 \equiv R_{\mathrm{ECS}}$, to get

$$(n+1)\frac{p}{\rho} + \Phi(r) = (n+1)\frac{p_0}{\rho_0} + \Phi(r_0), \tag{7}$$

where subscript zero denotes the quantities evaluated at the ECS, $r = r_0$. Following simple algebraic steps, one could write

$$\frac{p}{\rho} = \frac{p_0}{\rho_0} f, \tag{8}$$

where we define the function $f(r)$ as

$$f(r) = 1 - \frac{1}{nc_{\mathrm{s},0}^2} \left[\Phi(r) - \Phi(r_0) \right], \tag{9}$$

and $c_{\mathrm{s}}^2 = (n+1)p/(n\rho)$ is the square of the sound speed.

We now evaluate this function f in the vicinity of r_0 by the second-order Taylor expansion of the effective potential, which is valid for thin atmospheres. We have

$$\Phi(r) - \Phi(r_0) = \frac{(1-\lambda^2)^4 c^2}{32\lambda^4} \frac{r_0^2}{r_g^2} x^2, \tag{10}$$
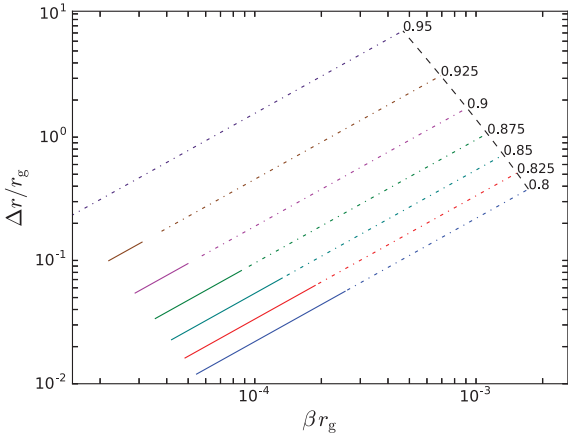
Figure 1. Atmosphere thickness, Δr, dependence on β and λ parameters. Both the axes are logarithmically scaled. Set of solid and dash–dot lines labelled with values of λ, represent the linear relation between thickness of the atmosphere and β. The solid lines mark the regime where the second-order approximation holds good. The dashed line is plotted for a particular temperature value 10^8 K that shows that atmosphere gets thinner as λ decreases. We considered $\mu = 1/2$ for this plot.

where we have introduced a new coordinate $x = (r - r_0)/r_0$, centred at r_0. This will immediately give us

$$f = 1 - \frac{x^2}{\beta^2}\omega_{r,0}^2, \tag{11}$$

where we define $\beta^2 = 2n c_{s,0}^2/r_0^2$ and

$$\omega_{r,0}^2 = \frac{(1-\lambda^2)^4}{16\lambda^4}\frac{c^2}{r_g^2} \tag{12}$$

for our convenience. We shall later show that $\omega_{r,0}$ is indeed the frequency of the fundamental mode. The boundaries of the atmosphere are defined at $f = 0$ as both the pressure and density vanish at this point. Following this, the thickness of the atmosphere would be

$$\Delta r = 2\beta r_0/\omega_{r,0} = 4\sqrt{2n}\left(\frac{c_{s,0}}{c}\right)\left(\frac{\lambda^2}{1-\lambda^2}\right). \tag{13}$$

In Fig. 1, we explore the dependence of the atmosphere thickness, Δr on β and λ. Each solid and dash–dot line, representing a particular value of λ, shows that Δr increases with β. Specifically, solid lines represent the regime where the second-order approximation may hold good, i.e. $x \ll 1$ (we simply chose $x = 0.005$ for the plot). Therefore, for a star with a given luminosity, λ remains constant, and the extent to which the atmosphere extends is determined by β and in the slender limit $\beta \to 0$.

As β implicitly depends on temperature at r_0, in Fig. 1 we considered the temperature range within $[10^5, 10^8]$ K and we take the mean molecular weight of the fluid, μ, to be $1/2$. The dashed line in Fig. 1 is plotted to give a glimpse of how Δr varies with λ. As shown in the figure, the slenderness of the atmosphere increases as λ decreases. Here the dashed line is plotted for the temperature value, 10^8 K, but the trend would remain the same for other values of temperature.

Based on equation (8) and the equation of state, equation (5), it is convenient to scale the pressure and density in equilibrium as follows:

$$p = p_0 f^{n+1},$$
$$\rho = \rho_0 f^n, \tag{14}$$

which clearly ensures that the pressure and density drop to zero at the boundaries while retaining their maximum value at the centre. The density gradient is always in the direction of the effective gravity (taking into account radiation forces as well), and so is Rayleigh–Taylor stable.

In passing, we note an interesting property of the numerical solution for the optically thick atmosphere, which may make our analysis an interesting limiting case of future (perhaps numerical) calculations of the oscillations of the optically thick levitating atmosphere. The optically thin edges of the optically thick atmosphere coincide with this analytically derived optically thin solution, while the radial density has a universal profile (independent of the mass of the atmospheric shell) in the optically thick regions, satisfying over the bulk of the shell the condition of density decreasing with radial distance from the source, i.e. increasing in the direction of the effective force of gravity (Wielgus 2016).

4 ELEMENTARY DISCUSSION OF RADIAL OSCILLATIONS

To develop intuitions relevant to fluid motion in a gravitational field of magnitude increasing with height we present an elementary discussion in a Newtonian formalism of the lowest frequency radial modes of a thin levitating atmosphere in the plane-parallel approximation.

Choose the z-axis in the vertical direction, pointing either towards or away from the neutron star, and consider a fluid atmosphere in a gravitational field directed towards the $z = 0$ plane: $\mathbf{g}(z) = -\hat{z}g(z)$, with $g(z) = \omega_\perp^2 z$. In hydrostatic equilibrium, the surface of maximum pressure coincides with the $z = 0$ plane, and the atmosphere is symmetric with respect to reflection in that plane.

Let us consider the lowest frequency modes of the atmosphere, one with a symmetric displacement function, $z \mapsto z + \xi(z, t)$, with $\xi(-z, t) = \xi(z, t)$, and no nodes (the 'fundamental'), and one with antisymmetric displacements, $\xi(-z, t) = -\xi(z, t)$, and one node (the 'first overtone'). As we will see, the fundamental mode corresponds to rigid motion, with the plane of non-varying maximum pressure moving harmonically up and down with respect to the $z = 0$ plane. The first overtone is a breathing-like motion characterized by reflection symmetry in the $z = 0$ plane. In general, as the atmosphere oscillates, its pressure is a function of position and time $p(z, t)$.

To derive the eigenfrequencies, consider – without any loss of generality – the part of the atmosphere that is initially above the horizontal plane at $z = z_0 > 0$ plane. For a polytropic atmosphere the density goes to zero at the upper boundary initially at, say, $z = H > 0$ (and another one at $z = -H$). Thus, we are focusing on atmospheric slab of matter confined by the upper boundary (plane) at $H + \xi(H, t)$ and an imagined lower boundary at $z_0 + \xi(z_0, t)$. The conserved mass per unit area in this slab is

$$m = \int dm = \int_{z_0}^{H} \rho(z)\, dz. \tag{15}$$

The slab suffers two external forces, a body force owing to gravity, and a surface force at the lower boundary at $z_0 + \xi$. The latter force per unit area is just the pressure $p = p_0 + \Delta p(t)$, with p_0 the equilibrium pressure at $z = z_0$, and Δp the Lagrangian change in pressure: $\Delta p(t) = p(z_0 + \xi_0, t) - p_0$, with $\xi_0 \equiv \xi(z_0, t)$. The body force is just the weight of the slab per unit area,

$$w(t) = \int g\, dm = \int_{z_0}^{H} g(z + \xi)\rho(z)\, dz. \tag{16}$$

We can now specify to the case at hand, $w_0 = m\omega_\perp^2 z_{CM}$ with $z_{CM} = (\int z \, dm)/m$,

$$w(t) = w_0 + \omega_\perp^2 \int_{z_0}^{H} \xi(z, t)\rho(z) \, dz. \tag{17}$$

The equation of motion for the displacement of the centre of mass, $\xi_{CM}(t) \equiv \xi(z_{CM}, t)$, is

$$m\partial^2\xi_{CM}/\partial t^2 = p - w. \tag{18}$$

For a uniform displacement, $\xi(z, t) = \xi_{CM}(t)$, i.e. for a rigid motion, there are no nodes, and we obtain the 'fundamental' frequency $\omega_1 = \omega_\perp$ from the simple harmonic equation $\partial^2\xi_{CM}/\partial t^2 = -\omega_\perp^2\xi_{CM}$, following from $\partial\xi/\partial z = 0$ that implies $p = p_0 = w_0$, with $p - w = -m\omega_\perp^2\xi_{CM}$ by equations (15) and (17).

For the breathing mode, with the (easy to derive) ansatz $\xi = z\xi_{CM}/z_{CM}$, we have $\Delta p = -\gamma p_0 \xi_{CM}/z_{CM} = -\gamma m\omega_\perp^2\xi_{CM}$, and $w(t) = w_0 + m\omega_\perp^2\xi_{CM}(t)$. Thus

$$\partial^2\xi_{CM}/\partial t^2 + (\gamma + 1)\omega_\perp^2\xi_{CM} = 0,$$

and the eigenfrequency of the breathing mode is $\omega_2 = \sqrt{1 + \gamma}\,\omega_1$. The same ratio of $\sqrt{1 + \gamma}$ can be obtained for the breathing and vertical mode eigenfrequencies of a slender torus orbiting a black hole (Blaes et al. 2006), if the Newtonian limit is taken (in which the epicyclic frequencies are equal to one another, $\omega_r = \omega_\perp$). In general, just like the fundamental mode just considered, the vertical mode of the slender torus corresponds to rigid motion at the vertical epicyclic frequency, $\omega_1 = \omega_\perp$ (Kluźniak 2005), and the breathing mode of the levitating atmosphere is a direct analogue of the breathing mode of a slender torus.

5 RADIAL OSCILLATIONS IN NEWTONIAN FRAMEWORK

We subject the static atmosphere to small radial perturbations of the form $\delta X(r, t) = \delta X_*(r)\,e^{i\omega t}$, where ω is the frequency with which perturbations propagate. Because of these small radial perturbations, fluid attains certain radial velocity given by δv_r. We then perform the linear perturbation analysis and derive the wave equation that governs the propagation of these perturbations. To do so, we assume that atmosphere is geometrically thin, i.e. $x \ll 1$. Relativistic corrections to energy density are negligible on such small scales to which these atmospheres extend. Therefore, Newtonian theory would suffice to evaluate ω. In this work, we ignore the radiation drag, but note that equation (3) is valid in any case as the equilibrium atmosphere is static and the initial velocities being zero do not contribute to the pressure balance.

We start with the equations of motion for a radially moving fluid in Newtonian framework. Linearized Euler and continuity equations are given as

$$\frac{\partial}{\partial t}\delta v_r + \frac{\partial}{\partial r}\left(\frac{\delta p}{\rho}\right) = 0, \tag{19}$$

$$\frac{\partial}{\partial t}(\delta\rho) + \frac{1}{r^2}\frac{\partial}{\partial r}\left(r^2\rho\delta v_r\right) = 0. \tag{20}$$

We define a scalar potential $W = \delta p/(\omega\rho)$, which identifies with the fluid enthalpy, and simplifies our problem to great extent (Papaloizou & Pringle 1984). Considering the time derivative of the perturbation quantities would give us the following relations:

$$\delta v_r = i\frac{\partial W}{\partial r}, \tag{21}$$

$$\omega^2 W = ic_s^2\left(\frac{\partial}{\partial r}\delta v_r + \frac{\delta v_r}{\rho}\frac{\partial\rho}{\partial r} + \frac{2\delta v_r}{r}\right). \tag{22}$$

Combining both of these equations, equations (21) and (22) and using equation (14), we obtain a second-order differential equation in W,

$$\frac{\partial^2 W}{\partial r^2} + \left(\frac{n}{f}\frac{\partial f}{\partial r} + \frac{2}{r}\right)\frac{\partial W}{\partial r} + \frac{\omega^2}{c_s^2}W = 0. \tag{23}$$

In general it is difficult to solve the above equation analytically but in the slender limit ($\beta \to 0$) this equation simplifies to

$$(1 - \eta^2)\frac{\partial^2 W}{\partial\eta^2} - 2n\eta\frac{\partial W}{\partial\eta} + 2n\sigma^2 W = 0, \tag{24}$$

where we have made use of the notations $\eta = x\omega_{r,0}/\beta$, with $f = 1 - \eta^2$, and $\sigma = \omega/\omega_{r,0}$. The eigenvalue problem given by equation (24) has to be solved with appropriate boundary conditions. In this case, it is required that pressure and density vanish at the boundaries. Since we consider small, linear perturbations, this condition translates to vanishing of the Lagrangian perturbation in pressure at the boundaries in the form

$$(\Delta p)_{f=0} = \left(\delta p + \xi\frac{\partial p}{\partial r}\right)_{f=0} = 0, \tag{25}$$

where ξ is the Lagrangian displacement. After rewriting the Lagrangian displacements in terms of W, the surface boundary condition becomes

$$\left[\rho_0 f^n \omega_{r,0}\left(W\sigma - \frac{\eta}{\sigma}\frac{\partial W}{\partial\eta}\right)\right]_{f=0} = 0. \tag{26}$$

The requirement that W and its first derivative be finite at $f = 0$ is a sufficient condition for this boundary condition to hold. It is also possible that the singular eigenfunctions may appear on the surface boundaries. But such solutions must be rejected as they are not compatible with equation (24). Therefore, the eigenfunctions are simply given by the Gegenbauer polynomials $C_\nu^\mu(\eta)$ with order $\mu = n - 1/2$ and degree $\nu = 0, 1, 2, 3\ldots$, where $\nu(\nu + 2n - 1) = 2n\sigma^2$ (Abramowitz & Stegun 1972). Hence,

$$\omega_\nu = \sqrt{\frac{\nu(\nu + 2n - 1)}{2n}}\,\omega_{r,0}, \tag{27}$$

with $\omega_{r,0}^2 = (1 - \lambda^2)^4 c^6/(16G^2 M^2\lambda^4)$ by equation (12).

6 RESULTS AND DISCUSSIONS

When the atmospheric fluid element in equilibrium is radially displaced, the restoring forces due the gravity and pressure variation act upon the fluid trying to restore it back to equilibrium. But owing to inertia, the displacement overshoots and thus the atmosphere is set into harmonic oscillations. Table 1 summarizes the eigenfunctions and eigenfrequencies of the first few eigenmodes of this system. Degree $\nu = 0$ corresponds to a trivial solution with eigenfunction 1, i.e. vanishing displacement by equation (21).

The lowest order mode, $\nu = 1$, is the fundamental mode given by the frequency $\omega_f \equiv \omega_1 = \omega_{r,0}$. In this mode the fluid oscillates around the ECS radially back and forth while maintaining the Lagrangian pressure profile in the atmosphere constant. Thus it is an incompressible mode. The displaced fluid is set into oscillations by the restoring force due to gravity.

For the next lowest order mode, $\nu = 2$, pressure restoring forces become important. We term this as the breathing mode since the

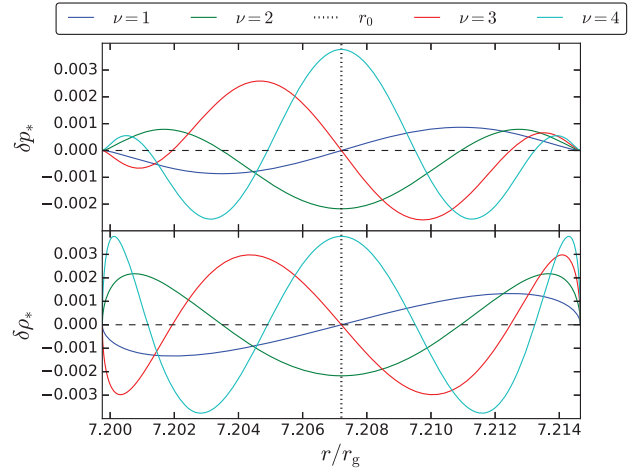**Table 1.** Eigenmodes and eigenfunctions of lowest order modes.

ν	Eigenfrequency squared, σ^2	Eigenfunction, W
0	0	1
1	1	$(2n-1)\eta$
2	$(2n+1)/n$	$\left(n - \frac{1}{2}\right)[\eta^2(2n+1) - 1]$
3	$3(n+1)/n$	$\frac{\eta}{6}(4n^2 - 1)[(2n+3)\eta^2 - 3]$
4	$2(2n+3)/n$	$\frac{1}{24}(4n^2 - 1)[(2n+3)\eta^2((2n+5)\eta^2 - 6) + 3]$
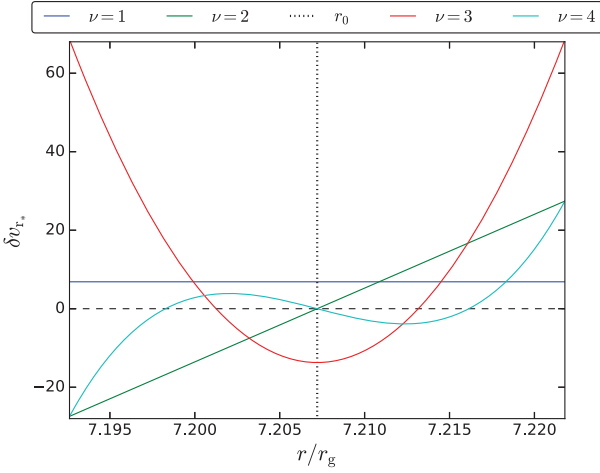
Figure 2. Radial profiles of velocity perturbations for the lowest order modes. We take $n = 3/2$ and $\lambda = 0.85$. Horizontal dashed line is plotted to trace the nodes where the radial velocity goes to zero, $\delta v_r = 0$, while the vertical dotted line marks the location of the ECS.

Figure 3. Top panel shows the pressure eigenmode profile for lowest order modes ($\nu = 1, 2, 3$ and 4) calculated for $n = 3/2$ and $\lambda = 0.85$. Bottom panel shows the perturbed density variations for the same. Horizontal dashed line is where the perturbations vanish, while the vertical dotted line marks the location of the ECS.

atmosphere expands and contracts symmetrically with respect to the ECS, with a frequency $\omega_b \equiv \omega_2 = \sqrt{(2n+1)/n}\,\omega_{r,0}$.

In Fig. 2, we plot the radial profiles of the velocity perturbation. We consider $n = 3/2$ and $\lambda = 0.85$. We can scale the perturbation by an arbitrary value so that assumptions made to pursue linear perturbation analysis hold well. The domain of the plot corresponds to the extent of the equilibrium atmosphere. The vertical dotted line marks the location of the ECS, which for the given parameters is $\approx 7.207 r_g$. The horizontal dashed line is plotted to identify the nodes at which velocity perturbations vanish. The fluid in the fundamental mode oscillates with uniform velocity depicted by the horizontal blue line. This means that at a given time, all the fluid particles in the atmosphere are moving with same speed in same direction. As the system evolves in this mode, the fluid oscillates back and forth through the horizontal dashed line. Velocity perturbation for the breathing mode holds a linear relation with radius as shown by the green line with a node at the ECS. While expanding and contracting, fluid in the atmosphere either recedes away from the ECS or approaches ECS, while the centre stays still marking a node at the ECS. As the system evolves, the green curve pivots around its node at the ECS. As we move further to the higher modes, the number of nodes simply increases.

In Fig. 3, the top and bottom panels show the radial profiles of the Eulerian perturbation in pressure and density, respectively. The parameters considered here are same as before. The vertical dotted line carries the same meaning as discussed for the previous figure. The horizontal dashed line is plotted to identify the nodes at which the perturbations in density and pressure vanish. Note that the pressure and density perturbations vanish at the boundaries too as required by the boundary condition, but they are not to be counted as nodes. The fundamental mode plotted by the dark blue curve is an incompressible mode. But to see this from an Eulerian perturbation plot, we need the information of velocity perturbations. Since the velocity perturbation in the fundamental mode is uniform (see Fig. 3), its divergence vanishes. This implies from the continuity equation that density or the pressure in a given volume remains the same. For the breathing mode, the pressure drop at the centre is accompanied by an increase in pressure close to the boundaries as shown by the green curve with two nodes in the plot. Since we considered a polytropic fluid, the density perturbation profiles look analogous to the pressure perturbation profiles. Note that the number of nodes in pressure perturbations profile is one greater than the number of nodes in the velocity perturbations for a given mode.

From Table 1, the frequency of oscillations in the fundamental mode is simply $\omega_{r,0}$. This is independent of n because the fundamental mode oscillations are caused purely by gravity. Remaining modes have the contribution from the fluid's pressure. The exact analytical expressions for eigenfrequencies allows us to calculate the ratio of the frequencies of the breathing mode, ω_b, to the fundamental mode, ω_f,

$$\frac{\omega_b}{\omega_f} = \sqrt{2 + \frac{1}{n}} = \sqrt{1 + \gamma}. \tag{28}$$

For $n = 3/2$, this ratio is $\sqrt{8/3} \approx 1.633$. Interestingly, the ratio of frequencies of any two modes is independent of λ, the stellar luminosity.

For a neutron star with mass $1.4\,M_\odot$ and $\lambda = 0.8$, we calculate the Newtonian frequency of oscillations for the $\nu = 1$ fundamental mode to be $1.171\,\text{kHz}$. Our result matches with the fundamental mode oscillation frequency earlier derived for full general relativistic equations (Abarca & Kluźniak 2016), if we consider the

following relativistic effects. First, the invariant line element differs from coordinate displacement dr, inducing a correction factor, $1/\sqrt{g_{rr}} \approx \lambda$. Secondly, in general relativity, proper time and coordinate time are different and the frequency measured by an observer at infinity would be redshifted by a factor $\sqrt{g_{tt}} \approx \lambda$. Owing to these two factors, if we multiply the Newtonian frequency by λ^2 we get the relativistic frequency $\tilde{\omega} = (1 - \lambda^2)^2 c/4r_g$. For the above considered parameters, the relativistic frequency for the fundamental mode is then ≈ 750 Hz, for $\lambda = 0.8$, which is the same as obtained in Abarca & Kluźniak (2016). For $0.8 < \lambda$ the fundamental frequency decreases in value with increasing luminosity, but similarly accounting for the relativistic corrections, the eigenfrequencies of the higher modes for $0.8 < \lambda < 0.98$ may fall in the observed range of 300–600 Hz for X-ray burst quasi-periodic oscillations (QPOs). Abarca & Kluźniak (2016) have also shown that for optically thin solutions, radiation drag can efficiently damp the fundamental mode oscillation. Here we find that the higher modes have larger frequencies than the damping rate found by those authors, so it is likely that the oscillations of the higher modes can be underdamped. We leave this for our future work, where we plan to study the full general relativistic motion of particles including radiation drag.

Also, note that $\omega_{r,0}$ increases with decreasing luminosity.[1] So for any given mode, assuming that the polytropic index of the atmosphere remains the same, frequency of any of the eigenmodes would increase with time if the luminosity of the source decreases with time. This is similar to what is usually observed in the decay phase of the X-ray bursts (Strohmayer 2001; Strohmayer & Bildsten 2006).

7 CONCLUSIONS

In this paper, we provide a complete Newtonian analytic solution for the radial oscillation eigenmodes of a thin levitating atmospheric shell centred at the ECS around a luminous non-rotating stellar source. We derive the complete set of eigenfunctions for the modes, and the eigenfrequencies for all the mode oscillations[2] are given by an exact analytical expression, equation (27). We provide the ratio of the frequencies of breathing mode to the fundamental mode, $\sqrt{1+\gamma}$, which entirely depends on the polytropic index of the atmosphere. For $\gamma = 5/3$, we find this ratio to be $\sqrt{8/3} \approx 1.633$, and for $\gamma = 4/3$ it is $\sqrt{7/3} \approx 1.53$.

ACKNOWLEDGEMENTS

REFERENCES

Abarca D., Kluźniak W., 2016, MNRAS, 461, 3233
Abramowicz M. A., Ellis G. F. R., Lanza A., 1990, ApJ, 361, 470

Abramowitz M., Stegun I. A., 1972, Handbook of Mathematical Functions. Dover Press, New York
Bachetti M. et al., 2014, Nature, 514, 202
Basko M. M., Sunyaev R. A., 1976, MNRAS, 175, 395
Bini D., Jantzen R. T., Stella L., 2009, Classical Quantum Gravity, 26, 055009
Blaes O. M., Arras P., Fragile P. C., 2006, MNRAS, 369, 1235
Coe M. J., Burnell S. J. B., Engel A. R., Evans A. J., Quenby J. J., 1981, MNRAS, 197, 247
Fukue J., 1996, PASJ, 48, 89
Inogamov N. A., Sunyaev R. A., 1999, Astron. Lett., 25, 269
Israel G. L. et al., 2017a, Science, 355, 817
Israel G. L. et al., 2017b, MNRAS, 466, L48
Itanishi Y., Fukue J., 2017, PASJ, 69, 56
Kitabatake E., Fukue J., 2003, PASJ, 55, 1115
Kluźniak W., 2005, Astron. Nachr., 326, 820
Kluźniak W., 2013, A&A, 551, A70
Lewin W. H. G., van Paradijs J., van den Heuvel E. P. J. eds, 1997, Cambridge Astrophys. Ser. Vol. 26, X-ray Binaries. Cambridge Univ. Press, Cambridge
Mishra B., Kluźniak W., 2014, A&A, 566, A62
Muno M. P., Chakrabarty D., Galloway D. K., Psaltis D., 2002, ApJ, 580, 1048
Mushtukov A. A., Suleimanov V. F., Tsygankov S. S., Ingram A., 2017, MNRAS, 467, 1202
Oh J. S., Kim H., Lee H. M., 2010, Phys. Rev. D, 81, 084005
Papaloizou J. C. B., Pringle J. E., 1984, MNRAS, 208, 721
Rogers A., 2017, Universe, 3, 3
Sazonov S. Y., Sunyaev R. A., Lund N., 1997, in Meyer-Hofmeister E., Spruit H., eds, Lecture Notes in Physics, Vol. 487, Accretion Disks – New Aspects. Springer-Verlag, Berlin, p. 199
Skinner G. K., Bedford D. K., Elsner R. F., Leahy D., Weisskopf M. C., Grindlay J., 1982, Nature, 297, 568
Stahl A., Wielgus M., Abramowicz M., Kluźniak W., Yu W., 2012, A&A, 546, A54
Stahl A., Kluźniak W., Wielgus M., Abramowicz M., 2013, A&A, 555, A114
Strohmayer T. E., 2001, in White N. E., Malaguti G., Palumbo G. G. C., eds, AIP Conf. Proc. Vol. 599, X-ray Astronomy: Stellar Endpoints, AGN, and the Diffuse X-ray Background. Am. Inst. Phys., Melville, NY, p. 377
Strohmayer T., Bildsten L., 2006, in Lewin W. H. G., van der Klis M., eds, Compact Stellar X-ray Sources. Cambridge Univ. Press, Cambridge, p. 113
van Straaten S., van der Klis M., Kuulkers E., Méndez M., 2001, ApJ, 551, 907
Wielgus M., 2016, in Meiron Y., Li S., Liu F.-K., Spurzem R., eds, Proc. IAU Symp. Vol. 312, Star Clusters and Black Holes in Galaxies across Cosmic Time. Cambridge Univ. Press, Cambridge, p. 131
Wielgus M., Stahl A., Abramowicz M., Kluźniak W., 2012, A&A, 545, A123
Wielgus M., Kluźniak W., Sądowski A., Narayan R., Abramowicz M., 2015, MNRAS, 454, 3766
Wielgus M., Sądowski A., Kluźniak W., Abramowicz M., Narayan R., 2016, MNRAS, 458, 3420

---

[1] For an impulsive change in luminosity the optically thin atmosphere may be ejected (Kluźniak 2013; Mishra & Kluźniak 2014).

[2] The atmospheric oscillations described here are very different from the oscillations of the ECS described in Wielgus et al. (2012), which are due to accretion feedback and stellar luminosity variability.

This paper has been typeset from a TEX/LATEX file prepared by the author.

Chapter 4

Paper III: Atmospheric oscillations provide simultaneous measurement of neutron star mass and radius

Atmospheric oscillations provide simultaneous measurement of neutron star mass and radius

D. A. Bollimpalli [1,2]★ M. Wielgus,[1,2,3] D. Abarca[1] and W. Kluźniak[1,2]

[1]*Nicolaus Copernicus Astronomical Center, ul. Bartycka 18, PL 00-716 Warsaw, Poland*
[2]*Kavli Institute for Theoretical Physics, University of California, Santa Barbara, CA 93106, USA*
[3]*Black Hole Initiative, Harvard University, 20 Garden Str, Cambridge, MA 02138, USA*

ABSTRACT

Neutron stars with near-Eddington observable luminosities were shown to harbour levitating atmospheres, suspended above their surfaces. We report a new method to simultaneously measure the mass and radius of a neutron star based on oscillations of such atmospheres. In this paper, we present an analytic derivation of a family of relativistic, oscillatory, spherically symmetric eigenmodes of the optically and geometrically thin levitating atmospheres, including the damping effects induced by the radiation drag. We discover characteristic maxima in the frequencies of the damped oscillations and show that from a measurement of the frequency maximum and of the luminosity one can determine the mass and radius of the neutron star. In addition to the stellar parameters, observation of the variation of the oscillation frequencies with flux would allow us to estimate the stellar luminosity and therefore the distance to the source with an accuracy of a few per cent. We also show that the ratio of any two undamped eigenfrequencies depends only on the adiabatic index of the atmosphere, while for the damped eigenfrequencies, this ratio varies with the luminosity. The damping coefficient is independent of the mode number of the oscillations. Signatures of the dynamics of such atmospheres will be reflected in the source's X-ray light curves.

Key words: gravitation – radiation: dynamics – stars: atmospheres – stars: neutron – X-rays: bursts – X-rays: stars.

1 INTRODUCTION

Neutron stars are the most compact non-singular objects observed in the Universe. The theoretical densities of these objects range from about $10^4 \, \mathrm{g \, cm^{-3}}$ at the surface of the crust (Chamel & Haensel 2008) to above nuclear density of around $10^{14} \, \mathrm{g \, cm^{-3}}$ in the core (Rhoades & Ruffini 1974). The physics governing the equation of state at such large densities becomes uncertain, and a wide range of equations of state has been proposed, each producing different mass–radius relations, for neutron stars (Arnett & Bowers 1977; Cooperstein 1988; Cook, Shapiro & Teukolsky 1994; Lattimer 2012). Accurate measurements of both the mass and radius of neutron stars are necessary for constraining the equation of state, and thus the physics of highly dense material. Precise measurements of the mass are possible for pulsars in binary systems (Hulse & Taylor 1975; Özel & Freire 2016). In semidetached low-mass X-ray binaries (LMXBs), stellar masses can only be roughly estimated by the usual methods of determining the orbital parameters (Charles 2011).

Measurements of radius are more difficult and they are usually performed for X-ray sources that are not radio pulsars. Most methods involve X-ray spectroscopy, for example during thermonuclear bursts, when the redshift may be inferred by comparing the flux at maximum radius expansion of the burst with that at 'touchdown' (Ebisuzaki 1987; van Paradijs & Lewin 1987; Damen et al. 1990; Nättilä et al. 2016), or in the quiescent state of LMXBs (Brown, Bildsten & Rutledge 1998; Marino et al. 2018). The determined radius usually depends on the mass – in this sense the spectral method yields simultaneous measurements of both the mass and the radius, although the confidence contours give rather large (banana-shaped) allowed areas in the mass–radius plot (e.g. Bogdanov et al. 2016). To date, sufficiently accurate results have not been obtained, or at least in enough systems, to effectively measure the equation of state, although constraints have been imposed.

We have found a new method for an accurate simultaneous measurement of both the mass and the radius based on the expected timing properties of accreting neutron stars at near-Eddington luminosities, if the distance is known. Potentially, if a certain type of atmospheric oscillation is detected over a wide range of X-ray fluxes in an X-ray burst source, the distance to the source will also be directly measurable from the timing properties.

★ E-mail: deepika@camk.edu.pl

Super-Eddington luminous neutron stars are observed in various astrophysical phenomena and it is understood that such high luminosities are powered by the accretion of matter on to the stellar surface or surface nuclear burning. Recent studies have reported highly luminous neutron stars to be such accretors in pulsing ultraluminous X-ray sources NGC 7793 P13, NGC 5907, NuSTAR J09551+6940.8, NGC 300 ULX1 (Bachetti et al. 2014; Israel et al. 2017a,b; Carpano et al. 2018). Super-Eddington luminosity has long been known to occur during the outbursts in a few transient X-ray binaries, e.g. A0538–66, SMC X-1 and GRO J1744–28 (Skinner et al. 1982; Sazonov, Sunyaev & Lund 1997; Coe et al. 1981), and during the X-ray bursts.

Type-I X-ray bursts, are powered by thermonuclear burning of accreted material, during which neutron stars often reach Eddington luminosities (Lewin, Vacca & Basinska 1984; Tawara et al. 1984; Lewin, van Paradijs & Taam 1993). Spectral-timing analysis of these X-ray bursts shows periodic intensity variations that are termed as burst oscillations (Strohmayer & Bildsten 2006). Such oscillations have been observed to occur during the rise, peak and/or decay phases of the X-ray bursts with typical frequency range within 245–620 Hz (Strohmayer et al. 1996; Watts 2012). Burst oscillations during the rise phase are usually attributed to the rotational modulation of the hot spot corresponding to flame propagation on the stellar surface. Observations of burst oscillations from nuclear powered pulsars that emit persistent accretion-powered pulsations have shown that the burst oscillation is correlated with the spin of the neutron star in SAX J108.4–3658 (Chakrabarty et al. 2003) and 4U 1636–53 (Strohmayer & Markwardt 2002). However, the origin of burst oscillations that occur during the decay phase of the X-ray bursts is not yet well understood. Here, we explore another possibility of understanding these frequencies along with a new method to measure the mass and radius of accreting neutron stars in the context of the radial oscillations of 'levitating atmospheres'.

For compact stars with Eddington luminosities, radiation pressure becomes quite significant close to the stellar surface and thus has a strong influence on the dynamics of the ambient material. There is an effect unique to general relativity when examining the forces on the fluid outside a highly luminous star. If we take the fluid to be optically thin, then there exists exactly one radius, r_0, where the gravitational acceleration is balanced by the radiative force of a spherically symmetric star (Abramowicz, Ellis & Lanza 1990). The force balance can be described by an effective potential well centred at r_0. Later studies on the motion of test particles in the combined field of gravitation and radiation have shown that the radiation drag has significant effects on the particle dynamics (Bini, Jantzen & Stella 2009; Sok Oh, Kim & Mok Lee 2011; Stahl et al. 2012). A particle orbiting a highly luminous star has its angular momentum removed by the radiation field due to the Poynting–Robertson effect (or radiation drag effect), causing it to come to rest at this special radius r_0. For this reason, this radius is also deemed as the 'Eddington capture sphere', or ECS (Wielgus et al. 2012; Stahl et al. 2013). These results generalize to a shell of optically thin fluid, in which case a stable levitating atmosphere suspended around r_0 is formed (Wielgus et al. 2015), which is completely supported by the radiation pressure, and not in contact with the star at all. It has been proposed that oscillations of these radiation supported atmospheres could be good candidates to explain the oscillation frequencies observed during Type I X-ray bursts. Abarca & Kluźniak (2016) examined the lowest order, incompressible, radial mode of such atmospheres, and found it to be overdamped by radiation drag. Encouraged by the possibility of higher order modes, Bollimpalli & Kluźniak (2017), performed a full analysis in a Newtonian framework without radiation drag, finding a family of eigenmodes with promising eigenfrequencies. For values typical for a near-Eddington neutron star, the natural frequency is right around 600 Hz. What remains to be done is a similar analysis in a general relativistic framework with a proper treatment of radiation drag, in quest for underdamped oscillations. In this paper, we perform such an analysis.

The paper is outlined as follows. In Section 2, we give a pedagogical introduction to the radius of 'force balance' and to the fundamental frequencies. We shall then discuss in Section 3, the necessary equilibrium conditions for levitating atmospheres and derive a family of relativistic eigenmodes and eigenfrequencies of the radial oscillations. Damping of oscillations owing to radiation drag effect is investigated and an analytical expression for the damping coefficient is also found. In Section 4, we demonstrate how a new method to measure the mass and radius of neutron stars emerges from a unique maximum frequency treated as a function of stellar luminosity, mass and radius, as well as the oscillation mode. In Section 5, we show how observing changes in the frequency over a wide range of X-ray fluxes would allow a determination of the distance to the source as well. We conclude the paper by a discussion (Section 6) and a summary of the results (Section 7).

2 FUNDAMENTALS OF LEVITATING ATMOSPHERE OSCILLATIONS

Radial oscillations of levitating atmospheres have been previously investigated for special cases (Abarca & Kluźniak 2016; Bollimpalli & Kluźniak 2017), and the current paper aims to present a general study of these oscillations, including radiation drag in the relativistic regime. Before turning to rigorous calculations (Section 3 and following), we present a heuristic derivation of the fundamental mode frequency of the levitating atmosphere.

The usual Eddington luminosity derivation assumes that both the radiative flux and the force of gravity are inversely proportional to the square of the radius, r, of a spherical surface concentric with the star. In general relativity, this is no longer the case – because it is redshifted, the radiative flux decays with distance more rapidly than the gravitational acceleration – and (in the spherically symmetric case) there will be only one particular radius, r_0, at which the radiative force on the electron of a stationary hydrogen atom can balance the gravitational acceleration of the proton. At lower radii, radiation force dominates over gravity and so (in Newtonian language) the net force is directed away from the star, towards the ECS at r_0. At larger radii, beyond r_0, gravitational attraction dominates the radiation force and so the net force is directed towards the star, i.e. again towards the ECS. A stable, optically thin fluid shell may therefore be positioned at $r \approx r_0$. In hydrostatic equilibrium, the net force ('effective gravity') is balanced by the fluid pressure gradient – thus at r_0, where the effective gravity vanishes, the pressure is at its maximum.

If the radial extent of such a fluid shell is much smaller than r_0 ('thin atmosphere limit'), its fundamental mode of radial oscillations corresponds to uniform radial displacement by a distance $\delta s(r, t) = \delta s(t) = (1 + z)\delta r(t)$ – the redshift factor $(1 + z)$ accounting for the difference between proper and coordinate distance – with the shell suffering a restoring force per unit mass of $-\omega^2 \delta s(t)$, resulting

in harmonic radial oscillations at the (locally observed) frequency $\omega = \sqrt{(\mathrm{d}\,f_\mathrm{g}/\mathrm{d}\,r)(\delta r/\delta s)}$, with $f_\mathrm{g}(r)$ being the value of the net force per unit mass at r, and the derivative evaluated at r_0.[1]

To derive r_0 and ω, we note that for an observer measuring the stellar luminosity, both the frequency of the photons and the rate of the arrival of photons are gravitationally redshifted, introducing two redshift factors, i.e. $(1 + z)^{-2}$. Therefore, for a static, spherically symmetric field around a star with mass M and radius r_*, a local observer at radius r measures the stellar luminosity $L(r)$ to be decreasing with the radial coordinate as

$$L(r) = L_\infty \left(1 - \frac{2GM}{rc^2} \right)^{-1}$$
$$= L_* \left(1 - \frac{2GM}{r_*c^2} \right) \times \left(1 - \frac{2GM}{rc^2} \right)^{-1}, \qquad (1)$$

where L_∞ is the luminosity measured by a distant observer ($r \to \infty$), L_* would be measured at the stellar surface, and $1 + z = [1 - 2GM/(rc^2)]^{-1/2}$ is the redshift factor.

Now, the gravitational acceleration of a static observer at radius r is given by $GMr^{-2}(1 + z)$. Therefore, at the radius r_0, where the gravitational acceleration and the radiative force of the star balance each other at local luminosity $L(r_0)$, one has

$$L_\mathrm{Edd} \left(1 - \frac{2GM}{r_0c^2} \right)^{-1/2} = L(r_0) = L_\infty \left(1 - \frac{2GM}{r_0c^2} \right)^{-1}, \qquad (2)$$

where $L_\mathrm{Edd} = 4\pi cGM/\kappa$ is the usual expression for the Eddington luminosity, with the opacity given by κ. Defining

$$\lambda = L_\infty / L_\mathrm{Edd} \qquad (3)$$

for our convenience, we immediately obtain

$$\lambda = \left(1 - \frac{2GM}{r_0c^2} \right)^{1/2} \qquad (4)$$

from equation (2), and the radius of equilibrium follows as (Abramowicz et al. 1990; Stahl et al. 2013)

$$r_0 = \frac{2GM}{c^2(1 - \lambda^2)}. \qquad (5)$$

For a fixed value of λ, the radius scales directly with mass, as is usual in general relativity.

The radiative force per unit mass is $\kappa L(r)/(4\pi cr^2) = \lambda (GM/r^2)[1 - 2GM/(rc^2)]^{-1}$, where we used the first equality in equation (1) and the definition of λ and L_Edd. The locally observed eigenfrequency of the fundamental mode, ω, and its counterpart observed at infinity, $\omega_r = \omega/(1 + z)$, can now easily be obtained by expanding to first order in $r - r_0$ the expression for the effective gravity (difference between the radiative force per unit mass and the acceleration of gravity)

$$-\frac{GM}{r^2} \left[\left(1 - \frac{2GM}{rc^2} \right)^{-1/2} - \left(1 - \frac{2GM}{rc^2} \right)^{-1} \left(1 - \frac{2GM}{r_0c^2} \right)^{1/2} \right]$$
$$\approx -\left(\frac{GM}{r_0^2c} \right)^2 (1 + z)^2 \delta s \equiv -\omega^2 \delta s.$$

[1]The higher radial modes are more difficult to derive, as pressure variations play a role in determining the oscillatory motion. For example, the next higher mode is a breathing mode in which the oscillatory motion can be described as expansion away and contraction towards the ECS, with the (only) node at the ECS (Bollimpalli & Kluźniak 2017).

Finally (Abarca & Kluźniak 2016),

$$\omega_r = \frac{GM}{r_0^2c} = \frac{c^3(1 - \lambda^2)^2}{4GM}. \qquad (6)$$

Note the $1/M$ general relativistic (GR) scaling of the frequency:

$$\omega_r = \frac{c^3}{GM} \left(\frac{GM}{r_0c^2} \right)^2, \qquad (7)$$

the expressions in parentheses being constant for fixed λ in equations (5)–(7). As the observable frequency depends on the observed flux and the neutron star mass, it is then possible to determine the stellar mass from the two observables, ω_r and L_∞. In the following sections, we will see that when radiation drag is included in the calculation, the frequency has a maximum corresponding to a location of the levitating atmosphere that is quite close to the stellar surface, $r_0 \approx r_*$. As r_0 is also determined from the two observables, this allows a determination of the stellar radius as well. More precise statements can be found in the remainder of the paper.

3 LEVITATING ATMOSPHERES: HYDROSTATIC EQUILIBRIUM AND RADIAL OSCILLATIONS

In this section, we present the full general relativistic calculations for radial perturbations of an optically thin levitating atmosphere. We adopt the natural system of units in which $G = 1 = c$. We assume a static spherically symmetric space–time for the background solution, thereby the line element for a Schwarzschild metric with signature $(-, +, +, +)$ is given by

$$\mathrm{d}s^2 = g_{ij}\mathrm{d}x^i\mathrm{d}x^j = -B\mathrm{d}t^2 + B^{-1}\mathrm{d}r^2 + r^2(\mathrm{d}\theta^2 + \sin^2\theta\,\mathrm{d}\phi^2), \quad (8)$$

where we have introduced

$$B \equiv 1 - \frac{2M}{r} = -g_{tt} = g^{rr}. \qquad (9)$$

We assume a perfect fluid with stress energy tensor $T^{\mu\nu} = (\epsilon + p + \rho)u^\mu u^\nu + pg^{\mu\nu}$, where u^μ is the four-velocity, ϵ is the internal energy, and ρ, p are rest mass density and pressure of the flow, respectively. For the relevant gas temperatures, $T < 10^{10}\,K$, it is safe to assume that $\rho \gg p + \epsilon$. We keep this simplifying assumption throughout the work.

We start with the governing equations of fluid dynamics; the continuity equation reads

$$\nabla_\mu (\rho u^\mu) = 0, \qquad (10)$$

where ∇_μ is the covariant derivative. The conservation of energy–momentum is given by

$$\nabla_\mu T^{\mu\nu} = G^\nu, \qquad (11)$$

where G^ν is the radiation four-force density (Mihalas & Mihalas 1984). For electron-scattering-dominated regions, $G^\nu = \kappa\rho F^\nu$, where κ is the scattering opacity and F^ν is the radiation flux. Using the projection tensor $h^\nu_{\ \mu} = \delta^\nu_{\ \mu} + u^\nu u_\mu$, this quantity can be determined through the radiation stress–energy tensor, $R^{\mu\nu}$, as $F^\nu = h^\nu_{\ \lambda} R^{\mu\lambda} u_\mu$. Under the optically thin limit, all components of $R^{\mu\nu}$ for an isotropically radiating star were first presented in Abramowicz et al. (1990) and we adopt the same here. The relevant components of the radiation stress–energy tensor are

$$R^{tt} = \frac{L(r)}{2\pi r_*^2} \left(1 - \frac{2M}{r_*} \right) \left(1 - \frac{2M}{r} \right)^{-2} (1 - \cos\alpha), \qquad (12)$$
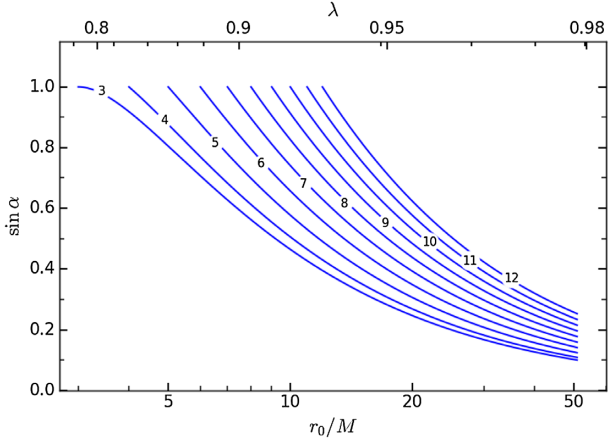
Figure 1. The sine of the viewing angle as a function of the ECS location, plotted for a range of stellar radii $r_* = 3$–$12M$ (from left to right).

$$R^{tr} = \frac{L(r)}{4\pi r_*^2} \left(1 - \frac{2M}{r_*}\right) \left(1 - \frac{2M}{r}\right)^{-1} \sin^2 \alpha, \quad (13)$$

$$R^{rr} = \frac{L(r)}{6\pi r_*^2} \left(1 - \frac{2M}{r_*}\right) (1 - \cos^3 \alpha). \quad (14)$$

where r_* is the radius of the star, and α is the viewing angle, which is the maximum polar angle up to which an observer at radius r can see the photons from the stellar surface. For simplicity, we assumed that the stellar radius is beyond the photon orbit, $r_* > 3M$, which gives[2]

$$\sin \alpha = \frac{r_*}{r} \left(1 - \frac{2M}{r}\right)^{1/2} \left(1 - \frac{2M}{r_*}\right)^{-1/2}. \quad (15)$$

The dependence of $\sin \alpha$ on r_0 is shown in Fig. 1 for several stellar radii.

The radial component of the relativistic Euler equation for an optically thin gas subject to the radiation field becomes

$$u^\mu \nabla_\mu u^r + \left(g^{\mu r} + u^\mu u^r\right) \frac{\nabla_\mu p}{\rho} + \kappa u_\mu \left(R^{r\mu} + u^r u_\nu R^{\mu\nu}\right) = 0. \quad (16)$$

We have assumed a uniformly radiating star, which may be a good description of a neutron star undergoing an X-ray burst. For an accreting and rotating neutron star, a rotating, radiating and levitating belt in the boundary layer has been shown to form due to the balance of gravitation, centrifugal and radiation forces; as the accretion rate approaches the near-Eddington luminosities, this belt extends from the equatorial plane up to the pole, allowing the entire surface of the neutron star to radiate (Inogamov & Sunyaev 1999). Thus, the spherically symmetric envelope may be a useful approximation even for a rotating neutron star accreting through a disc.

3.1 Geometrically thin background solution

Initially, the atmosphere is in hydrostatic equilibrium with a normalized four-velocity, u^t, given by $(B^{-1/2}, 0, 0, 0)$. Following

[2]Refer to Abramowicz et al. (1990) for details.

equation (16), the hydrostatic equilibrium condition for a spherically symmetric and optically thin levitating atmosphere around a uniformly radiating star is (Wielgus et al. 2015)

$$\frac{1}{\rho} \frac{dp}{dr} = -\frac{M}{r^2 B} \left(1 - \frac{\lambda}{B^{1/2}}\right). \quad (17)$$

Note that the location of the pressure maximum from the above equation, at $\lambda = B_0^{1/2}$, corresponds to the location of the ECS, r_0, see also equation (5),

$$r_0 = \frac{2M}{1 - \lambda^2}. \quad (18)$$

Quantities with subscript 0 are evaluated at the ECS, e.g. $B_0 \equiv B(r_0) = 1 - 2M/r_0$. Analytical solutions of an optically and geometrically thin polytropic atmosphere show that the density and pressure have Gaussian-like profiles (Wielgus et al. 2015) with the maximum located at r_0. Here, we present such solutions in a form usable for the calculation of normal modes. The procedure is quite similar to the one employed in the task of finding normal modes of oscillating tori (see e.g. Blaes, Arras & Fragile 2006). The main difference is that in the currently considered case the radiation force, rather than the centrifugal force, balances gravity in the background solution. The simplification is that the current problem has a spherical symmetry; hence, we obtain ordinary (and not partial) differential equations. Denoting $\mathcal{E} = -u_t = B^{1/2}$, we define an effective potential $\mathcal{U}_{\text{eff}}$ such that

$$\frac{1}{\rho} \frac{dp}{dr} = -\frac{\mathcal{E}^2}{2} \frac{d\mathcal{U}_{\text{eff}}}{dr}. \quad (19)$$

Using equation (17) and integrating, we find

$$\mathcal{U}_{\text{eff}} = -B^{-1} + \frac{2\lambda}{3} B^{-3/2}. \quad (20)$$

Casting the equation of hydrostatic equilibrium as

$$\frac{1}{\rho} \frac{dp}{dr} + \frac{\mathcal{E}_0^2}{2} \frac{d\mathcal{U}_{\text{eff}}}{dr} = -\frac{1}{2} \left(\mathcal{E}^2 - \mathcal{E}_0^2\right) \frac{d\mathcal{U}_{\text{eff}}}{dr} \quad (21)$$

allows us to express the right-hand side of the equation as a gradient of a scalar function, ψ. For a polytropic fluid with an adiabatic index $n, p \propto \rho^{(1 + 1/n)}$, we may integrate equation (21) to find the Bernoulli equation in the following form:

$$(1 + n)\frac{p}{\rho} + \frac{1}{2}\mathcal{E}_0^2 \mathcal{U}_{\text{eff}} + \psi = \text{const.} \quad (22)$$

After evaluating the constant at the ECS and some reordering, this integral condition can be cast as

$$\frac{p}{\rho} = \frac{p_0}{\rho_0} \left\{1 - \frac{1}{n c_{s,0}^2} \left[\frac{\mathcal{E}_0^2}{2} \left(\mathcal{U}_{\text{eff}} - \mathcal{U}_{\text{eff},0}\right) + \psi - \psi_0\right]\right\}, \quad (23)$$

with the speed of sound (squared) $c_s^2 = dp/d\rho$.

So far we did not explicitly assume that the background solution should be geometrically thin. We make this simplification now, by approximating the right-hand side of equation (23) with the second-order Taylor expansion around r_0, noticing that

$$\left.\frac{d\mathcal{U}_{\text{eff}}}{dr}\right|_{r_0} = \left.\frac{d\psi}{dr}\right|_{r_0} = \left.\frac{d^2\psi}{dr^2}\right|_{r_0} = 0. \quad (24)$$

The approximation holds for atmospheres that are sufficiently geometrically thin to neglect the gradient of the potential, i.e. the radial variation of space–time curvature and the radiation field, in comparison with the gradient of pressure. Hence, it is acceptable

for atmospheres with thickness much less than r_0. The following approximate formula is obtained:

$$\frac{p}{\rho} \approx \frac{p_0}{\rho_0}\left[1 - \frac{1}{nc_{s,0}^2}\frac{\mathcal{E}_0^2}{2}\frac{d^2\mathcal{U}_{\mathrm{eff}}}{dr^2}\frac{(r-r_0)^2}{2}\right] \equiv \frac{p_0}{\rho_0}f. \qquad (25)$$

Seeing how

$$\frac{-g_{tt}(r_0)\mathcal{E}_0^2}{2g_{rr}(r_0)}\frac{d^2\mathcal{U}_{\mathrm{eff}}}{dr^2}\bigg|_{r_0} = \frac{\lambda^6}{2}\frac{d^2\mathcal{U}_{\mathrm{eff}}}{dr^2}\bigg|_{r_0} = \left(\frac{M}{r_0^2}\right)^2, \qquad (26)$$

this result can be cast in a more compact form using the following substitutions:

$$\omega_r^2 = \left(\frac{M}{r_0^2}\right)^2, \qquad (27)$$

$$\beta = \frac{\sqrt{2n}\,c_{s,0}\lambda}{r_0}, \qquad (28)$$

$$x = \frac{r - r_0}{r_0}\sqrt{g_{rr}}, \qquad (29)$$

$$\eta = \frac{\omega_r}{\beta}x, \qquad (30)$$

with a simple interpretation: ω_r corresponds to the fundamental oscillation angular frequency, already familiar from equation (6), parameter β controls the geometric thickness of the atmosphere, x and η correspond to a convenient scaling of the radial coordinate. Thus, equation (25) for the radial profile of pressure may be rewritten simply as

$$\frac{p}{\rho} \approx \frac{p_0}{\rho_0}\left(1 - \frac{\omega_r^2}{\beta^2}x^2\right) = \frac{p_0}{\rho_0}(1 - \eta^2) = \frac{p_0}{\rho_0}f. \qquad (31)$$

3.2 Perturbations of the geometrically thin solution

We assume coherent, spherically symmetric perturbations of physical variable X in the form of

$$\widehat{\delta X}(r,t) = \delta X(r)\exp(-i\omega t) \qquad (32)$$

and linearly perturb the relevant hydrodynamic equations. The first thing to notice is that $\delta u^t = 0$ is necessary to fulfil the perturbed four-velocity norm, as $u_r = 0$ in

$$u_r\delta u^r + u_t\delta u^t = 0. \qquad (33)$$

The linearly perturbed version of the continuity equation takes the following form:

$$-i\omega B^{-1/2}\frac{\delta\rho}{\rho} + \frac{d}{dr}\delta u^r + \frac{1}{\sqrt{-g}\rho}\frac{d\left(\sqrt{-g}\rho\right)}{dr}\delta u^r = 0. \qquad (34)$$

The perturbed radial Euler equation yields

$$-i\omega u^t\delta u^r + g^{rr}\frac{d}{dr}\left(\frac{\delta p}{\rho}\right) + \delta\mathcal{D} = 0, \qquad (35)$$

where $\delta\mathcal{D} = \kappa\left(u_t^2 R^{tt} + g_{rr}R^{rr}\right)\delta u^r$ relates to the radiation drag acting against the radial motion of the particle and can be rewritten as

$$\delta\mathcal{D} = \frac{2}{3}\frac{M\left(1 - 2M/r_*\right)}{\lambda^3 r_*^2}(1 - \cos\alpha)(\cos^2\alpha + \cos\alpha + 4)\delta u^r$$

$$\equiv \chi\delta u^r, \qquad (36)$$

cf. equations (12)–(16). Although χ has a radial dependence through the cosine and sine functions of the viewing angle, in the geometrically thin limit $r \sim r_0$, hence χ will be taken to be constant for given stellar parameters and stellar luminosity.

Following Ipser & Lindblom (1992) and Abramowicz et al. (2006), we define a new variable,

$$W = -\frac{\delta p}{u^t\rho}. \qquad (37)$$

From the above definition and equation (35), it follows that in the geometrically thin limit

$$\delta u^r = i\frac{B}{\omega + i\chi\lambda}\frac{dW}{dr}. \qquad (38)$$

Substituting W in equation (34) and combining with equation (38) gives a single second-order ordinary differential equation. In the geometrically thin atmosphere limit ($\beta \to 0$), this equation simplifies to

$$f\frac{d^2W}{d\eta^2} - 2n\eta\frac{dW}{d\eta} + \frac{2n\omega^2}{\omega_r^2}\left(1 + i\frac{\chi\lambda}{\omega}\right)W = 0 \qquad (39)$$

with ω_r^2 given by equation (27). Note that equation (39) can be cast into a convenient dimensionless form

$$(1 - \eta^2)\frac{d^2W}{d\eta^2} - 2n\eta\frac{dW}{d\eta} + 2n\left(\sigma^2 + 2i\gamma\sigma\right)W = 0, \qquad (40)$$

with

$$\sigma \equiv \omega/\omega_r, \qquad (41)$$

$$\gamma \equiv \chi\lambda/(2\omega_r) = (4 - \cos^3\alpha - 3\cos\alpha)/(3\sin^2\alpha), \qquad (42)$$

and with the specific viewing angle given by

$$\sin\alpha = \frac{r_*}{r_0}\frac{(1 - 2M/r_0)^{1/2}}{(1 - 2M/r_*)^{1/2}}. \qquad (43)$$

As we will see, $\tau = 1/(\omega_r\gamma)$ is the decay constant (damping time scale) of the oscillatory solutions, so it is important to compare the value of the damping coefficient γ to the values σ of the (dimensionless) oscillation frequencies for the undamped solutions.

It is easy to show that outside the photon orbit, i.e. for $r_0 \geq 3M$, the viewing angle decreases monotonically with λ (or with the ECS radius r_0), and so does the damping coefficient γ. The maximum value of $\gamma = 4/3$ is attained at the stellar radius $r_0 = r_*$, and $\gamma \to 1$ as $r_0 \to \infty$, $\alpha \to 0$, $\lambda \to 1$. Thus, the radiative drag is always present in the problem at hand, with $4/3 \geq \gamma > 1$. None the less, it is instructive to consider a simplified problem in which radiative drag is artificially neglected.

3.3 Undamped oscillations

Let us now consider the artificial problem of undamped oscillations. This is obtained by blithely neglecting the damping term in equation (40), i.e. putting $\gamma = 0$, which leads to the Gegenbauer equation,

$$\left(1 - \eta^2\right)\frac{d^2W}{d\eta^2} - 2n\eta\frac{dW}{d\eta} + 2n\sigma^2 W = 0, \qquad (44)$$
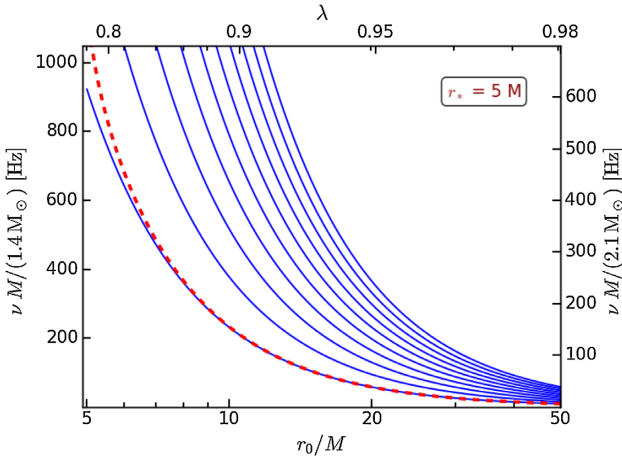
Figure 2. Frequencies of the ten first normal modes of undamped oscillations of the thin atmospheres as function of the atmosphere location. Frequencies scaled to fiducial masses $1.4\,M_\odot$ and $2.1\,M_\odot$ are shown on the left- and right-hand side vertical axes, respectively. Here, we assumed the stellar radius $r_* = 5M$. The dashed (red) line represents the damping rate, scaled in the same way, $\gamma \omega_r M/(2\pi M_{\text{fiducial}})$.

The corresponding solutions represent the undamped oscillations with the relativistic eigenfrequencies observed at infinity given by[3]

$$\omega_k^2 = \omega_r^2 \sigma_k^2, \tag{45}$$

where

$$\sigma_k^2 = \frac{k(k + 2n - 1)}{2n}. \tag{46}$$

The relativistic frequencies differ from the Newtonian ones (Bollimpalli & Kluźniak 2017) by a redshift related factor of λ^2, while the relativistic eigenmodes are similar to the Newtonian eigenmodes. Nevertheless σ_k, the ratio of normal mode frequencies to the fundamental mode frequency, remains the same for both the relativistic and non-relativistic cases. The ratio of frequencies of the second ('breathing') mode and the fundamental mode is $\sigma_2 = \sqrt{2 + 1/n}$.

The eigenfrequencies grow with the mode number; the first two are $\sigma_1 = 1 < \gamma$ and $\sigma_2^2 = 2 + 1/n > 2 > \gamma^2$. Thus, in the full problem, which includes radiative damping, the radial mode ($k = 1$) is overdamped (Abarca & Kluźniak 2016), but all the higher modes ($k \geq 2$) have an oscillatory character (are underdamped). This is also clear when we plot the frequencies, $\nu = \omega_k(r_0)/(2\pi)$, of the first ten modes of undamped oscillations (left to right), as a function of Eddington parameter or atmosphere location (Fig. 2).

The frequencies are plotted in Hz to facilitate comparison with observations. The values on the left vertical axis correspond to $M = 1.4\,M_\odot$. For a different mass, M, the frequency at a given r_0 and a given mode can be obtained with the scaling factor $M/(1.4\,M_\odot)$ shown on the left vertical axis. Frequencies computed for $2.1\,M_\odot$ are shown with similar scaling on the right vertical axis. The radius in units of the stellar mass has to be assumed a priori to compute these frequencies, we took $r_* = 5\,M$. For a given λ or r_0, higher number modes have larger frequencies. The further the atmosphere is located from the stellar radius, the lower the frequencies get as

the magnitude of the restoring forces decreases with the radius. This radial dependence is fully accounted for by the functional form of ω_r, given in equation (27). We note that there is a range of luminosities for which the frequencies of these oscillations fall in the range of 300–600 Hz, typical for observed frequencies of X-ray burst oscillations.

3.4 Damped oscillations

We now turn to the full problem including the damping effects of the ever-present radiation drag in radiation-supported atmospheres.

It is easiest to solve equation (40) by considering the real (σ_R) and imaginary (σ_I) parts of σ separately,

$$\sigma = \sigma_R + i\sigma_I, \tag{47}$$

and the corresponding relation $\omega = \omega_R + i\omega_I$, with $\omega_R = \omega_r \sigma_R$ and $\omega_I = \omega_r \sigma_I$. Substituting complex σ into equation (40) results in a differential equation with real and imaginary parts that are separable and can be solved simultaneously. The real part is an eigenvalue problem in the form of a Gegenbauer differential equation,

$$\left(1 - \eta^2\right) \frac{d^2 W}{d\eta^2} - 2n\eta \frac{dW}{d\eta} + 2n\left(\sigma_R^2 - \sigma_I^2 - 2\gamma\sigma_I\right) W = 0, \tag{48}$$

while the imaginary part yields

$$i 4n\sigma_R\left(\sigma_I + \gamma\right) W = 0. \tag{49}$$

A particularly simple solution corresponds to the overdamped case of purely imaginary σ. The eigenvalues are given by $-\sigma_I^2 - 2\gamma\sigma_I = \sigma_k^2$, giving

$$\sigma_I = -\gamma \mp \sqrt{\gamma^2 - \sigma_k^2}. \tag{50}$$

In fact, as follows from the discussion above, this solution only occurs for $k = 1$, for which $\sigma_k = 1$, corresponding to the imaginary frequency of the overdamped solution of

$$\omega = i\omega_{\text{OD}}, \tag{51}$$

with

$$\omega_{\text{OD}} = -\omega_r \left[\gamma \pm \sqrt{\gamma^2 - 1}\right]. \tag{52}$$

The time dependence of this decaying solution is $\exp(-i\omega t) = \exp(\omega_{\text{OD}} t)$.

In the general case, equation (48) can be solved with a proper boundary condition of pressure vanishing on the atmosphere boundary. The corresponding eigenmodes are represented by the Gegenbauer polynomials $C_k^\alpha(\eta)$ with $\alpha = n - \frac{1}{2}$ and $k = 0, 1, 2, 3, \ldots$ which can be calculated with a recursive formula (Koornwinder et al. 2010)

$$C_0^\alpha(\eta) = 1,$$

$$C_1^\alpha(\eta) = 2\alpha\eta,$$

$$kC_k^\alpha(\eta) = 2\eta\left(k - 1 + \alpha\right) C_{k-1}^\alpha(\eta) - (k - 2 + 2\alpha) C_{k-2}^\alpha(\eta). \tag{53}$$

They form a complete set of modes, that is, any spherically symmetric oscillation of the levitating atmospheres is necessarily a combination of the eigenmodes described by the equation (53). For example, the eigenfunctions of the second mode ($k = 2$) and the third mode ($k = 3$) take the form of $\left(n - \frac{1}{2}\right)[\eta^2(2n + 1) - 1]$

---

[3]Which can also be identified directly from equation (55) with the damping coefficient set to zero.

and $\frac{\eta}{6}(4n^2 - 1)[(2n + 3)\eta^2 - 3]$, respectively.[4] The above imply a non-vanishing eigenfunction W, and for $k > 1$ also $\sigma_R \neq 0$, so equation (49) simply gives the damping rate

$$\omega_I = -\omega_r \gamma. \tag{54}$$

Using this, the corresponding eigenfrequencies of the oscillations are computed from the Gegenbauer relation,

$$\omega_R^2 = \omega_r^2 \left(\sigma_k^2 - \gamma^2\right) = \omega_r^2 \left[\frac{k(k + 2n - 1)}{2n} - \gamma^2\right], \tag{55}$$

where $k = 2, 3, 4 \ldots$. Note that the time dependence of the solution is $\exp(-i\omega_R t - \omega_r \gamma t)$, so $1/(\omega_r \gamma)$ is the damping time. The damping coefficient γ has been defined in equation (42) and the fundamental frequency ω_r in equation (27).

The frequency ω_R^2 is a product of the fundamental frequency ω_r squared, which is a rapidly and monotonically decreasing function of the ECS radius r_0, and of a monotonically increasing function of the same variable, $\sigma_k^2 - \gamma^2(r_0)$. The product has a maximum, close to the stellar surface, even though the damping coefficient γ of equation (42) is a slowly varying function of the viewing angle, and σ_k is a constant. This is because close to the stellar surface, the angle α itself varies rapidly with r_0. Indeed,

$$\frac{d\gamma}{dr_0} = \frac{d\gamma}{d\alpha} \times \frac{1}{\cos\alpha} \times \frac{d\sin\alpha}{dr_0}, \tag{56}$$

and the second factor dominates the radial derivative of ω_R^2, as $\cos\alpha \to 0$ at $r_0 \to r_*$, where $\alpha \to \pi/2$, while the other terms are regular everywhere:

$$\frac{d\gamma}{d\alpha} = \frac{(1 - \cos\alpha)^3(3 + \cos\alpha)}{3\sin^3\alpha}, \tag{57}$$

$$\frac{d\sin\alpha}{dr_0} = -\frac{\sin\alpha}{r_0}\frac{(1 - 3M/r_0)}{(1 - 2M/r_0)}. \tag{58}$$

Thus, close to the stellar surface ω_R is a growing function of r_0, while at larger radii, over most of its range, ω_R decreases with distance to the star. Therefore, for any mode higher than the fundamental ($k > 1$), a maximum of the atmospheric oscillation frequency occurs close to the stellar surface. The fundamental mode ($k = 1$) is overdamped, and hence the maximum occurs in the inverse decay constant $|\omega_{OD}|$, as can be seen in Fig. 3.

Fig. 3 presents the frequencies $\omega_R(r_0)/(2\pi)$ of the initial few lowest modes of the underdamped oscillations in an increasing order of mode number from left to right. One may immediately notice from the figure that the frequencies of the modes have now decreased slightly due to damping. For the fundamental mode, we plot the magnitude, $|\omega_{OD}|/(2\pi)$, shown by the thin dashed line in the plot. The overdamped solutions are not of much astrophysical interest, so in further discussions we shall only consider the second and higher modes, as they allow for oscillations.

Observed oscillations in the X-ray bursts occur mainly during the rise and decay phase of the outburst (Muno et al. 2001). Interestingly, even with the damping, the observed range of 300–600 Hz still falls within the frequency range of these mode oscillations. Oscillations during the outburst decay phase are found to have increasing frequency with time (Strohmayer & Bildsten 2006). Equation (55) and Fig. 3 show that the frequencies increase

---

[4]As a reminder, n is the adiabatic index and η is a scaled radial coordinate (see equation 30).
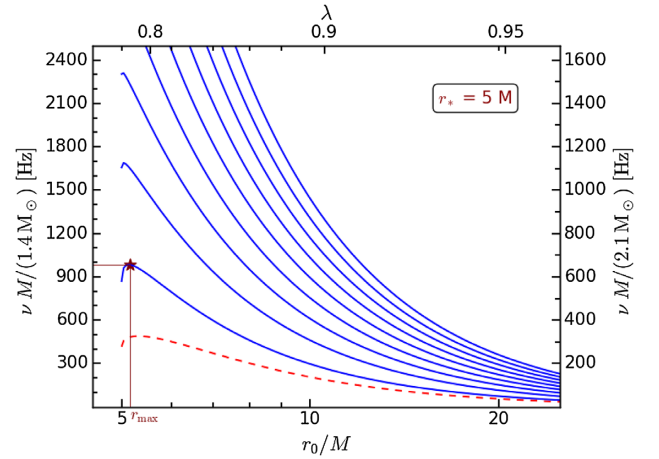
Figure 3. Frequencies of the 10 first normal modes of damped oscillations of the thin atmospheres as function of the atmosphere location. For the overdamped fundamental mode, $|\omega_{OD}|/(2\pi)$ is shown by dashed (red) line. Assumed stellar radius is $r_* = 5M$.

with decreasing luminosity (as long as the frequency maximum is not reached), which is in accord with the observed oscillations, since luminosity decreases with time during the decay phase of the outbursts, as the name suggests. However, the magnitude of the frequency increase in the optically thin model exceeds the observed changes.

In the following section, we present a method of simultaneous mass and radius measurements from the frequency maximum of the damped oscillations.

4 CHARACTERISTIC FREQUENCY MAXIMUM: MASS AND RADIUS DETERMINATION

While the frequency of the oscillations in general decreases with luminosity, a distinctive feature to be noted in Fig. 3 is the maximum in the frequencies of underdamped oscillations close to the stellar surface. For given stellar parameters, M, r_*, we mark the radius at which the atmosphere can oscillate with maximum frequency, ν_{max}, as r_{max}. The maximum for the second mode is clearly pronounced. For higher modes, since r_{max} is quite close to the stellar radius, it would be difficult to observe the decrease of frequency to the left of the maximum as the luminosity decreases. The presence of the frequency maximum can be identified as due to the steep radial decrease of damping close to the star which is mostly attributed to a rapid decrease in viewing angle, as remarked in Section 3.4, in the discussion of equation (56).

Fig. 4 shows for the first few underdamped modes the coordinate distance between the location of the atmosphere that corresponds to the maximum frequency and the stellar surface. Lower modes are comparatively farther away from the stellar surface, while the distance also increases with the stellar radius.

For a particular mode, this maximum of the frequency, ν_{max}, depends on two parameters (r_*, M). In Fig. 5, we plot the frequencies of the second mode for $1.4\,M_\odot$ and $2.1\,M_\odot$ stellar mass and various stellar radii. The following can be noted from the figure:

(a) For a given stellar mass, ν_{max} decreases with increasing r_*/M.

(b) For a given r_*/M, ν_{max} is inversely proportional to the stellar mass, as expected for GR scaling.
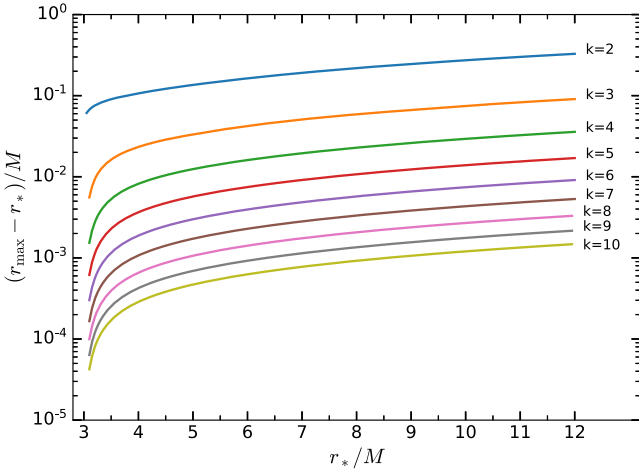
Figure 4. Distance between r_{max} location and the stellar surface for first few underdamped modes.
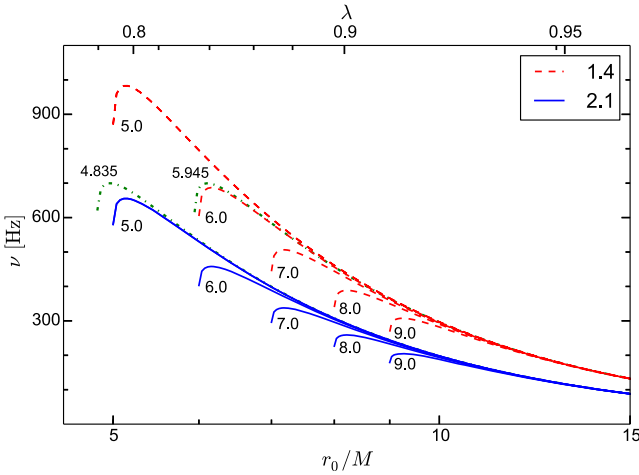
Figure 5. Behaviour of the second mode frequency maximum as function of r_0 for different stellar masses and radii. Dashed (red) curves are for $1.4 \, M_\odot$ and solid (blue) curves for $2.1 \, M_\odot$. Dash–dotted (green) lines represent the curves for both these masses with frequency maximum value of 700 Hz. For given mass, various stellar radii (r_*/M) chosen are marked for the curves in the figure.

(c) Irrespective of the values of r_*/M and M, r_{max} is always located close to the stellar surface.

(d) There is a degeneracy in the frequency maximum value that occurs for different combinations of r_*/M, r_{max}/M, and M. For example, two different stars with masses $1.4 \, M_\odot$ and $2.1 \, M_\odot$ and radii $5.945 \, M$ and $4.835 \, M$ exhibit the same frequency maximum value of 700 Hz when their respective locations of the atmosphere are at $6.1 \, M$ and $4.95 \, M$. These frequencies are plotted as green dash–dotted lines in Fig. 5. As we shall discuss below, the stellar luminosity breaks this degeneracy and allows us to obtain the stellar parameters unique to the corresponding frequency maximum.

(e) However, for a given r_*/M, the frequency maximum occurs at the same radius (in units of M), independent of the stellar mass. This follows immediately from equation (55), which is a function of r_*/M and r_0/M alone, once the $1/M$ dependence of ω_r is taken out. So, the condition for the maximum, i.e. the first derivative of the frequency with respect to r_0/M being set to zero, gives a relation just between the two radii r_*/M and r_{max}/M.

Given the frequency maximum value and the corresponding luminosity, we can determine the mass and radius of the neutron star. Indeed, we already know that for any single mode exhibiting a frequency maximum, we can now find the value of the dimensionless stellar radius, r_*/M, if we know r_{max}/M. We require one last relation to close the system of equations that enable us to solve for the two parameters (r_*, M). Equation (18) fulfils this requirement by providing a relation between M and r_{max} through λ or stellar luminosity.

To derive the stellar parameters, the set of nonlinear relations are solved semi-analytically using the following protocol:

(i) We derive λ as a function of M and L_∞ from equation (3), assuming the Eddington limit for ionized hydrogen. An atmosphere with a different composition would have a different Eddington limit and the x-axis of the plots in Figs 6(a) and (b) would then vary accordingly.

(ii) With the direct dependence on λ, r_{max}/M is then determined as a function of M and L_∞, using equation (5) with $r_0 = r_{max}$.

(iii) For the assumed mode number (say $k = 2$ or $k = 3$), we set the first derivative of frequency with respect to r_0 to zero to derive r_*/M as a function of r_{max}/M, and therefore as a function of M and L_∞.

(iv) The final equation for the frequency maximum is thus solely a function of mass and luminosity, so that given any two quantities, the other can be determined. Thus, given that we know the observed frequency maximum and luminosity, we can determine the mass of the star.

(v) Knowing M and r_*/M, we determine the stellar radius.

We admit a source of ambiguity in the measurements of radius and mass due to the mode number. The mode number is a discrete parameter, and so assuming different mode numbers introduces large discrete changes in the measured mass and radius. We expect the higher modes to be less likely to be excited than the breathing mode ($k = 2$), given their more complicated eigenfunctions. However, in any case, we believe it would in principle be possible to determine the mode number by observing the frequency variation with varying flux (luminosity) – the higher the mode number, the more rapid the variation, as is clear from Fig. 3.

In Figs 6(a) and (b), we show a grid of stellar mass and radius contours for a given range of luminosity and frequency maximum computed as described above for the second and third modes, respectively. The coloured contours (sloping upwards with luminosity) are for stellar radius in increasing steps of 0.5 km from top to bottom. The nearly vertical black contours represent mass in range of $1 \, M_\odot$ to $4 \, M_\odot$ in increasing steps of $0.05 \, M_\odot$ from left to right. At a given luminosity, ν_{max} of a star increases with its compactness. Since we assumed that the stellar surface lies above the photon orbit, we omit solutions with $r_* < 3M$. Hence, for combinations of higher luminosity and higher frequency maximum, we see no contours in the figures.

As we can note from the grid in the plots, each pair of stellar luminosity and frequency maximum thus gives a unique measure of the radius and mass of the neutron star. For example, if the observed frequency maximum is around 600 Hz and the corresponding luminosity of the star observed at this frequency is around $1.9 \times 10^{38} \, \text{erg s}^{-1}$, then assuming that the frequency corresponds to the second mode ($k = 2$), the determined stellar radius is 14.5 km and mass is $1.65 \, M_\odot$. If we assume the third mode ($k = 3$), then the determined stellar radius increases to 18.5 km and the mass estimate decreases to $1.6 \, M_\odot$.

(a) $k = 2$

(b) $k = 3$
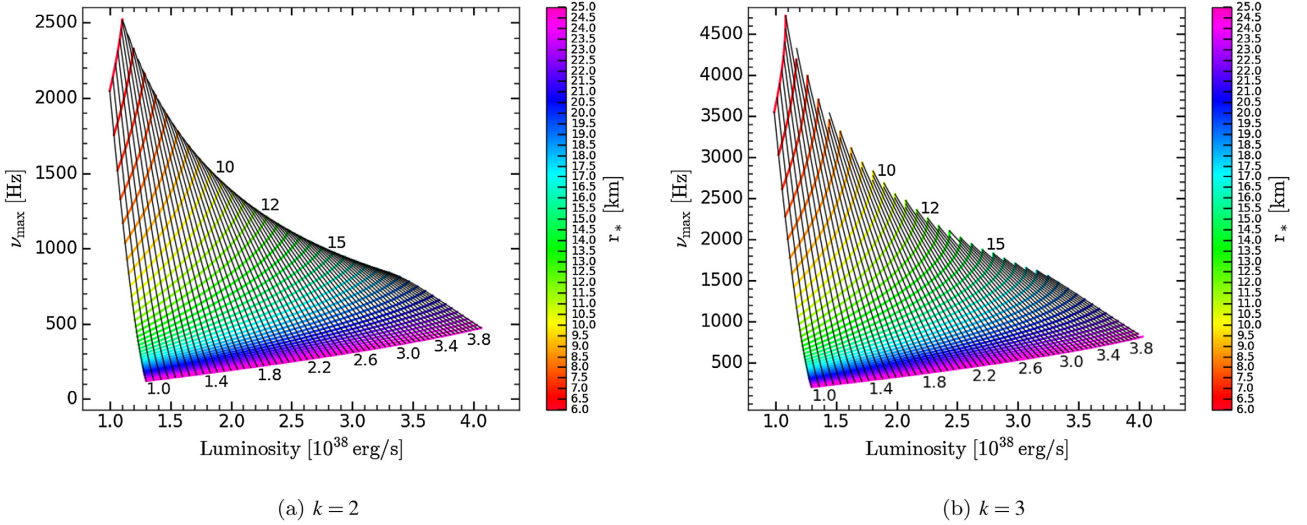
Figure 6. Mass and radius of neutron star for given luminosity and frequency of oscillations for the second and third modes. The lines sloping upwards are the contours of stellar radius in km, plotted in increasing steps of 0.5 km from top to bottom. The nearly vertical black lines are the contours of stellar mass, plotted in increasing steps of 0.05 $M_\odot$ from left to right.

Inferring the mass and radius of the neutron star through this method thus requires only a single observation of two quantities, luminosity, and frequency. However, this method is subject to certain systematic uncertainties, of which the most important is the uncertainty in the distance to the source, which translates directly into uncertainty in the luminosity, thereby leading to errors in the estimated mass and radius. We discuss these in the next subsection.

4.1 Error budget

The determination of the neutron star mass and radius, described in this section, would be quite accurate if the distance to the source were known quite precisely, as in the 47 Tuc globular cluster, with quoted distance $d = 4.53 \pm 0.06$ kpc (Woodley et al. 2012). Unfortunately, the distance errors to other globular clusters are less constrained, with uncertainties sometimes approaching 10 per cent (Guillot et al. 2013; Steiner et al. 2018). Typical errors on the distances to the neutron star LMXBs in the field are even larger, falling between 10–20 per cent (Galloway et al. 2008). Such large uncertainties in the distance imply that the typical uncertainties in luminosity can be around 20 per cent or higher.

Frequencies of oscillations, once detected, are typically much more precise. Planned, sensitive X-ray instruments, e.g. *STROBE-X* (Ray et al. 2019) and *eXTP* (Zhang et al. 2016), should be able to measure the frequencies to exquisite precision, given by the ratio of the oscillation period to the time-scale for frequency change (as the luminosity varies), which should be less than one part in a hundred. To be conservative, in the remainder of this section we assume a frequency error of 3 per cent. All the analysis throughout the rest of this paper considers only the second mode, i.e. $k = 2$.

To quantify the mass and radius errors, we do a simple χ^2-error analysis with chosen uncertainties in luminosities and frequencies. We assume that the luminosity and frequency maximum measurements are normally distributed, with different mean values for different cases. We consider the uncertainties on the luminosity and frequency to be 20 per cent and 3 per cent, respectively, which

are taken to be the standard deviations of the corresponding distributions. We consider six cases in total with the mean luminosities ($\bar{L}$) taken to be 1.8×10^{38} and 2.0×10^{38} erg s^{-1}, and the mean frequency maxima ($\bar{\nu}_{max}$) to be 300, 600, and 900 Hz. Fig. 7 shows the joint confidence regions for mass and radius for the six different cases with $\bar{L}$ and $\bar{\nu}_{max}$ given in the title of the each plot. The confidence regions are determined based on the $\Delta\chi^2$ values calculated with the chosen uncertainties. Overplotted black contours denote the 1σ, 2σ, and 3σ errors that correspond to the 68.27 per cent, 95.45 per cent, and 99.73 per cent confidence levels, respectively.

A projection of the 1σ contour ($\Delta\chi^2 = 1$) on to the corresponding axes yields upper limits to the 1σ errors on mass and radius, but the actual 1σ errors on the parameters are always smaller. As we cannot assert that these parameters have a Gaussian distribution, we turn to a Monte Carlo analysis to generate the probability distributions for mass and radius and to accurately determine the errors on their values.

We once again consider the six cases with the assumption that the frequency and luminosity are normally distributed with the mean values as given in the first two columns of Table 1 and with the same 3 per cent and 20 per cent uncertainties as before. For each such case, we perform a Monte Carlo simulation to generate a large ensemble of 10^8 pairs of luminosity and frequency maximum values that are normally distributed with the chosen $\bar{\nu}_{max}$ and $\bar{L}$. For each such pair of luminosity and frequency maximum, we compute the corresponding pair of mass and radius to generate the posterior distributions for the mass and radius. In Fig. 8, we show the distributions for mass and radius for one such case ($\bar{\nu}_{max} = 600$ Hz and $\bar{L} = 2.0 \times 10^{38}$ erg s^{-1}). The red solid line represents the median (50th percentile), while the red dashed lines denote 1σ error bounds (16th and 84th percentile). The central plot shows the contours of joint confidence regions at the levels 0.68 and 0.95. The 1σ errors on mass and radius determined through this method are given in the third and fourth columns of Table 1. The typical errors on mass and radius from this table are slightly larger than 20 per cent and 10 per cent, respectively.
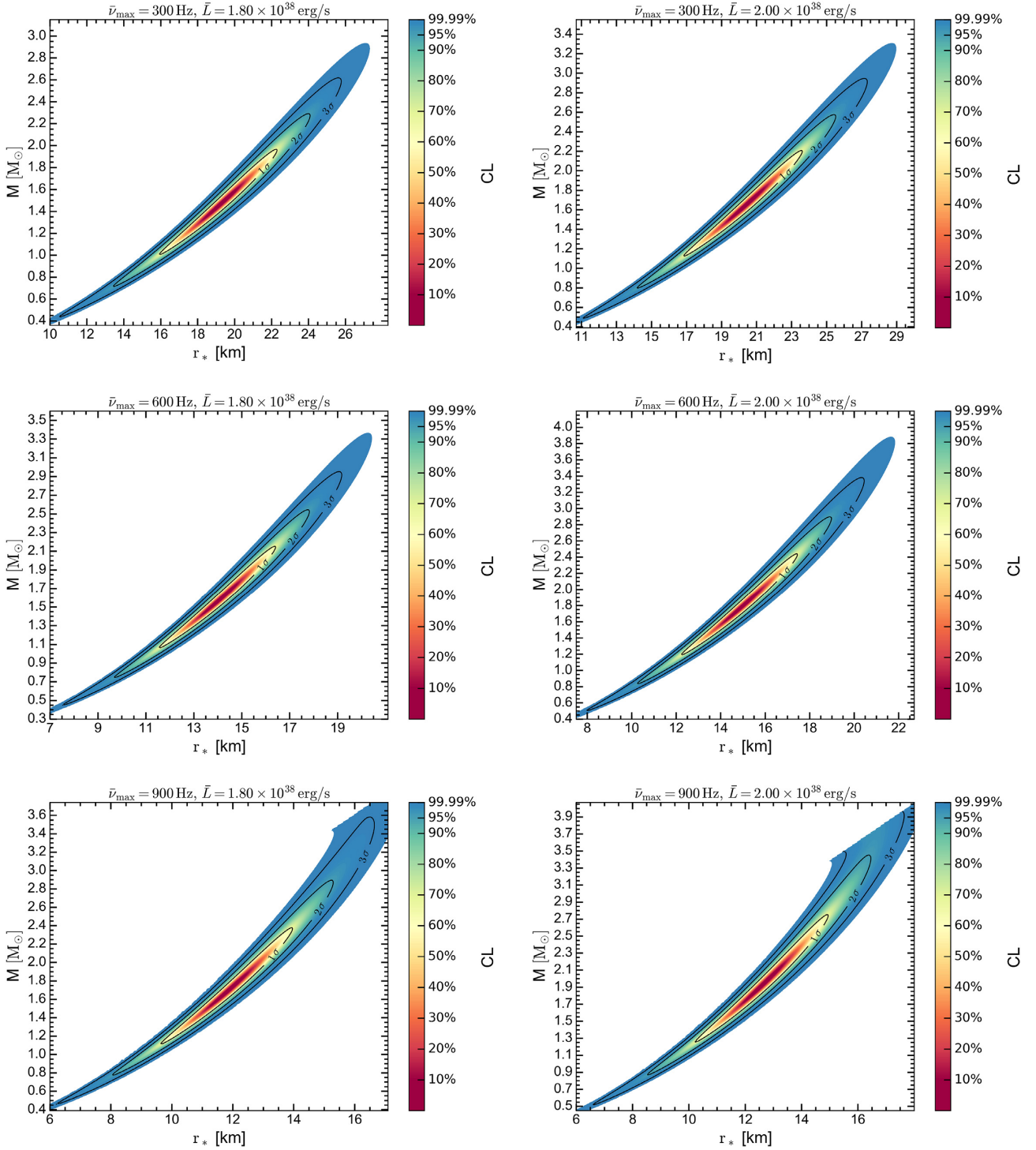
Figure 7. Contours of confidence levels (CL) for the mass and radius of the neutron star are shown corresponding to different mean values of frequency maximum $\bar{\nu}_{max}$ and luminosity ($\bar{L}$) as labelled in the titles of the plots. In all the plots, the errors on frequency maximum and luminosity are taken to be 3 per cent and 20 per cent, respectively. The 1σ, 2σ, and 3σ error contours are overplotted in black.

Therefore, we can say that with respective errors of 20 per cent and 3 per cent in luminosity and frequency, we can estimate the parameters of the neutron star with an accuracy of 20 per cent for mass and 10 per cent for radius. It is easy to see that the errors on mass and radius will be significantly lowered if the errors on luminosity can be decreased. Indeed, the uncertainty in

the determined values of mass and radius are of the order of the uncertainty in the luminosity.

Interestingly, if the oscillation frequency is observed over a wide range of fluxes, the neutron star mass and radius could be determined without prior knowledge of the distance to the source. In the following section, we discuss how to simultaneously determine

Table 1. Frequency maximum and luminosity are assumed to be normally distributed with the mean values as given in the first and second columns, with assumed errors of 20 and 3 per cent, respectively. Corresponding 1σ errors, which are given in the third and fourth columns, are determined from the probability distributions of mass and radius.

$\bar{v}_{max}$ (Hz)	$\bar{L}$ ($\times 10^{38}$ erg s^{-1})	M (M$_\odot$)	r_* (km)
300	1.8	$1.48^{+0.32}_{-0.32}$	$19.3^{+2.0}_{-2.2}$
300	2.0	$1.65^{+0.37}_{-0.35}$	$20.4^{+2.1}_{-2.3}$
600	1.8	$1.58^{+0.35}_{-0.32}$	$14.1^{+1.5}_{-1.6}$
600	2.0	$1.79^{+0.42}_{-0.40}$	$15.0^{+1.7}_{-1.8}$
900	1.8	$1.70^{+0.41}_{-0.37}$	$11.9^{+1.3}_{-1.4}$
900	2.0	$1.94^{+0.48}_{-0.44}$	$12.6^{+1.4}_{-1.5}$
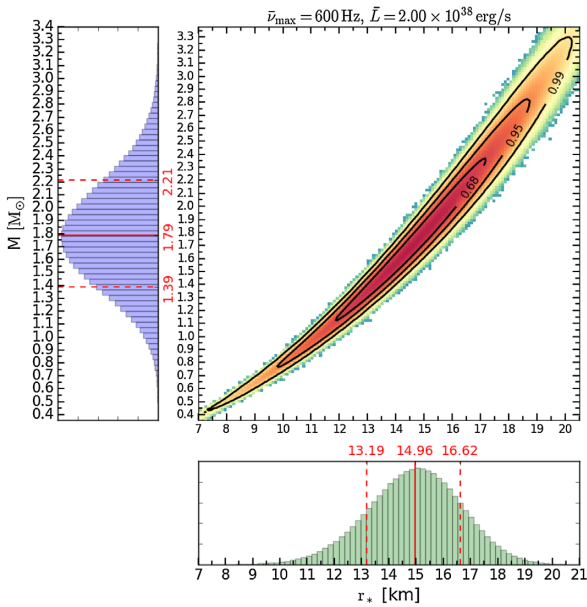
Figure 8. Probability distributions and mass and radius computed though the Monte Carlo simulations. The median and the 1σ range for each quantity are marked with solid-red and dashed-red lines. The central plot shows the joint confidence region for the two quantities, with the 68 per cent, 95 per cent, and 99 per cent confidence levels represented by the black contours.

the mass, radius, and distance to the source, and show that the errors on M, and r_* would be decreased by an order of magnitude relative to the errors discussed above.

5 MASS, RADIUS, AND DISTANCE DETERMINATION

One way to circumvent the problem with distance uncertainties is to consider the ratio of luminosities that essentially translates into flux ratio, which is a directly measurable quantity like frequency. The two green dash–dotted lines in Fig. 5 that share the same frequency maximum for different masses and radii show visibly different frequency variation with λ ($\propto L/M$), but the mass, and therefore λ as well, is not yet known, so in practice we cannot use this plot. In fact, let us assume that we do not know the distance to the source, so that we do not know the luminosity. None the

less, if we consider plotting the frequency variation with the flux ratio, which does not depend on the distance, we can distinguish the curves for different masses and radii. Suppose that we have a set of observed data points for frequency variation with flux. In principle, as per our model, there exists a unique pair of mass and radius, within error, that can fit all the observed data points. Although, in reality, if we do not have a sufficient number of data points, or data spanning a sufficiently wide range over frequencies, then a wide range of masses and radii can potentially fit the observed data points, thus making it difficult to stringently constrain the mass and radius (unless we already know the luminosity, in which case we can proceed as in Section 4).

To elaborate on this, we consider an example of frequency variation with luminosity for the parameters $M = 1.5$ M$_\odot$ and $r_* = 13.72$ km. The curve has $v_{max} = 600$ Hz and we chose five data points on this frequency curve corresponding to 550, 500, 450, 400, and 350 Hz with 1 per cent uncertainty. We can use these five data points as a proxy for the real observation data set and check to within what accuracy we can recalculate the values of mass and radius by finding the best fits to these points. Since we do not know the distance, these points can only be represented on the frequency-flux plane if we scale the corresponding luminosities of each point with the luminosity of any one particular point. This is the same as scaling the fluxes of the observed data points to the flux of one data point. In this example, we chose this reference point to be the one with frequency 600 Hz.

First, let us suppose that we have a precise measurement for the frequency maximum. In such a case, we can try to fit through all the points with the frequency curves for various mass and radius pairs that have the same $v_{max} = 600$ Hz, as shown in Fig. 9(a). The x-axis for each curve is scaled with its corresponding flux ($F_{v_{max}}$) at v_{max}. The lower we go in the frequency data compared to v_{max}, the better we can constrain the mass and radius measurements. An inspection of the plot close to the error bars located at 400 Hz and 350 Hz shows that we can already limit the errors on mass to a much better accuracy than ± 0.1 M$_\odot$. This can be better visualized in Fig. 9(b), which shows fits to the error bounds for each data point. This way the errors on mass and radius determined from the fits to the bounds of the 350 Hz error bar are a factor of 6 less compared to the errors from the fits to the 550 Hz error bar. So given a precise measurement for v_{max}, and a wide range of frequency measurements, the mass and radius can be estimated with relatively minor errors of < 2 per cent (± 0.027 M$_\odot$) and < 1 per cent (± 0.121 km), respectively.

Another potential source of error is from a measurement of the frequency maximum with given uncertainty just like the remaining data points. We fit three curves to the centre, lower end, and upper end of the error bars as shown in Fig. 10. The respective masses are labelled in the plot, and we see all the curves passing through the 'data' points in Figs 9 and 10 yield values of M and r_* within an error of less than 2 per cent.

Thus, we conclude that the overall error in the neutron star mass and radius determination by this method is of the same order as the assumed error in the measured frequencies (1 per cent), which would be an excellent result.

5.1 A note on distance estimates

With the above derived constraints on mass and radius for a known v_{max}, we can determine the luminosity and thereby the distance to the source with a high accuracy. In Fig. 11, we show a grid of v_{max} (nearly diagonal lines in black) and luminosity contours
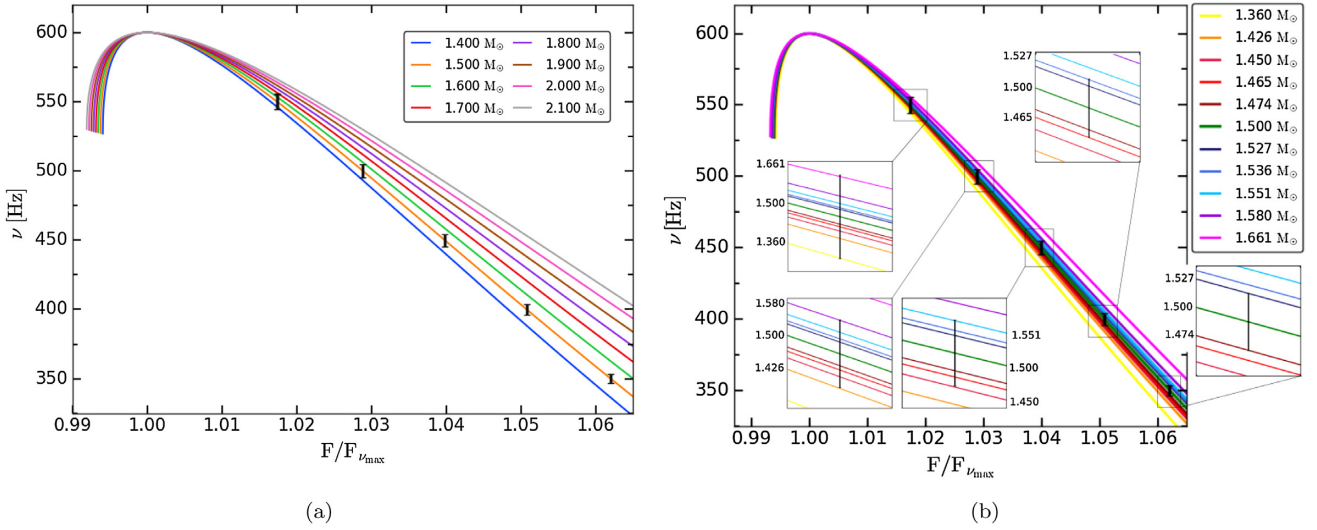
Figure 9. Frequency variation with flux for different masses labelled in the plot that have the same frequency maximum value at 600 Hz. In the left-hand panel (a), the increasing order of the curves (from the lowest curve in blue to the highest curve in grey) have their the corresponding masses increasing in steps of 0.1 $M_\odot$ and the respective radii are $r_* = 13.26, 13.72, 14.164, 14.594, 15.011, 15.416, 15.809, 16.192$ km. In the right-hand panel (b), the masses labelled in increasing order correspond to the increasing order of the curves with the respective radii given by 13.073, 13.38, 13.493, 13.559, 13.601, 13.72, 13.841, 13.881, 13.948, 14.076, 14.427 km.
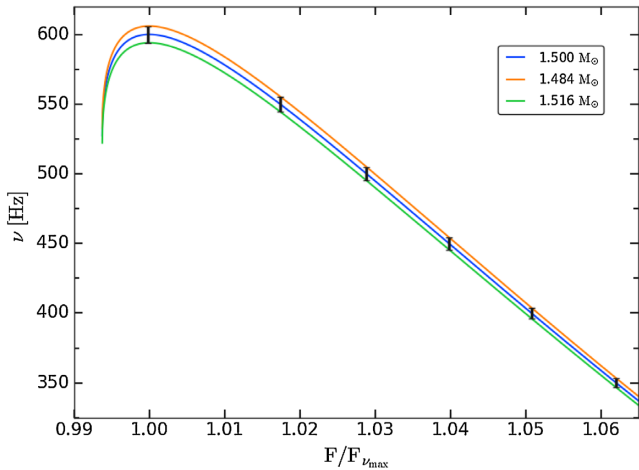
Figure 10. Frequency curve fits when the frequency maximum is also measured with an uncertainty. The respective radii for the curves with masses 1.5, 1.484, 1.516 $M_\odot$ are $r_* = 13.72, 13.579, 13.862$ km.

(coloured downward sloping lines) plotted for a wide range of masses and radii. The red crosses lying close to the intersection of $\nu_{max} = 600$ Hz and $L = 1.70 \times 10^{38}$ erg s^{-1} contours mark the mass and radius errors estimated with 1 per cent uncertainty in ν_{max}, as just described, and with these, the luminosity can be determined with an accuracy of 1 per cent. This implies that the distance to the source can also be constrained to within 1 per cent errors.

The technique may have astrophysical applications. Type-I X-ray bursts with photospheric radius expansion have been treated as standard candles to evaluate distances to globular clusters containing these X-ray bursters with uncertainties on the level of 30 per cent (Kuulkers et al. 2003). Measurements of LMXBs in quiescence seem to be more precise, with errors less than 10 per cent (Guillot et al. 2013; Steiner et al. 2018). With our model, if it is successfully applied to X-ray bursters, we could place much more stringent
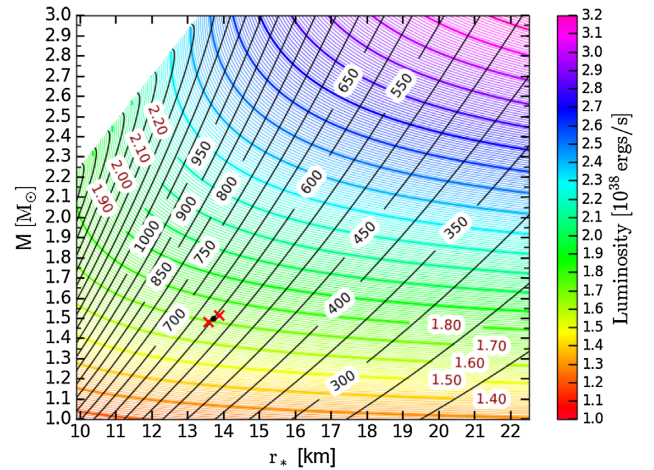
Figure 11. A grid of luminosity and frequency maximum contours computed from a wide range of masses and radii. The coloured downward sloping contours represent luminosity (in 10^{38} erg s^{-1} units) plotted in steps of 0.1, and the black quasi-diagonal lines represent the frequency maximum contours plotted for every 50 Hz. The errors on mass and radius determined in Section 5 correspond to the interval (close to the 600 Hz line) marked by the red crosses.

constraints on the distances to these globular clusters. For clusters such as 47 Tuc, where the distance has been estimated accurately through other methods (Woodley et al. 2012), one would get a valuable cross-check on the validity of our approach.

6 FURTHER DISCUSSION

We have derived the modes of oscillation of an atmosphere suspended above the neutron star surface by the force of radiation. Although the fundamental mode is critically damped due to radiation drag, the higher oscillatory modes of optically thin atmospheres may be detected by future X-ray missions. We have shown that

with the knowledge of the frequency and the corresponding near-Eddington luminosity from the X-ray observations, the mass and radius of the neutron star can be derived. It would be interesting to check the applicability of this method with the currently available X-ray data, to compare with the already available estimates of the neutron star mass and radius.

Recent works on constraining the mass and radius of neutron stars rely on X-ray spectroscopy of the thermal emission from the hot neutron stars residing in quiescent LMXBs. An analysis of LXMB sources in the Galactic plane gave mass and radius constraints on two sources with respective errors at 90 per cent confidence level between 30 per cent and 50 per cent (Marino et al. 2018), and comparable, or even higher, errors for several globular cluster sources (Steiner et al. 2018). These error estimates assume a precisely known distance, the errors further increase when accounting for distance uncertainties. For quiescent LMXB X7 in the globular cluster 47 Tuc, the distance to which is known accurately, Bogdanov et al. (2016) obtains a 7 per cent error in the radius, assuming a particular value for the neutron star mass. Our method, which is described in Section 4, is potentially much more accurate (and yields both, the mass and radius), but for uncertain distances it yields errors as large as those of the distance determination. However, we note that the slope (in the mass–radius diagram) of the confidence level contours differs between the methods. The spectral technique employed to various LMXB sources in globular clusters yields mass and radius constraints with probabilities shifting towards larger radii for lower masses in most of the sources (Steiner et al. 2018). This picture when overlapped with Fig. 7 of this paper in which the probabilities shift towards larger radii for larger masses can further narrow down the limits on mass and radius. Thus in an overall comparison, burst oscillation study can be a very useful technique to constrain the mass and radius with a high accuracy.

As we showed in Section 5, if the oscillation is detected over a sufficiently wide range of X-ray fluxes, the distance to the source may be directly determined by comparing observations with the theoretical frequency–flux curves. In such a case, the mass and radius, as well as the distance, could be determined to high accuracy with no reference to the spectral method.

Apart from the oscillations and their relevance to the observed frequencies, the levitating atmosphere may have its own observational signatures. A study by Rogers (2017) suggests that such levitating atmospheres can deflect the light rays coming from the central compact source and this can significantly affect the appearance of the central object in the observations.

Similar atmospheres are found in the corona of accretion discs and described as photon floaters, formed at the critical height where the radiation force from the disc is balanced by the gravitational force of the central object (Fukue 1996). It would be interesting to see if similar oscillations persist in the disc corona. Under the plane-parallel approximation, the eigenfunctions of these atmospheric oscillations may remain the same as for the spherically symmetric geometry presented here, while the frequencies of such oscillations would be different.

So-called burst oscillation frequencies are detected during the Type I X-ray bursts. If these are identified with the actual oscillations of an optically thin atmosphere, the methods described in this paper can be directly applied to the X-ray burst frequencies in order to determine the neutron star mass and radius. However, the radiating surface in X-ray bursters is optically thick and throughout this work we have assumed an optically thin fluid. The construction of optically thick atmospheres was given by Wielgus et al. (2016) and the procedure involved numerical methods. So an analytical analysis

of the oscillation modes in such a case is non-viable and their analysis is beyond the scope of this paper. Clearly, they are of great astrophysical interest and could possibly be subject to less radiation drag since radiation transport inside the optically thick atmosphere is due to diffusion. It is hoped that future work will treat the oscillations of the optically thick levitating atmospheres, especially in the context of radius expansion X-ray bursts. Regardless of this, future instruments with high time resolution and good sensitivity to higher energy photons, such as *STROBE-X* (Ray et al. 2019) and *eXTP* (Zhang et al. 2016), may detect optically thin atmospheres, and their oscillations, outside Eddington luminosity neutron stars.

7 CONCLUSION

Neutron stars with super-Eddington luminosity have a strong radiation field close to the stellar surface that dominates over gravity. The strong radiation force pushes the surrounding matter away from the stellar surface to a certain critical radius r_0, beyond which gravity prevails, thereby forming an atmospheric shell at r_0 that levitates above the stellar surface. These levitating atmospheres are thus supported by the strong radiation flux from the stellar surface. The same flux is a source of strong radiation drag that eventually damps any oscillations of the atmosphere.

In this paper, we analytically study in general relativity the oscillations of levitating atmospheres that are optically and geometrically thin, including the radiative terms in the perturbation equation. Radiation drag induces damping of oscillations in all regimes and we find that the damping coefficient is independent of the mode number. Radiation drag prevents oscillations only for the first mode, while higher modes are underdamped. The frequency range observed for the burst oscillations in the decay phase of the X-ray bursts is 300–600 Hz, which lies within the obtained frequencies of the damped oscillations. The frequency of these oscillations increasing with decreasing luminosity is in qualitative agreement with the observations for the oscillations in the decay phase of the X-ray burst where luminosity decreases with time.

The frequency of these oscillations exhibits a characteristic maximum that is more pronounced for the lower order modes. Noting that the frequency is only dependent on the stellar luminosity, mass, and radius, we compute the mass and radius as a function of the maximum frequency, and luminosity. However, the accuracy of this method is limited by the uncertainties in distance to the source, typically of $\sim$10 per cent, which lead to a comparative relative error on mass and radius estimates.

An alternative method to determine the stellar parameters is also proposed, which does not rely on prior knowledge of the distance. This method focuses on the variation of the two directly observable quantities with respect to each other, i.e. the frequency variation with the flux. We show that with this method, the stellar parameters could be estimated as accurately as the frequencies are measured, i.e. to $\sim$1 per cent should such oscillations be observed over a sufficiently wide range of frequencies. The new constraints on the mass and radius when combined with the knowledge of the frequency maximum allow us to also directly infer the luminosity of the source with an accuracy of < 1 per cent. Therefore, the distance can also be constrained to within a 1 per cent error, by comparing the inferred luminosity with the measured flux. This model thus potentially establishes a new way to determine, with exceptionally high accuracy, the distance to the neutron star, and its mass and radius.

ACKNOWLEDGEMENTS

REFERENCES

Abarca D., Kluźniak W., 2016, MNRAS, 461, 3233
Abramowicz M. A., Ellis G. F. R., Lanza A., 1990, ApJ, 361, 470
Abramowicz M. A., Blaes O. M., Horák J., Kluzniak W., Rebusco P., 2006, Class. Quantum Gravity, 23, 1689
Arnett W. D., Bowers R. L., 1977, ApJS, 33, 415
Bachetti M. et al., 2014, Nature, 514, 202
Bini D., Jantzen R. T., Stella L., 2009, Class. Quantum Gravity, 26, 055009
Blaes O. M., Arras P., Fragile P. C., 2006, MNRAS, 369, 1235
Bogdanov S., Heinke C. O., Özel F., Güver T., 2016, ApJ, 831, 184
Bollimpalli D. A., Kluźniak W., 2017, MNRAS, 472, 3298
Brown E. F., Bildsten L., Rutledge R. E., 1998, ApJ, 504, L95
Carpano S., Haberl F., Maitra C., Vasilopoulos G., 2018, MNRAS, 476, L45
Chakrabarty D., Morgan E. H., Muno M. P., Galloway D. K., Wijnands R., van der Klis M., Markwardt C. B., 2003, Nature, 424, 42
Chamel N., Haensel P., 2008, Living Rev. Relativ., 11, 10
Charles P., 2011, in Schmidtobreick L., Schreiber M. R., Tappert C., eds, ASP Conf. Ser. Vol. 447, Evolution of Compact Binaries. Astron. Soc. Pac., San Francisco, p. 19
Coe M. J., Burnell S. J. B., Engel A. R., Evans A. J., Quenby J. J., 1981, MNRAS, 197, 247
Cook G. B., Shapiro S. L., Teukolsky S. A., 1994, ApJ, 424, 823
Cooperstein J., 1988, Phys. Rev. C, 37, 786
Damen E., Magnier E., Lewin W. H. G., Tan J., Penninx W., van Paradijs J., 1990, A&A, 237, 103
Ebisuzaki T., 1987, PASJ, 39, 287
Fukue J., 1996, PASJ, 48, 89
Galloway D. K., Muno M. P., Hartman J. M., Psaltis D., Chakrabarty D., 2008, ApJS, 179, 360
Guillot S., Servillat M., Webb N. A., Rutledge R. E., 2013, ApJ, 772, 7
Hulse R. A., Taylor J. H., 1975, ApJ, 195, L51
Inogamov N. A., Sunyaev R. A., 1999, Astron. Lett., 25, 269
Ipser J. R., Lindblom L., 1992, ApJ, 389, 392
Israel G. L. et al., 2017a, Science, 355, 817
Israel G. L. et al., 2017b, MNRAS, 466, L48
Koornwinder T. H., Wong R., Koekoek R., Swarttouw R. F., 2010, in Olver F. W. J., Lozier D. W., Boisvert R. F., Clark C. W., eds, NIST Handbook of Mathematical Functions, Chapt. 18. Cambridge Univ. Press, Oxford, p. 435

Kuulkers E., den Hartog P. R., in't Zand J. J. M., Verbunt F. W. M., Harris W. E., Cocchi M., 2003, A&A, 399, 663
Lattimer J. M., 2012, Ann. Rev. Nucl. Part. Sci., 62, 485
Lewin W. H. G., Vacca W. D., Basinska E. M., 1984, ApJ, 277, L57
Lewin W. H. G., van Paradijs J., Taam R. E., 1993, Space Sci. Rev., 62, 223
Marino A., Degenaar N., Di Salvo T., Wijnands R., Burderi L., Iaria R., 2018, MNRAS, 479, 3634
Mihalas D., Mihalas B. W., 1984, Foundations of Radiation Hydrodynamics. Oxford Univ. Press, Oxford
Muno M. P., Chakrabarty D., Galloway D. K., Savov P., 2001, ApJ, 553, L157
Nättilä J., Steiner A. W., Kajava J. J. E., Suleimanov V. F., Poutanen J., 2016, A&A, 591, A25
Özel F., Freire P., 2016, ARA&A, 54, 401
Ray P. S. et al., 2019, preprint (arXiv:1903.03035)
Rhoades C. E., Ruffini R., 1974, Phys. Rev. Lett., 32, 324
Rogers A., 2017, Universe, 3, 3
Sazonov S. Y., Sunyaev R. A., Lund N., 1997, in Meyer-Hofmeister E., Spruit H., eds, Lecture Notes in Physics, Berlin Springer Verlag Vol. 487, Accretion Disks – New Aspects. Springer, Berlin, Heidelberg, p. 199
Skinner G. K., Bedford D. K., Elsner R. F., Leahy D., Weisskopf M. C., Grindlay J., 1982, Nature, 297, 568
Sok Oh J., Kim H., Mok Lee H., 2011, New Astron., 16, 183
Stahl A., Wielgus M., Abramowicz M., Kluźniak W., Yu W., 2012, A&A, 546, A54
Stahl A., Kluźniak W., Wielgus M., Abramowicz M., 2013, A&A, 555, A114
Steiner A. W., Heinke C. O., Bogdanov S., Li C. K., Ho W. C. G., Bahramian A., Han S., 2018, MNRAS, 476, 421
Strohmayer T., Bildsten L., 2006, in Lewin W., van der Klis M., eds, Compact Stellar X-ray Sources. Cambridge Univ. Press, Cambridge, p. 113
Strohmayer T. E., Markwardt C. B., 2002, ApJ, 577, 337
Strohmayer T. E., Zhang W., Swank J. H., Smale A., Titarchuk L., Day C., Lee U., 1996, ApJ, 469, L9
Tawara Y. et al., 1984, ApJ, 276, L41
van Paradijs J., Lewin W. H. G., 1987, A&A, 172, L20
Watts A. L., 2012, ARA&A, 50, 609
Wielgus M., Stahl A., Abramowicz M., Kluźniak W., 2012, A&A, 545, A123
Wielgus M., Kluźniak W., Sądowski A., Narayan R., Abramowicz M., 2015, MNRAS, 454, 3766
Wielgus M., Sądowski A., Kluźniak W., Abramowicz M., Narayan R., 2016, MNRAS, 458, 3420
Woodley K. A. et al., 2012, AJ, 143, 50
Zhang S. N. et al., 2016, Proc. SPIE, 9905, 99051Q

This paper has been typeset from a TEX/LATEX file prepared by the author.

Part IV

Variability in Black holes: Broad-band variability

Chapter 5

Paper IV: Looking for the underlying cause of black hole X-ray variability in GRMHD simulations

Looking for the underlying cause of black hole X-ray variability in GRMHD simulations

D. A. Bollimpalli [1,2]★ R. Mahmoud [3] C. Done,[3] P. C. Fragile [2,4] W. Kluźniak,[1]
R. Narayan[5] and C. J. White[4]

[1]*Nicolaus Copernicus Astronomical Center, Polish Academy of Sciences, ul. Bartycka 18, PL-00-716 Warsaw, Poland*
[2]*Department of Physics and Astronomy, College of Charleston, Charleston, SC 29424, USA*
[3]*Department of Physics, University of Durham, South Road, Durham DH1 3LE, UK*
[4]*Kavli Institute for Theoretical Physics, Kohn Hall, University of California, Santa Barbara, CA 93107, USA*
[5]*Harvard-Smithsonian Center for Astrophysics, 60 Garden Street, Cambridge, MA 02138, USA*

ABSTRACT

Long-term observations have shown that black hole X-ray binaries exhibit strong, aperiodic variability on time-scales of a few milliseconds to seconds. The observed light curves display various characteristic features like a lognormal distribution of flux and a linear rms–flux relation, which indicate that the underlying variability process is stochastic in nature. It is also thought to be intrinsic to accretion. This variability has been modelled as inward propagating fluctuations of mass accretion rate, although the physical process driving the fluctuations remains puzzling. In this work, we analyse five exceptionally long-duration general relativistic magnetohydrodynamic (GRMHD) simulations of optically thin, geometrically thick, black hole accretion flows to look for hints of propagating fluctuations in the simulation data. We find that the accretion profiles from these simulations do show evidence for inward propagating fluctuations below the viscous frequency by featuring strong radial coherence and positive time lags when comparing smaller to larger radii, although these time lags are generally shorter than the viscous time-scale and are frequency-independent. Our simulations also support the notion that the fluctuations in $\dot{M}$ build up in a multiplicative manner, as the simulations exhibit linear rms–mass flux relations, as well as lognormal distributions of their mass fluxes. When combining the mass fluxes from the simulations with an assumed emissivity profile, we additionally find broad agreement with observed power spectra and time lags, including a recovery of the frequency dependency of the time lags.

Key words: accretion, accretion discs – MHD – methods: numerical – X-rays: binaries.

1 INTRODUCTION

A large fraction of the galactic black hole X-ray binaries (BHXRBs, e.g. GX 339–4, XTE J1550–64, and GRO J1655–40) are generically variable, both spectrally and temporally, as may be associated with changes to the geometry and nature of accretion flows. They occasionally undergo outbursts during which the luminosity varies by several orders of magnitude, and the X-ray spectral states evolve – a phenomena termed 'state transitions'. The two main spectral states seen in these systems are a high-luminosity, 'soft' state, dominated by thermal emission from the accretion disc, and a variable-luminosity, 'hard' state, dominated by a non-thermal Comptonized X-ray spectrum, with a weak or absent thermal component (see, e.g. the review by Done, Gierliński & Kubota 2007).

The X-ray light curves of BHXRBs, particularly in the hard state, are dominated by strong, aperiodic variability (flicker-type noise) on time-scales of milliseconds to seconds (van der Klis 1995). This manifests as a continuous band of power present over a wide range of frequencies in the power spectral densities (PSDs), which also change during the state transitions. The other important variability features reported in these systems are a linear rms–flux relation and lognormal distribution of flux, indicating that the underlying stochastic process could be non-linear and multiplicative in nature (Uttley & McHardy 2001; Uttley, McHardy & Vaughan 2005). Further hints on the origin of variability may be derived from the frequency-dependent time lags and strong coherence observed between different energy bands (Miyamoto & Kitamoto 1989; Nowak et al. 1999; McHardy et al. 2004). Similar variability features are observed to occur in active galactic nuclei

★ E-mail: deepika@camk.edu.pl

(AGN) on time-scales of hours to months (McHardy 1988; Gaskell 2004).

In addition to the black hole systems, broad-band variability is also observed in other accreting systems: neutron star systems (in X-rays) (Wijnands & van der Klis 1999), accreting white dwarfs (in optical/UV band) (Scaringi et al. 2013; Van de Sande, Scaringi & Knigge 2015), and young stellar objects (in IR/optical band; Scaringi et al. 2015). The remarkable similarity in the variability across different systems suggests that the underlying physical mechanism at work may be the same in all these systems.

Lyubarskii (1997) suggested a model where fluctuations of viscosity generated in the disc at different radii on viscous time-scales cause mass accretion rate ($\dot{M}$) fluctuations that propagate inwards by modulating subsequent fluctuations driven at smaller radii. Since the fluctuations couple together, this model readily explains multiple observed features: (a) The accretion rate, and thereby the emission flux from the inner regions, carries the imprints of fluctuations generated over a wide range of radii associated with a wide range of variability time-scales, thus producing a broad PSD; and (b) the high-frequency fluctuations presumed to be driven at smaller radii are modulated by the longer time-scale fluctuations coming from larger radii, thus giving rise to the rms–flux relation over all time-scales. Furthermore, this coupling through a multiplicative combination of fluctuations naturally leads to a lognormal distribution. The observed energy-dependent PSDs, where the higher photon-energy bands show relatively more high-frequency power than lower photon energy bands, can be explained by this model if the hard X-rays are produced from a concentrated region close to the central object and the soft X-rays come from an extended region further away. This basic picture also explains the strong coherence and time lags that appear between the different X-ray energy bands – as the fluctuations propagate inwards, they first appear in the softer energy bands and later in the harder energy bands (Kotov, Churazov & Gilfanov 2001; Mahmoud & Done 2018a). Additionally, outward propagating fluctuations from inner radii could potentially cause negative lags at higher frequencies, whether they are carried by waves (Mushtukov, Ingram & van der Klis 2018) or matter.[1] Since the accretion process carrying the fluctuations inwards is diffusive in nature, any fluctuations generated on time-scales shorter than the diffusion time-scales will be damped before they can reach the inner radii. Thus, to explain the observed high-amplitude, high-frequency variability power in the PSDs of BHXRBs may require the relatively short characteristic time-scales associated with geometrically thick, optically thin accretion flows (Churazov, Gilfanov & Revnivtsev 2001; Arévalo & Uttley 2006; Ingram & Done 2011; Mahmoud & Done 2018a).

Our general understanding of accretion discs is largely based on the concepts of Shakura & Sunyaev (1973), which describes geometrically thin and optically thick discs, emitting thermal blackbody-like radiation. However, that model was soon found to be incapable of producing the observed hard X-rays (∼100 keV) from Cygnus X-1 (Lightman & Shapiro 1975). Various models were invoked to explain the observed spectral properties through hot, optically thin, and geometrically thick flows at low luminosities, in the inner disc regions around the black hole (Thorne & Price 1975; Shapiro, Lightman & Eardley 1976), which were later modified to include advection to ensure thermal stability and became what is

known as advection-dominated accretion flows (ADAFs; Ichimaru 1977; Narayan & Yi 1995b). In these flows, the energy released through viscous dissipation is stored in the accreted matter and advected radially into the black hole (Narayan & Yi 1994). Thus, these flows are hot and radiatively inefficient, therefore sometimes are referred to as radiatively inefficient accretion flows (RIAFs). The typical temperatures in ADAFs are close to virial and thus have the potential to explain the observed hard spectra through inverse-Compton scattering by hot electrons. These flows are, however, susceptible to the convective instability, which can play a vital role in launching outflows (Narayan & Yi 1995a). Further studies have developed analytical solutions that treat convection as a dominant process in transporting angular momentum (Narayan, Igumenshchev & Abramowicz 2000; Quataert & Gruzinov 2000); such solutions are sometimes referred to as convection-dominated accretion flows (CDAFs). Disc winds could also carry away the angular momentum from the accretion flow, in which case the net advected energy on to the black hole is reduced (Blandford & Begelman 1999). It is now widely accepted that ADAFs can consistently account for the observations of a number of low-luminosity state BHXRBs and AGN, including Sgr A∗ (Rees et al. 1982; Narayan et al. 1998).

All these ADAF models (see e.g. Yuan & Narayan 2014) are self-similar analytic solutions derived primarily by assuming a constant α-viscosity parameter. However, real accretion discs are magnetized and thought to be subject to the magnetorotational instability (MRI; Balbus & Hawley 1991), which acts as a natural source of turbulence, mediating the outward transport of angular momentum, thus allowing for accretion.

Many numerical simulations of ADAFs have been performed so far in the interest of understanding the details of their flow dynamics and their observational relevance, yet the presence of aperiodic variability in these simulations remains relatively unexplored. Only recent MHD simulations of geometrically thin discs[2] have been examined in such a way Wellons et al. (2014), Hogg & Reynolds (2016).

In our work, we are motivated to search for aperiodic variability in ADAFs using GRMHD simulations for at least two main reasons: (a) the association of broad-band variability with hard X-ray flux in BHXRBs suggests they come from ADAF discs; and (b) the characteristic time-scales of standard, thin discs cannot explain the high-amplitude, high-frequency variability power in the PSDs of BHXRBs (Churazov et al. 2001). The GRMHD simulations analysed in this work are notable for their extremely long time duration, which makes it possible to probe a wider frequency range of broad-band variability. However, a drawback of the fast time-scales associated with ADAFs is that simulations of them can be particularly sensitive to the initial conditions used (White, Quataert & Gammie 2020); for this reason, we analyse simulations with different initial conditions, which can help discern the robustness of the propagating fluctuations in these flows.

Our paper is organized as follows. We provide brief descriptions of the simulations used in this analysis in Section 2. Since we use the mass accretion rate ($\dot{M}$) as a proxy for the luminosity, we describe our analysis of $\dot{M}$ in Section 3. In Section 4, we present our results in the form of power spectra, coherence plots, time lags, rms–$\dot{M}$ relations, and $\dot{M}$ distributions. In Section 5, we compare our results with observations and conclude in Section 6.

---

[1]The velocity field in three-dimensional discs is non-trivial and even thin α-discs are known to exhibit backflows (Urpin 1984; Kluzniak & Kita 2000; Regev & Gitelman 2002; Philippov & Rafikov 2017)

[2]These discs are thought to be more relevant to X-ray binaries in the high/soft state, white dwarfs systems, and young stellar objects.

Table 1. Parameters of the simulations considered for analysis in this paper.

Simulation	a_*	r_{max} (r_g)	r_{in} (r_g)	Γ	B field (number of loops)	Run length (r_g/c)	Dump interval (r_g/c)
A	0	52	25.0	4/3	$N_r = 6, N_\theta = 4$	440 000	100 (1)[a]
B	0	52	25.0	4/3	$N_r = 6, N_\theta = 1$	220 000	100
C	0	52	25.1	5/3	$N_r = 6, N_\theta = 4$	220 000	100
R	0	19.2	10.0	5/3	$N_r = 8, N_\theta = 1$	200 000	10
D	0.5	40	22.0	4/3	$N_r = 1, N_\theta = 1$	63 000	100

[a]For this particular simulation, we also have the high-cadence data with dumping interval equal to $1\,GM/c^3$ for variables at a few predetermined radii

2 DESCRIPTION OF SIMULATIONS

We analyse the accretion rate data from five different simulations of ADAFs, which were initiated using different initial conditions and were performed using different GRMHD codes. While we performed simulation D in the interest of this work, simulations A, B, and C were taken from White et al. (2020), while simulation R comes from Narayan et al. (2012). In this section, we briefly describe the numerical set-ups of each simulation and discuss their key differences. For more details of simulations A, B, C, and R, we refer the reader to the original papers.

First, we describe the similarities between the simulations before we delve into the differences. All five simulations are non-radiative, which allows us to scale our results to any required black hole mass. However, this implies that we do not have a direct estimation of luminosity from the simulations, limiting us to use the mass accretion rate as a proxy for luminosity/flux. All the simulations are initiated from a rotating, hydrostatic equilibrium torus of matter governed by gravity, pressure, and centrifugal forces. The mass of the torus is assumed negligible compared to the mass of the black hole so that the gravity is fixed by the black hole space–time. Each torus is threaded with weak magnetic fields that are susceptible to the MRI (Balbus & Hawley 1991). Once the simulations start, the MRI grows and produces turbulence, which is responsible for transporting angular momentum outwards, allowing matter to accrete inwards. Thus, the inner region of the torus turns into an accretion flow while the outer region acts as a matter reservoir, feeding the accretion flow throughout the simulation. Below, we provide details of the equilibrium torus solutions and the magnetic field configurations used for the initial set-up of each simulation. Key simulation parameters are summarized in Table 1.

2.1 Simulations A, B, and C

These simulations are performed using the GRMHD code, ATHENA++ (White, Stone & Gammie 2016; Stone et al. 2020). They are initialized using the torus solution of Fishbone & Moncrief (1976), in which $u_\phi u^t$ (in Boyer Lindquist coordinates) is constant. The torus has a pressure maximum located at $r_{max} = 52\,r_g$, where $r_g = GM/c^2$ is the gravitational radius. The peak density at r_{max} is normalized to 1. Simulation A is run for the longest time period, up to $t = 4.4 \times 10^5\,GM/c^3$, while the variants of this simulation – B and C – are run up to $t = 2.2 \times 10^5\,GM/c^3$. For A and B, the inner edge of the torus is set at $r_{in} = 25\,r_g$, while for C, $r_{in} = 25.1\,r_g$. A polytropic equation of state is used in each case, with an adiabatic index of $\Gamma = 4/3$ for simulations A and B and $\Gamma = 5/3$ for simulation C. The initial magnetic field is chosen to be purely poloidal with the number of alternating polarity loops set along the radial and polar directions, N_r and N_θ, different for each simulation. For simulations A and C, $N_r = 6$ and $N_\theta = 4$, while for simulation B, $N_r = 6$ and N_θ

= 1. Using the alternating poloidal loops prevents the accumulation of large net magnetic flux in the accretion flow.

These simulations are evolved in the space–time of a non-spinning black hole ($a_* = Jc/GM^2 = 0$) using spherical Kerr–Schild coordinates. Grid cells are logarithmically spaced in the radial direction extending from $r = 1.7$ to $10^4\,r_g$ and compressed towards the equator in the polar direction to increase the resolution close to the symmetry plane of the disc. The base grid, covering the entire sphere, consists of $120 \times 20 \times 20$ cells in the radial, polar, and azimuthal directions with an additional one level refinement introduced in the region $\theta \in (\pi/5, 4\pi/5)$ and another level of refinement on top of that in the region $\theta \in (3\pi/10, 7\pi/10)$.

The key finding of these simulations is that the resulting flow structure of ADAFs is sensitive to the initial conditions. The larger magnetic field loops in simulation B build up a coherent vertical flux that drives polar outflows. For the same reason, simulation B attains a 'semi-MAD' (magnetically arrested disc) state with the magnetic flux on the horizon reaching a limiting value for a brief period. Simulations A and C, on the other hand, exhibit polar inflows and equatorial backflows, which cannot be explained by convective stability/meridional circulation. Just the difference in Γ causes a much more spherical distribution of mass in simulation C compared to simulations A and B that present a more standard disc picture, with high density near the equatorial region and low density close to the polar region. Further details of these simulations are provided in White et al. (2020).

2.2 Simulation R

This simulation is performed using the 3D GRMHD code, HARM (Gammie, McKinney & Tóth 2003; McKinney 2006; McKinney & Blandford 2009). The simulation is set up using a torus solution similar to the Polish doughnut (Penna, Kulkarni & Narayan 2013), for which $r_{in} = 10\,r_g$ and the outer radius is $1000\,r_g$. The pressure maximum is located around $19.21\,r_g$. The angular momentum in the torus ($-u_\phi/u_t$) is constant within $42\,r_g$; beyond this radius, it is set to 71 percent of the Keplerian value. A polytropic equation of state is used with $\Gamma = 5/3$. The initial magnetic field is purely poloidal with eight centres of poloidal loops with alternating polarity set along the radial direction ($N_r = 8, N_\theta = 1$).

This simulation is also evolved in the space–time of a non-spinning black hole ($a_* = 0$) using spherical Kerr–Schild coordinates. Grid cells are logarithmically spaced at smaller radii and hyperlogarithmically at the larger radii. Grid cells along the polar direction are non-uniformly spaced so as to increase the resolution close to both the equatorial region and the poles. This simulation uses a grid of $256 \times 128 \times 64$ cells in the radial, polar, and azimuthal directions without any additional refinement.

Simulation R never reaches a MAD state even though the initial magnetic field configuration is similar to simulation B. This
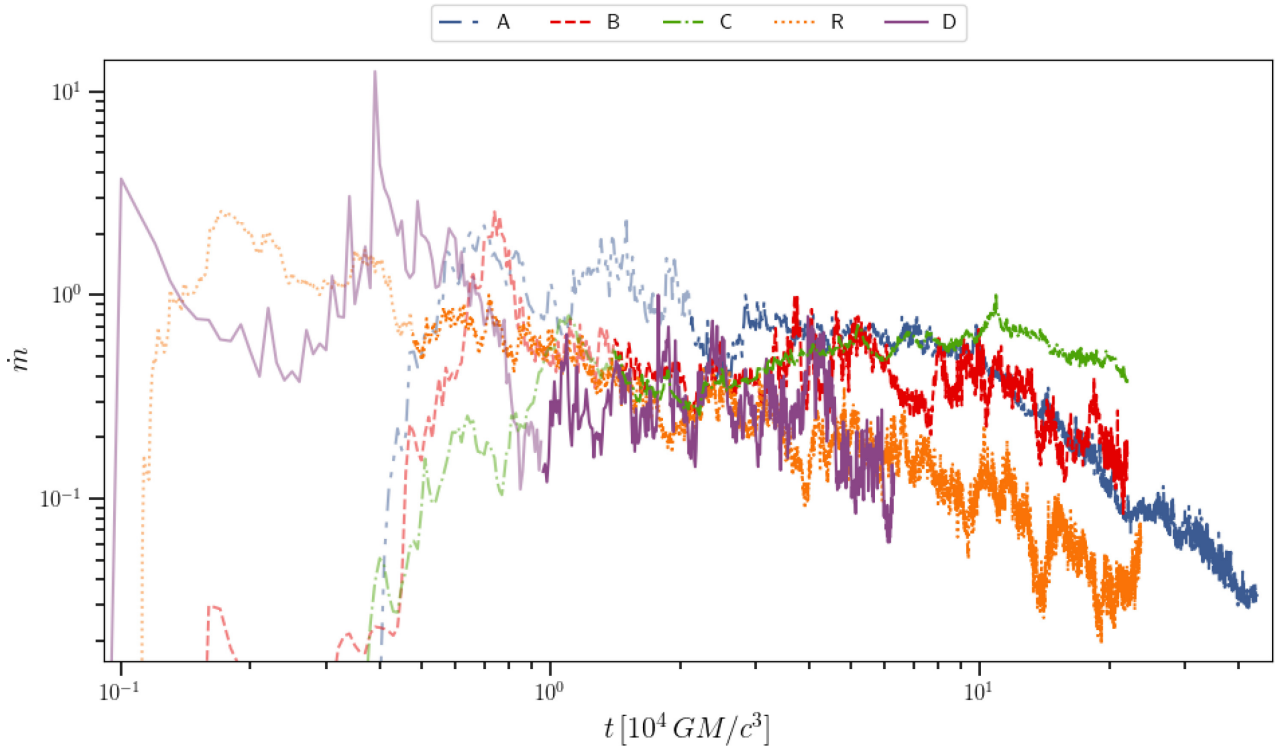
Figure 1. Profiles of the normalized accretion rate, $\dot{m}$, through the black hole horizon for all five simulations. Discarded data for simulations B, C, and D (first six $P_{\rm orb}$) and simulations A and R (first nine $P_{\rm orb}$) are shown in lighter shades.

simulation is convectively stable. Further details of this simulation are provided in Narayan et al. (2012).

2.3 Simulation D

This simulation is performed using the 3D GRMHD code, COSMOS++ (Anninos, Fragile & Salmonson 2005; Fragile et al. 2012; Fragile, Olejar & Anninos 2014). The simulation is set up following the torus solution given by Chakrabarti (1985), for which we set $r_{\rm in} = 22\,r_{\rm g}$ and $r_{\rm max} = 40\,r_{\rm g}$. The angular momentum inside the torus follows a power-law distribution in radius. The torus is threaded with a single poloidal magnetic field loop. The simulation is evolved in the space–time of a spinning black hole with $a_* = 0.5$ using spherical Kerr–Schild coordinates. A polytropic equation of state is used with $\Gamma = 4/3$. This simulation uses a grid of $192 \times 128 \times 32$ cells in the radial, polar, and azimuthal directions without any additional refinement. For more details on this simulation, see Appendix A.

3 ACCRETION RATE

The mass accretion rate, $\dot{M}$, at a given radius and time is computed by integrating the mass flux over a spherical shell:

$$\dot{M}(r, t) = -\iint \rho u^r \sqrt{-g}\,{\rm d}\theta\,{\rm d}\phi \, , \tag{1}$$

where ρ is the rest mass density, u^r is radial four-velocity, and the negative sign is included to make $\dot{M}$ positive when matter is flowing inwards towards the black hole. We calculate this expression in spherical Kerr–Schild coordinates. In our analysis, we discard the initial six orbital periods ($P_{\rm orb}$) of simulation data for simulations B, C, and D and nine orbital periods for simulations A and R, where $P_{\rm orb}$ is measured at $r_{\rm max}$. $\dot{M}$ for each simulation is then re-normalized

by its maximum value outside the discarded initial transient phase. In the rest of this paper, we report the normalized accretion rate, $\dot{m} = \dot{M}/\max(\dot{M})|_{r_{\rm H}}$, where $r_{\rm H}$ is the horizon radius.

Fig. 1 shows the evolution of the accretion rate on to the black hole for all five simulations. The discarded data, corresponding to the initial transient phase of the simulations, are shown in lighter shade. Simulation C remains at a comparatively high accretion rates throughout, while simulations A and B show secular declines beyond $\approx 100\,000\,GM/c^3$, with the decrease in $\dot{m}$ nearly two orders of magnitude for simulation A. Simulation R, as well, shows a significant decline in $\dot{m}$, while no such decline is seen in simulation D, though this simulation is run for a shorter time period. This secular decline behaviour of $\dot{m}$ can be attributed to two principal causes: (a) The disc loses its mass through the horizon at a rate faster than it is supplied by the surrounding torus (see, e.g. fig. 6 in Narayan et al. 2012); and (b) since the torus mass is not replenished in any of the simulations, $\dot{m}$ must inevitably begin to decline at some point as the mass reservoir becomes drained.

Among the several models in the literature that try to explain X-ray variability, a common assumption is that the underlying process is stationary, i.e. the mean and variance of the time series do not change over time. However, this is not what we see in our $\dot{m}$ profiles, especially for simulations A and R, which are far from being stationary. Therefore, it may be worthwhile to try to correct for any secular behaviour seen in these simulations. Unfortunately, there is no foolproof method for doing so, and any procedure presents the risk of introducing artefacts into the data. Nevertheless, for purposes of comparison, we adapt the method of Reynolds & Miller (2009) to apply an exponential fit to $\dot{m}$. Since simulation D does not show much of a decline and simulation C instead shows an increase followed by a late decline, we present the corrected accretion rate ($\dot{m}_{\rm cor}$) profiles at $r_{\rm H}$ only for simulations A, B, and R in Fig. 2, while the raw rates from Fig. 1 are reproduced as dotted curves.
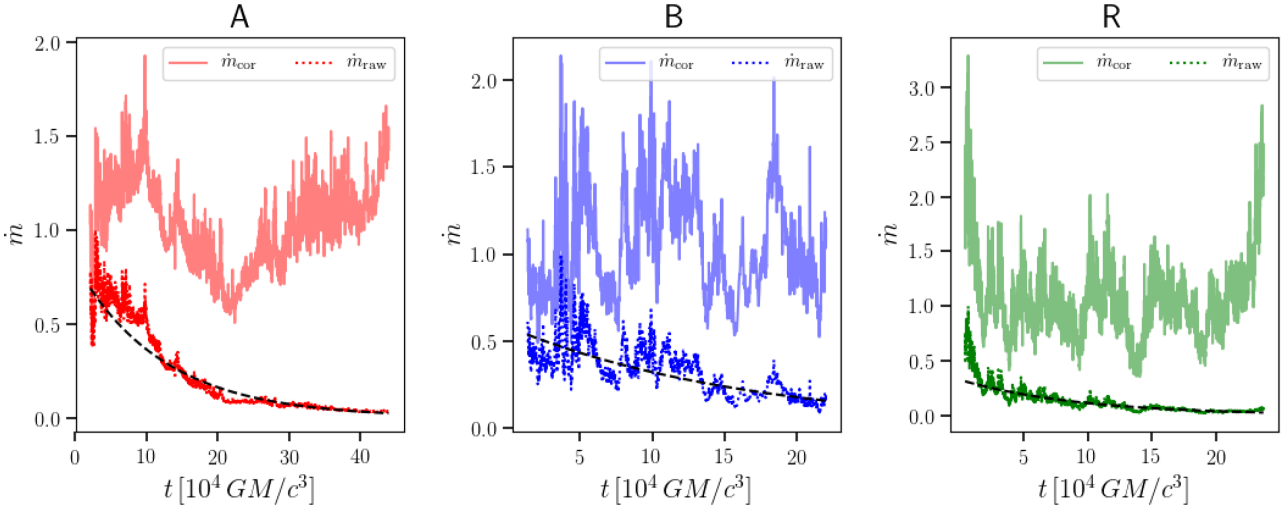
Figure 2. .Profiles of the mass accretion rates at r_H for simulations A (left-hand panel), B (middle panel), and R (right-hand panel), corrected for their secular declines ($\dot{m}_{cor}$). The original (uncorrected) data ($\dot{m}$) are shown as dotted curves, with the corresponding exponential fits overplotted as black dashed curves.

The exponential fit used in each case is shown as a black dashed curve. In the following subsections, we shall use these $\dot{m}_{cor}$ profiles to understand if a secular decline alters any of our results.

In Fig. 3, we show space–time plots of $\dot{m}$ for each simulation after $30P_{orb}$ over a window of $5P_{orb}$. Over this time window, the simulations are all in inflow equilibrium within $30 r_g$. Simulations A, B, and C show lower overall $\dot{m}$ during this period and lower variability. Simulation R shows an interesting chevron pattern, which indicates that there are $\dot{m}$ changes originating between $r = 10$ and $15 r_g$ that are then propagating inwards *and* outwards. Simulation D is distinguished by exhibiting the most small-scale variability.

4 RESULTS

4.1 Power spectra

We primarily use power spectra to look for traces of variability in these simulations. The power spectra are computed using the normalized $\dot{m}$ for each simulation following the steps presented in Uttley et al. (2014). At each radius, the time series data, i.e. the normalized accretion rate, are binned into a certain number of segments with the requirement that the number of time intervals per segment (N) be an integral power of 2. For each segment, a normalized periodogram, P, is computed as

$$P = \frac{2\Delta t}{\langle \dot{m} \rangle^2 N} |\widetilde{\dot{m}}(\nu)|^2 , \tag{2}$$

where $\widetilde{\dot{m}}(\nu)$ is the discrete Fourier transform of $\dot{m}$ (defined as in equation 1 of Uttley et al. 2014) and the angle brackets denote a time-average value. We compute P below the maximum frequency of $1/(2\Delta t)$ and above a minimum frequency given by the inverse of the segment length. Here Δt is the sampling time of the data, i.e. the dumping interval from the original simulation (provided in Table 1). The average of the periodograms obtained from all the segments yields the average PSD. To further reduce the noise, the resulting power spectrum from the previous procedure is re-binned logarithmically over frequencies and averaged over each frequency bin. This gives the normalized root mean square PSD, which is what we plot in all the power spectra figures. The frequencies in all the

power spectra are reported in Hz, assuming a unit solar mass black hole; therefore, by simply dividing by the mass in solar units, the frequencies for any other black hole mass can be extracted.

For all the space–frequency plots discussed in this section, we also plot three characteristic frequencies of disc dynamics: the Keplerian, radial epicyclic, and viscous frequencies. The viscous frequency (ν_{visc}) is simply computed as

$$\nu_{visc}(r) = \frac{\langle V^r(r,t) \rangle}{r} , \tag{3}$$

so it is directly related to the accretion time-scale, where V^r is the density-weighted, radial component of the three-velocity averaged over poloidal and azimuthal angles within one scale height of the mid-plane.

For all the simulations, we also extract the power spectra at 2, 10, and $20 r_g$. Of course, we certainly would not expect significant radiation to come from $r = 2r_g$, but as Fig. 3 shows, the mass flux is nearly uniform for all simulations at radii less than the innermost stable circular orbit (ISCO; at $4.23 r_g$ for simulation D and $6 r_g$ for the rest). This indifference to the presence of an ISCO is a common feature of ADAFs. Thus, the choice to consider $\dot{m}$ at radii below the ISCO should not adversely affect our variability analysis. For each of the resulting power spectra, we do a least-squares fitting with either a single power law, $P \propto \nu^\beta$, or a broken power law, with $P \propto \nu^{\beta_1}$ for $\nu < \nu_{break}$ (break frequency) and $P \propto \nu^{\beta_2}$ for $\nu > \nu_{break}$. In almost all cases, we find that the power spectra of 2 and $10 r_g$ are highly similar below the viscous frequency of $10 r_g$ and so we present the power-law fittings[3] to the averaged PSD of 2 and $10 r_g$.

4.1.1 Simulation A

Fig. 4 shows the power spectra of $\dot{m}$ from simulation A computed over a time window [38 900, 440 000] GM/c^3, during which inflow equilibrium is established out to $100 r_g$. Each segmented bin is of the length $0.13 (M/M_\odot)$ s. It is interesting to note the power

---

[3]Note that, although we plot $P\nu$ in the spectral plot, the respective power-law indices labelled in the plots correspond to the fitting made to P and not $P\nu$.
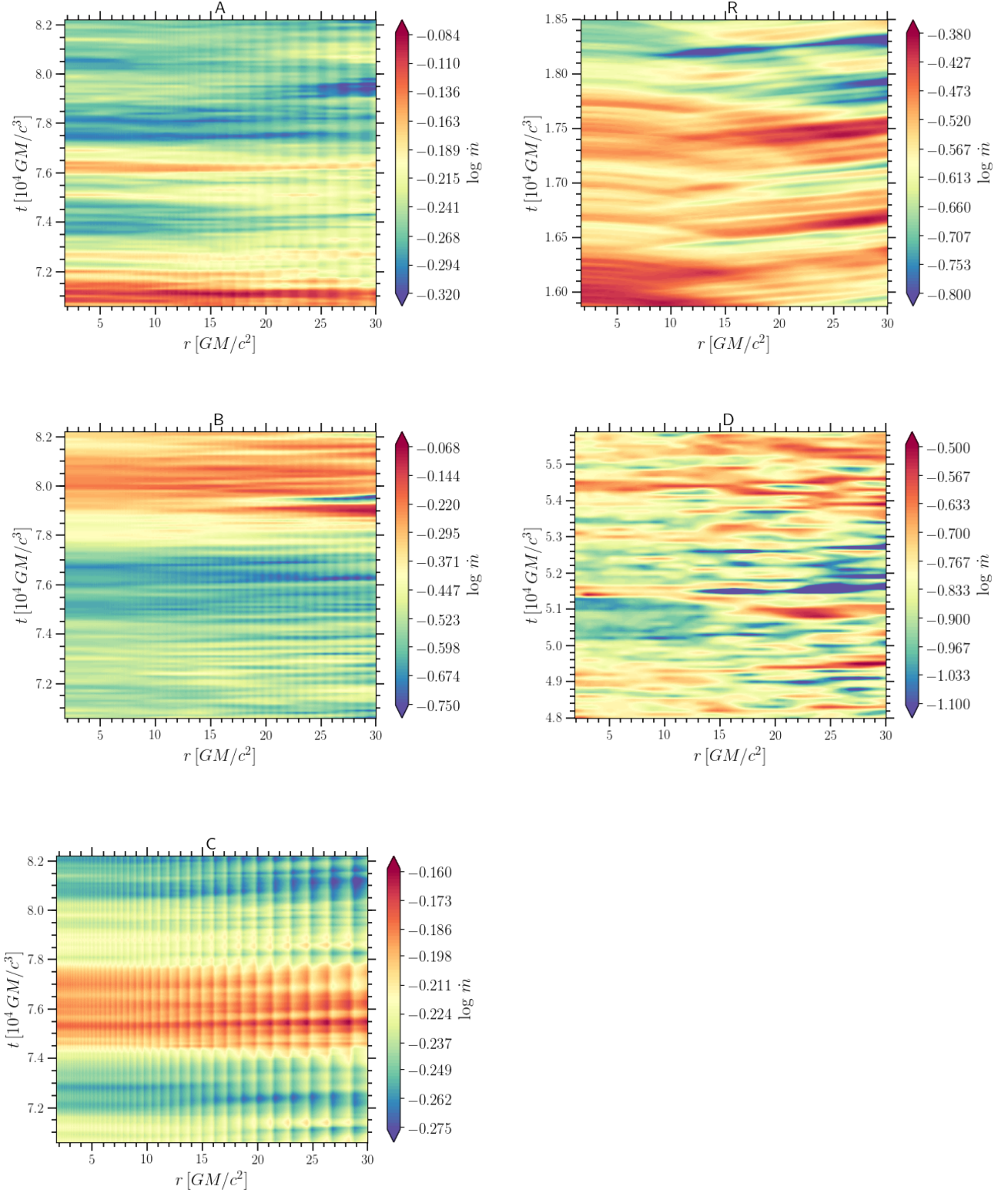
Figure 3. Space–time diagrams of $\dot{m}$ for all five simulations from $t = 30$ to 35 P_{orb}. Note that the colour scale is different for each panel. The faint vertical stripes seen in simulations A, B, and C are artefacts of extracting $\dot{m}$ over multiple refinement layers.

beyond the radial epicyclic frequency curve[4] and within the viscous

---

[4]Hereafter, by beyond the radial epicyclic curve, we mean at frequencies above the radial epicyclic curve for radii larger than where that curve peaks.

frequency curve. Between these curves, we find significantly less power. The power above the radial epicyclic frequency is possibly due to pressure waves, analogous to discoseismic p modes, which are likely non-dissipative and therefore will not contribute to the observed flux variations (Noble & Krolik 2009). Power below the
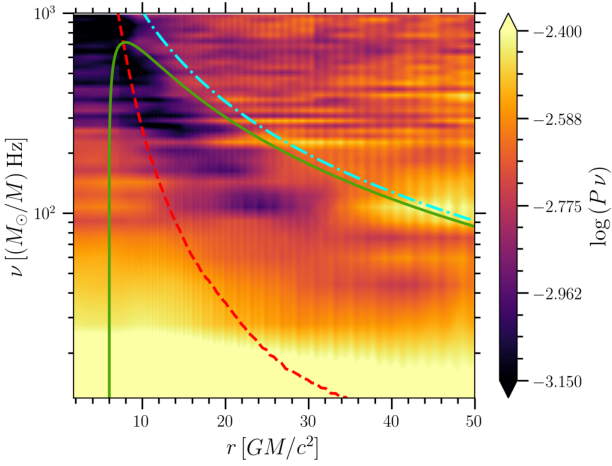
Figure 4. Normalized power spectra of $\dot{m}$ for simulation A computed for the time chunk $[38\,900, 440\,000]\,GM/c^3$, binned into segments of length $0.13\,(M/\mathrm{M}_\odot)$ s. The blue dash–dotted, solid green, and red dashed curves show the Keplerian, radial epicyclic, and viscous frequencies, respectively.

viscous frequency is likely due to propagating fluctuations. More evidence for the second statement will be provided in the later subsections when we discuss radial coherence and time lags. Below the epicyclic curve, as the frequency increases, the power drops and reaches a broad minimum at a factor of a few below the Keplerian frequency. This is not a true break in the power spectrum, as the power recovers at larger frequencies. However, it is interesting to note that in the case of geometrically thin discs, a break frequency has been predicted to correspond to the dynamo time-scale (King et al. 2004), which is a few times the Keplerian time-scale. This was later confirmed by the simulations of Hogg & Reynolds (2016) and may be related to what we are seeing here. A similar break, happening below the local Keplerian frequency, has recently been inferred from X-ray pulsar data (Mushtukov et al. 2019).

Since $\dot{m}$ does not vary noticeably across the ISCO, as pointed out in the previous section, it is not surprising that the power spectra

here and in subsequent sections also do not bear any signature of it. This in contrast with thin disc simulations, where the nature of the variability changes dramatically at the ISCO (Reynolds & Miller 2009; Mishra, Kluźniak & Fragile 2019).

In the left-hand panel of Fig. 5, we extract the power spectra at radii $r = 2$, 10, and $20\,r_\mathrm{g}$, shown as blue, orange, and green solid curves with decreasing line thickness, respectively. The chosen bin length is close to $0.16\,(M/\mathrm{M}_\odot)$ s. For both the plots in Fig. 5, we use the high-cadence data with $\Delta t = 1\,GM/c^3$, which is available only for simulation A and only for radii $r = 2, 5, 10$, and $20\,r_\mathrm{g}$. The PSDs are well fit by a broken power law with an index close to -1.55 for low frequencies, and an index ~ -2.57 for high frequencies. The break occurs at around $10^3\,(\mathrm{M}_\odot/M)$ Hz, which happens to be where Fig. 4 cuts off. The low-frequency slope is slightly steeper than flicker-type noise (index ≈ -1), and the high-frequency slope is slightly steeper than red-noise behaviour (index ≈ -2).

If we study Fig. 5 closely, we see that the spectrum at each radius shows strong correlation with the spectra of smaller radii below the local viscous frequency. For example, the curves of power spectra at 2, 10, and $20\,r_\mathrm{g}$ are virtually the same below the dashed line corresponding to the viscous frequency at $20\,r_\mathrm{g}$. Similarly, the PSD amplitudes of 2 and $10\,r_\mathrm{g}$ are nearly identical below the dashed line showing the viscous frequency at $10\,r_\mathrm{g}$. This seems to disagree with the assumption of the propagating fluctuations model that each independent annulus produces fluctuations with most of the variability power centred at the local viscous frequency. Moreover, it rules out the damping of propagating fluctuations (Arévalo & Uttley 2006; Rapisarda, Ingram & van der Klis 2017; Mahmoud & Done 2018b). Fig. 5 also shows that the break frequencies of the spectra do not correspond directly to any of the characteristic frequencies we consider, but do lie close to the local Keplerian frequencies.

Since the observed flux is usually an integration of the emission from a range of disc radii, we compute the average of the PSD at radii 2, 5, 10, and $20\,r_\mathrm{g}$, shown as the thin red curve in the right-hand panel of Fig. 5. The broken power-law fits are shown in thin red dash–dotted and dotted lines, respectively. We
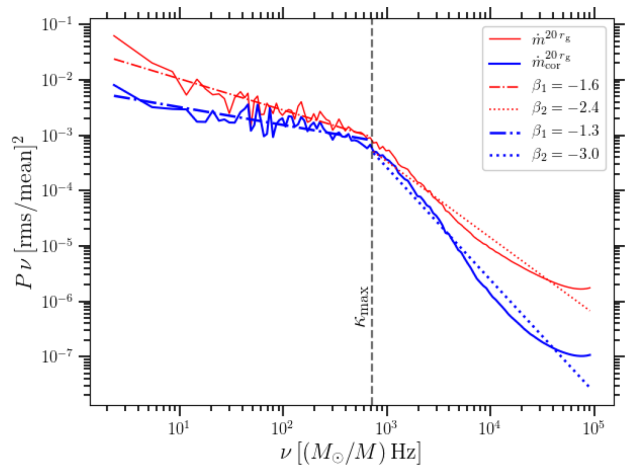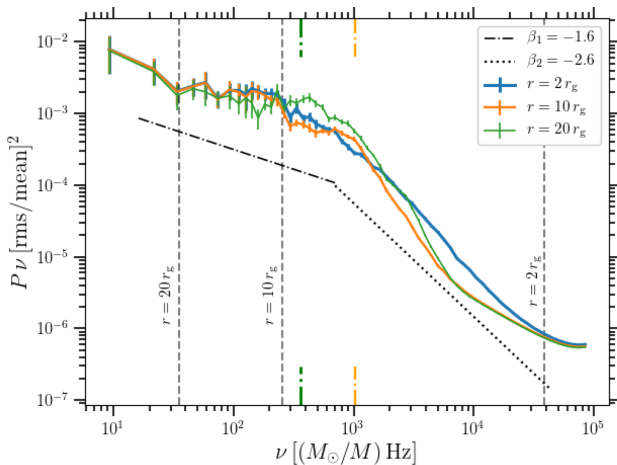
Figure 5. Normalized power spectra of $\dot{m}$ for simulation A at selected radii using the high-cadence data ($\Delta t = 1\,GM/c^3$) over a time window of $[38\,900, 440\,000]\,GM/c^3$. Left-hand panel: PSDs for radii $r = 2$, 10, and $20\,r_\mathrm{g}$ computed using bins of size $0.16\,(M/\mathrm{M}_\odot)$ s, shown in blue, orange and green curves, respectively, with decreasing line thickness. The average slopes of the broken power-law fittings to all three curves are indicated with black dash–dotted and dotted lines. The Keplerian frequencies for 10 and $20\,r_\mathrm{g}$ are marked near the x-axes in thin orange and thick green dash–dotted lines, respectively. The viscous frequencies for all three radii are shown as vertical dashed lines. Right-hand panel: average of the normalized PSDs for radii 2, 5, 10, and $20\,r_\mathrm{g}$ using longer bins of length $0.65\,(M/\mathrm{M}_\odot)$ s shown in thin red and thick blue curves for the original $\dot{m}$ and corrected $\dot{m}_{\mathrm{cor}}$ data. The respective broken power-law fittings are shown in dash–dotted and dotted lines. The vertical dashed line shows the maximum of the radial epicyclic frequency, which occurs at $8\,r_\mathrm{g}$.

Variability in GRMHD simulations 3815
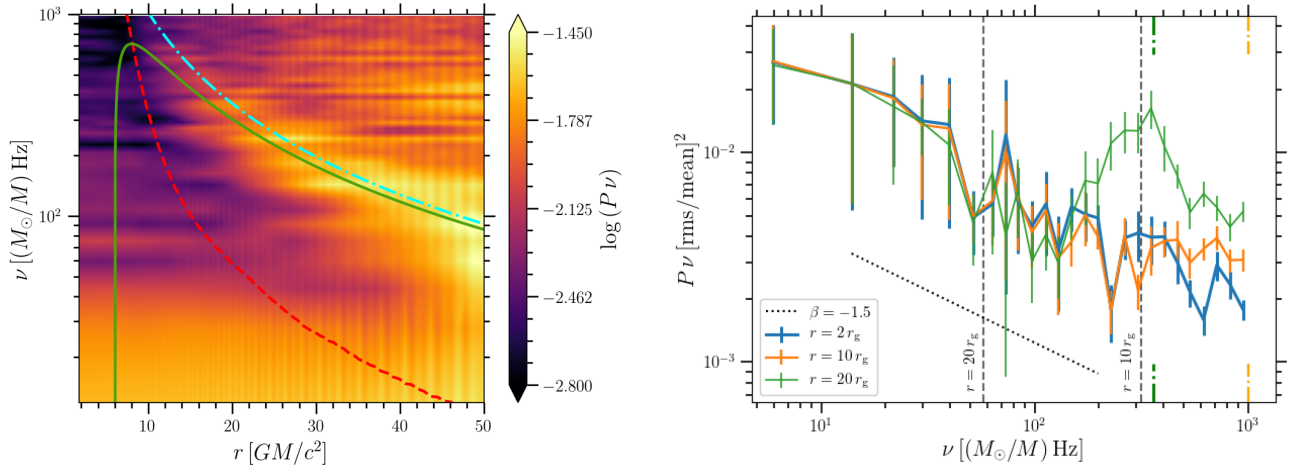
Figure 6. Normalized power spectra of $\dot{m}$ for simulation B. Left-hand panel: variation of power with frequency and radius computed over the time period $[38\,900, 220\,000]\,GM/c^3$ using bins of length $0.13\,(M/M_\odot)$ s. Blue dash–dotted, solid green, and red dashed curves show the Keplerian, radial epicyclic and viscous frequencies, respectively. Right-hand panel: PSDs at 2, 10, and $20\,r_g$ for the same time period but with longer segment lengths of $0.25\,(M/M_\odot)$ s. The average slope of the single power-law fittings to the 2 and $10\,r_g$ curves is indicated by the dotted line. The black dashed lines labeled with radii represent the local viscous frequencies, while the thin orange and thick green dash–dotted lines near the x-axes mark the Keplerian frequencies at 10 and $20\,r_g$, respectively.

then checked if the results differ when we use the accretion rate corrected for the secular decline. The thick blue curve in the same plot shows the average PSD computed for the same radii but now using $\dot{m}_{cor}$ data. The segment length used in this plot is $0.65\,(M/M_\odot)$ s, and so the power spectrum extends down to $1.5\,(M_\odot/M)$ Hz, where we see a significant difference between the PSD of $\dot{m}$ and $\dot{m}_{cor}$. When compared to the left-hand panel, which has shorter segment length (i.e. $0.16\,(M/M_\odot)$ s), the PSD of $\dot{m}_{cor}$ coincides with the PSD of the original (uncorrected) $\dot{m}$ at all the frequencies except the high frequency tail, which starts to differ above $\approx 3000\,(M_\odot/M)$ Hz. Thus, the difference in the PSDs from the original $\dot{m}$ to the corrected $\dot{m}_{cor}$ data starts to become significant as the length of the binned segments increases. Perhaps, this is because the longer time-period variations imposed by the secular decline in $\dot{m}$ can be traced better if the segments are longer, which leads to dominant power at low frequencies in the power spectra.

The break frequencies of the average PSD in the right-hand panel of Fig. 5 do not correspond to the viscous nor the Keplerian frequencies of any of the four radii (2, 5, 10, and $20\,r_g$). Neither do they correspond to any of the characteristic frequencies of the inflow-equilibrium radius. Instead, they appear to be more related to the peak of the radial epicyclic frequency curve, κ_{max}.

4.1.2 Simulation B

The left-hand panel in Fig. 6 shows the power spectra for simulation B, for radii within $50\,r_g$, computed over the time period $[38\,900, 220\,000]\,GM/c^3$ binned into segments of length $0.13\,(M/M_\odot)$ s (same as for simulation A). There is definitely more power above the radial epicyclic frequency, but power within the viscous frequency curve is not as prevalent as in simulation A. In this particular simulation, power along the radial epicyclic and Keplerian frequency curves is more evident, and it seems to be present throughout the simulation period.

The usual interpretation of observations put forward by the propagating fluctuation model requires that at higher frequencies, smaller radii should exhibit more power than larger radii. The right-hand panel of Fig. 6 seems to contradict this. In the figure,

we plot the PSDs for the same radii ($r = 2$, 10, and $20\,r_g$) as Fig. 5 with a longer segment length of $0.25\,(M/M_\odot)$ s. Clearly, the PSD at $20\,r_g$ has more power at higher frequencies compared to 2 and $10\,r_g$. This excess is coming from the power present around the radial epicyclic and Keplerian frequencies seen in the left-hand panel (note that the peak of the green curve in the right-hand panel coincides with the Keplerian frequency at $20\,r_g$ marked by the thick green dash–dotted line).

We do not see any clear break in any of the power spectra in the right-hand panel of Fig. 6, most likely because we are not going to high enough frequencies due to the lower sampling rate of this data. A single power-law fit, with an index close to -1.5 (black dashed line), matches the 2 and $10\,r_g$ curves fairly well. Since $\dot{m}$ does not decrease significantly for simulation B, the PSD of $\dot{m}_{cor}$ is similar to the PSD of $\dot{m}$, and hence we do not show it here.
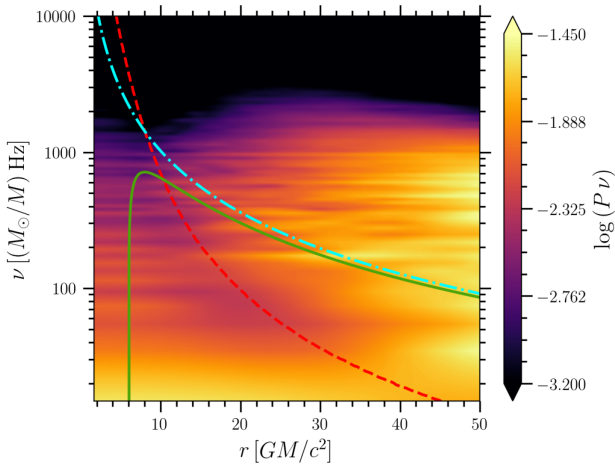
4.1.3 Simulation C

We do a similar analysis for simulation C and the results are shown in Fig. 7. The left-hand panel shows the power spectra for radii within $50\,r_g$ using the same segment length, i.e. $0.13\,(M/M_\odot)$ s, and over the same time window, $[38\,900, 220\,000]\,GM/c^3$, as simulation B. Unlike the previous two simulations, simulation C does not seem to exhibit a strong preference for power above the radial epicyclic frequency. There is also no dominant power along the radial epicyclic frequency/Keplerian frequency curve, nor is there much distinction between inside and outside the viscous frequency curve. This agrees with Fig. 3, where we see that simulation C shows less rapid variability compared to the other simulations.

In the right-hand panel, we plot the PSDs for the same radii ($r = 2$, 10, and $20\,r_g$) with the longer segment length of $0.25\,(M/M_\odot)$ s. Similar to simulation B, we see more high-frequency power at large radii than small and see no evidence for a break in the power spectrum, likely for the same reason as for simulation B. A single power-law fit to the power spectra is provided (black dotted line), with an index close to -1.91, which is perhaps consistent with red-noise behaviour.
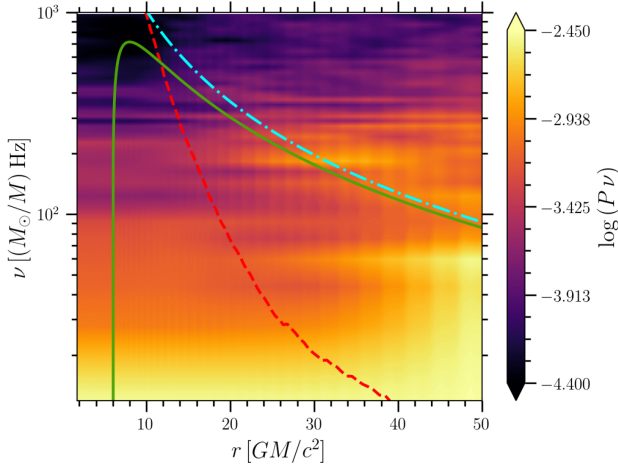
Figure 7. Normalized power spectra of $\dot{m}$ for simulation C. Left-hand panel: variation of power with frequency and radius computed over the time period [38 900, 220 000] GM/c^3 using bins of length 0.13 $(M/\mathrm{M}_\odot)$ s. Blue dash–dotted, solid green, and red dashed curves show the Keplerian, radial epicyclic and viscous frequencies, respectively. Right-hand panel: PSDs at 2, 10, and 20 r_g for the same time period but with longer segment lengths of 0.25 $(M/\mathrm{M}_\odot)$ s. The average slope of the single power-law fittings to all three curves is indicated by the dotted line. The black dashed lines labeled with radii represent the local viscous frequencies and the thin orange and thick green dash–dotted lines near the x-axes mark the Keplerian frequencies at 10 and 20 r_g, respectively.


Figure 8. Normalized power spectra of $\dot{m}$ for simulation R computed for the time period [50 000, 236 670] GM/c^3 binned into segments of length 0.11 $(M/\mathrm{M}_\odot)$ s. The blue dash–dotted, solid green, and red dashed curves show the Keplerian, radial epicyclic and viscous frequencies, respectively.

4.1.4 Simulation R

Simulation R has a higher sampling frequency ($\Delta t = 10\,GM/c^3$), which gives the advantage of being able to study higher frequencies and also obtain better spectra as each bin will now have more data points to average out the noise. In Fig. 8, we show the power spectra of $\dot{m}$ computed over the time period [50 000, 236 670] GM/c^3, during which the flow has reached inflow equilibrium to beyond 50 r_g (see table 1 and fig. 6 of Narayan et al. 2012), with a segment length of 0.11 $(M/\mathrm{M}_\odot)$ s. Interestingly, simulation R exhibits dominant power above the viscous frequency and does not show any difference in power with respect to the radial epicyclic nor Keplerian frequencies. It is worth noting that the power drops drastically at higher frequencies, roughly at the maximum radial epicyclic frequency.

In Fig. 9, we show the power spectra extracted at different radii. The left-hand panel shows the spectra at radii 2, 10 and 20 r_g
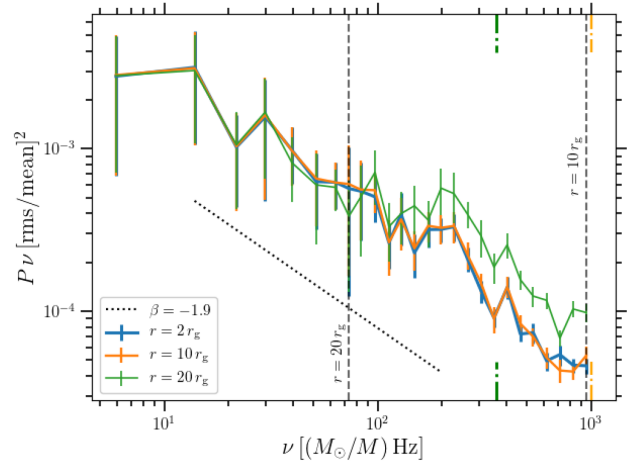
computed using segments of 0.2 $(M/\mathrm{M}_\odot)$ s over the time window[5] [12 000, 236 670] GM/c^3. As in simulation A, we can clearly see that the power spectrum at a given radius is highly coherent with the spectra at smaller radii below the local viscous frequency. This is the case in the other simulations (B, C, and D) as well, but it is harder to notice with the power spectra limited to a small Fourier frequency range due to the relatively poor sampling frequency. Simulation R spectra exhibit a clear break in the frequency, at about 800 $(\mathrm{M}_\odot/M)$ Hz, where the power-law index changes from ~ -1.46 at low frequencies to ~ -2.63 at high frequencies.

Similar to simulation A, we show a comparison of the radially averaged power spectra for $\dot{m}$ and $\dot{m}_\mathrm{cor}$ in the right-hand panel of Fig. 9 using segments of length 0.8 $(M/\mathrm{M}_\odot)$ s. The thin red curves represent the spectra obtained from averaging the PSD of $\dot{m}$ at all radii within 20 and 50 r_g. The thick blue curves represent the same for $\dot{m}_\mathrm{cor}$. Power-law fittings for the averaged spectra within 20 r_g are included. The spectra from $\dot{m}_\mathrm{cor}$ have a slope that is 15 percent flatter at low frequencies compared to the spectra from the original $\dot{m}$. Similar to the average spectra from simulation A, the frequency break in the right-hand panel of Fig. 9 occurs very close to the maximum radial epicyclic frequency. As we noted earlier, this is attributable to the steep decrease in power above roughly 1 $(\mathrm{M}_\odot/M)$ kHz.
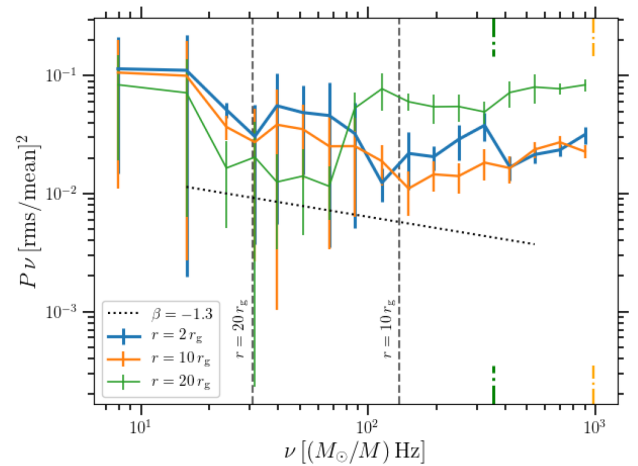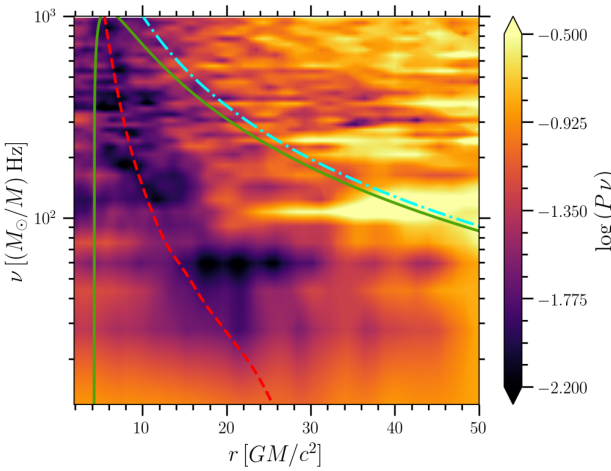
4.1.5 Simulation D

Simulation D is run for a shorter duration, so the power spectra are computed from the averaged periodograms of only two bins with segment lengths close to 0.13 $(M/\mathrm{M}_\odot)$ s. We use the $\dot{m}$ data over the time window [11 000, 63 000] GM/c^3. The left-hand panel of Fig. 10 shows the frequency–radius variation of power spectra and the right-hand panel shows the spectra for the same binning at radii 2, 10 and 20 r_g. Even with less data, we can see that there is dominant power above the radial epicyclic frequency (for $r > 8\,r_\mathrm{g}$) and some power within the viscous frequency curve, similar to simulations A and R. The right-hand panel does not show any clear evidence of

---

[5]By 12 000 GM/c^3, inflow equilibrium is established up to a radius of 20 r_g.
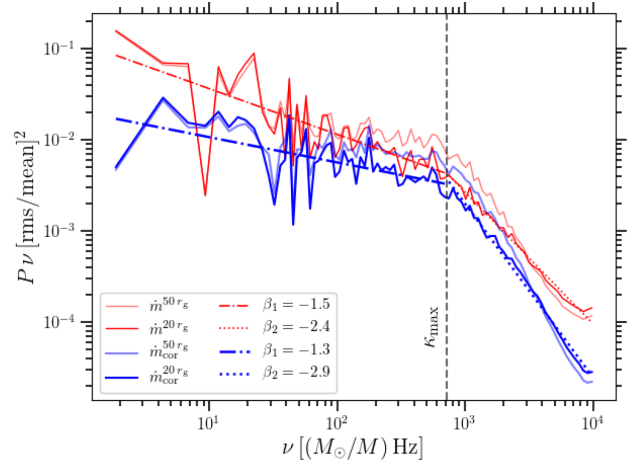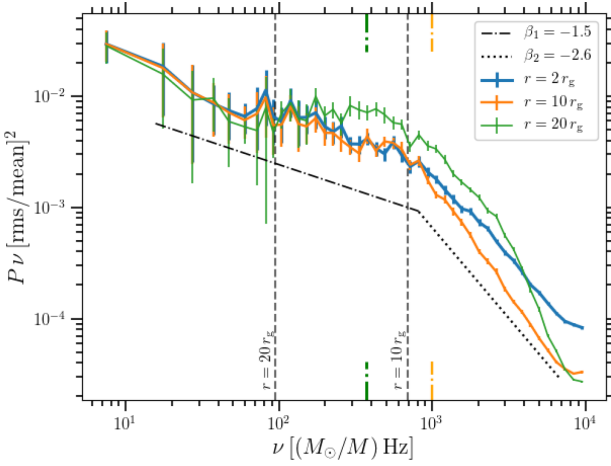
Figure 9. Normalized power spectra of $\dot{m}$ for simulation R at chosen radii. Left-hand panel: PSDs computed from the time window $[12\,000, 236\,000]\,GM/c^3$ using bins of length $0.2\,(M/M_\odot)$ s are shown in blue, orange, and green curves with decreasing line thickness for radii $r = 2$, 10, and $20\,r_\mathrm{g}$, respectively. The average slopes of the power-law fittings to the 2 and $10\,r_\mathrm{g}$ curves are indicated by the black dash–dotted and dotted lines. The Keplerian frequencies at 10 and $20\,r_\mathrm{g}$ are marked near the x-axes in thin orange and thick green dash–dotted lines. The viscous frequencies for all three radii are shown with vertical dashed lines. Right-hand panel: average of the PSDs from all radii within $20\,r_\mathrm{g}$ for the original $\dot{m}$ and corrected $\dot{m}_\mathrm{cor}$ data using longer bins of $0.8\,(M/M_\odot)$ s are shown in thin red and thick blue curves, respectively. Similar curves for averaged PSD within $50\,r_\mathrm{g}$ are shown in lighter shades. The broken power-law fittings for the $20\,r_\mathrm{g}$ averaged data are shown in the dash–dotted and dotted lines. The vertical dashed line shows the maximum of the radial epicyclic frequency, which occurs at $8\,r_\mathrm{g}$.

Figure 10. Power spectra of $\dot{m}$ for simulation D. Left-hand panel: normalized PSD computed for the data in the time window $[11\,000, 63\,000]\,GM/c^3$ using segments of length $0.13\,(M/M_\odot)$ s. Right-hand panel: plot of radial slices at $r = 2$, 10, and $20\,r_\mathrm{g}$. The dotted line shows the average slope obtained from averaging the power-law fits for 2 and $10\,r_\mathrm{g}$ curves. Vertical dashed lines give the viscous frequency for labelled radii, and the thin orange and thick green dash–dotted lines close to the x-axis mark the Keplerian frequencies for 10 and $20\,r_\mathrm{g}$, respectively.

a break, most likely because of the low sampling frequency of the data. We find the averaged slope of the single power-law fits to the 2 and $10\,r_\mathrm{g}$ curves is around -1.25, closer to flicker-noise behaviour, whereas the best fit to the $20\,r_\mathrm{g}$ curve has a slope of -0.77. Here, and in Figs 6 and 7, the large error bars are most likely due to the fact that the number of time intervals (N) in each segment is only a couple of hundred, i.e. at least an order of magnitude less than what is possible for simulations A and R (Figs 5 and 9).

The large amount of power found *above* the viscous frequency, and even above the radial epicyclic frequency, in these spectra is certainly not what is expected from the propagating fluctuation model. To explore this further, in Fig. 11, we include power spectra from simulation D where we limit the vertical extent of the domain included in the calculation. We consider both the mid-plane value of $\dot{m}$ (left-hand panel) and $\dot{m}$ within one scale height of the mid-plane (right-hand panel). In both cases, the relative power found above the

radial epicyclic frequency is greatly reduced (compared to Fig. 10). However, most of the power is still above the viscous frequency.

4.2 Radial coherence

We turn our focus now, though, to the variability power found *below* the viscous frequency, the source of which could be the propagating fluctuations we are searching for. According to the propagating fluctuations model, fluctuations driven at different radii should modulate the fluctuations at smaller radii as they propagate in on the viscous time-scale. Any fluctuations above the local viscous frequency should be damped, so they are unable to make it to smaller radii. Thus, the model predicts that the accretion rate between any two radii should exhibit high coherence below the viscous frequency and low coherence above it. In X-ray observations, this translates into a strong coherence between light curves in different energy

$\dot{m}(\theta = \pi/2)$ $\dot{m}$ within one scale height
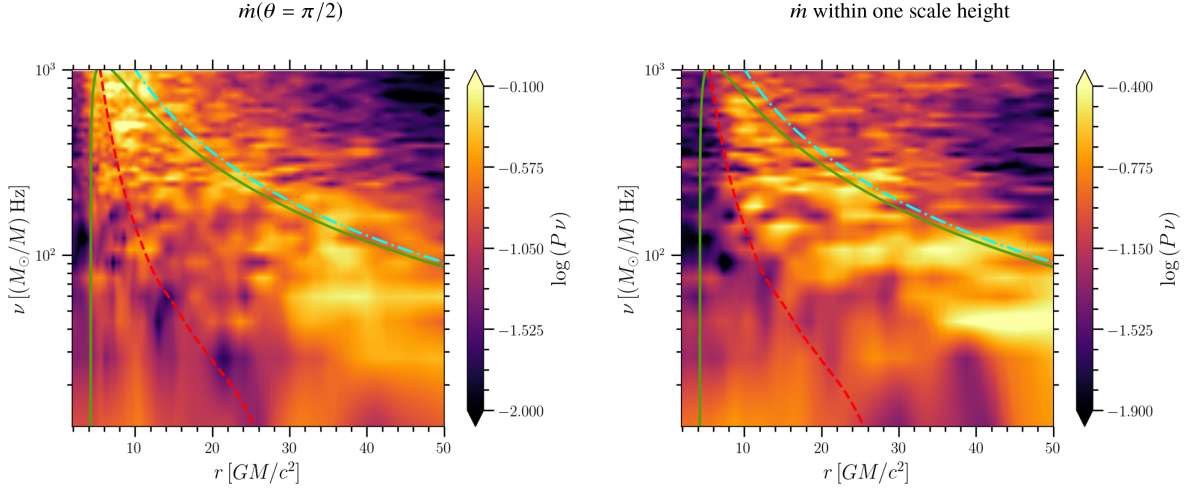
Figure 11. Normalized power spectra of the mid-plane value of $\dot{m}$ (left-hand panel) and $\dot{m}$ within one scale height of the mid-plane (right-hand panel) for simulation D. Spectra are computed over the time window $[11\,000, 63\,000]\,GM/c^3$ using bins of length $0.13\,(M/M_\odot)$ s. The blue dash–dotted, solid green, and red dashed curves show the Keplerian, radial epicyclic, and viscous frequencies, respectively.

bands, with the assumption that higher energy bands originate from radii closer to the black hole and lower energy bands come from further out.

Coherence fundamentally describes the fractional variance between two curves, which can be predicted via a linear transformation between them (Vaughan & Nowak 1997). In our case, let $h(t)$ and $s(t)$ denote $\dot{m}$ curves at any two radii, r_1 and r_2, with respective Fourier transforms $H(\nu)$ and $S(\nu)$. Then, following Uttley et al. (2014), we compute the radial coherence of $\dot{m}$ between r_1 and r_2 using

$$\gamma^2(\nu_j) = \frac{|C_{\mathrm{HS}}(\nu_j)|^2}{P_{\mathrm{H}}(\nu_j)P_{\mathrm{S}}(\nu_j)} , \qquad (4)$$

where $C_{\mathrm{HS}} = H^*S$ is the cross-spectrum averaged over multiple time segments and frequency bins and $P_{\mathrm{H}}(\nu_j)$ and $P_{\mathrm{S}}(\nu_j)$ are the power spectra obtained from $h(t)$ and $s(t)$, respectively, with similar averaging. If $h(t)$ and $s(t)$ are related through a linear transformation in time, the two are said to be perfectly coherent, and γ^2 reaches its maximum value of 1. When $h(t)$ and $s(t)$ are completely unrelated, $\gamma^2 = 0$ and they are said to be incoherent.

In Fig. 12, we show the radial coherence of all radii up to $50\,r_{\mathrm{g}}$ with respect to the inner radius (black hole horizon) for all five simulations. The black dashed line represents the viscous frequency, while the white dash–dotted line gives the Keplerian frequency. We consider the same binning of $\dot{m}$ as we did for the radius-frequency plots of power spectra in the previous section. We find that in all cases, $\dot{m}$ shows remarkable coherence below the local viscous frequency at all radii. Similar radial coherence is observed in the simulations and models of geometrically *thin* discs (Hogg & Reynolds 2016; Mushtukov et al. 2018). In addition, simulations A and C exhibit significant coherence even above the viscous frequency, up to a factor few below the Keplerian frequency, particularly at larger radii. It is interesting to note that these are the two simulations that show equatorial backflow.

4.3 Time lags

The presence of frequency-dependent, radial coherence indicates that fluctuations at different radii are causally connected. However, information about the direction of propagation of these fluctuations is missing from a simple coherence plot. To extract this information,

Table 2. Accretion time-scales and time lags for different radii within each simulation.

Simulation	r (r_{g})	t_{acc} $[(M/M_\odot)$ ms]	t_{lag} $[(M/M_\odot)$ ms]
A	2	4.57	0.25
	6	4.41	0.18
	10	3.46	0.08
B	2	3.44	0.46
	6	3.28	0.4
	10	2.52	0.25
C	2	1.36	0.25
	6	1.26	0.18
	10	0.98	0.09
R	2	1.65	0.44
	6	1.57	0.37
	10	1.23	0.21
D	2	7.79	1.59
	6	7.37	1.5
	10	5.32	0.88

Note. The time lags are averaged from values below the viscous frequency at $15\,r_{\mathrm{g}}$.

we compute the time leads/lags between $\dot{m}$ at different radii. The strong coherence seen in Fig. 12 implies that the two mass fluxes must be related by a phase shift $(\Delta\Phi)$ that can be calculated from the ratio of the imaginary and real parts of the cross-spectrum, C_{HS}. Time lags are then obtained using $\Delta\tau = \Delta\Phi/(2\pi\nu)$.

In Fig. 13, we show the time lags of $\dot{m}$ at $r = 2$ (blue solid curve), 6 (orange dashed curve), and $10\,r_{\mathrm{g}}$ (green dash–dotted curve) with respect to $15\,r_{\mathrm{g}}$. We do not show the lags where the coherence drops below 0.1. We find in all simulations that fluctuations below the viscous frequency at $15\,r_{\mathrm{g}}$ (black dashed line) show positive, definite lags when comparing small radii to larger radii, and for the most part, the magnitudes of the lags increase for larger radial separations. However, comparing the measured lags to the local accretion time-scale ($t_{\mathrm{acc}} = \int_r^{15} V^r(r, t)\,\mathrm{d}r$) for each radius (Table 2), we find they are uniformly shorter, too short to correspond to the viscous time-scale and more consistent with the local Keplerian time-scale.

We also find some evidence for negative lags at frequencies higher than the viscous frequency. Negative lags are also present in the
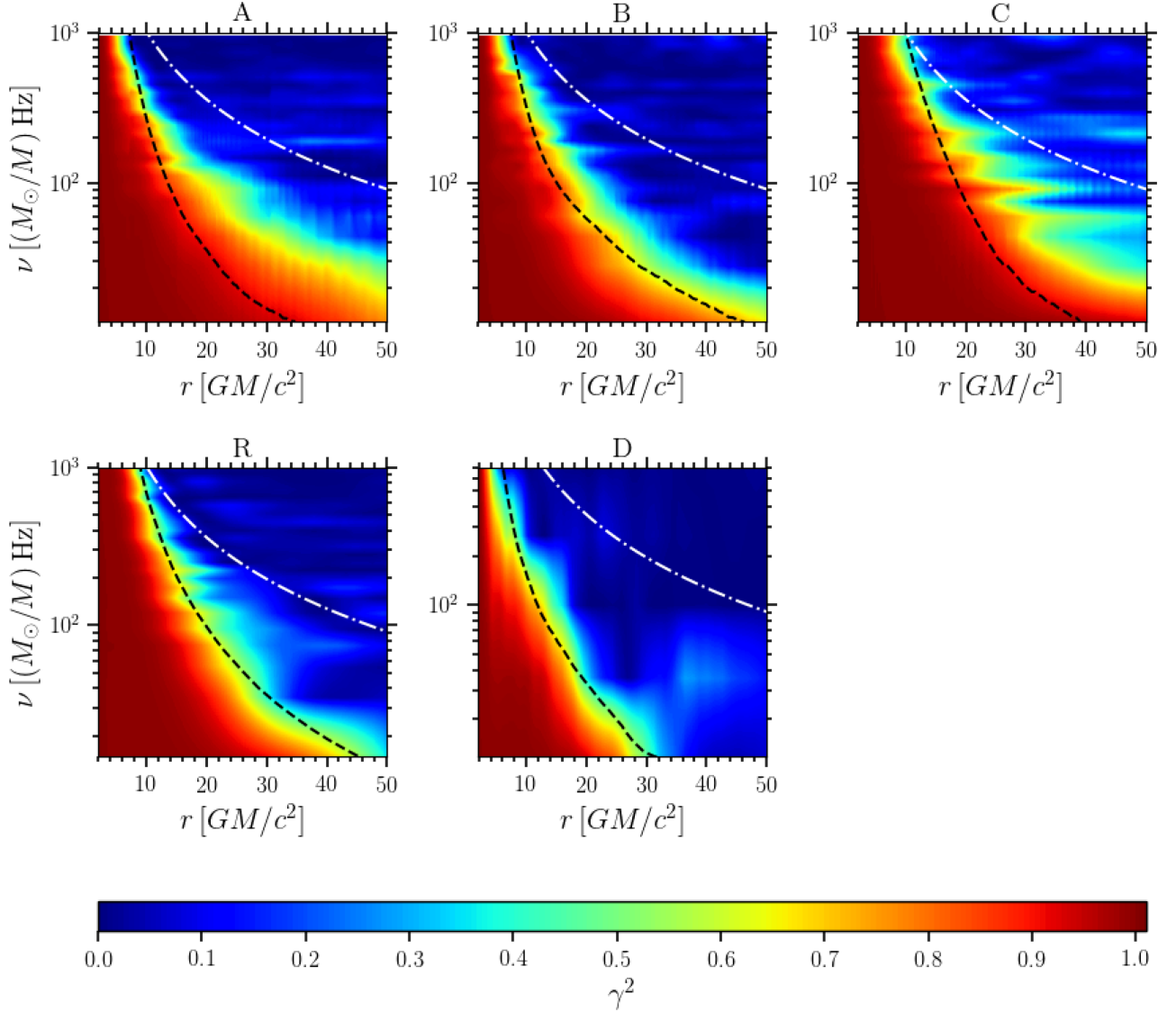
Figure 12. Radial coherence measured with respect to the inner radius. The white dash–dotted curve represents the Keplerian frequency and the black dashed curve represents the viscous frequency below which strong coherence is maintained.

thin-disc model of Mushtukov et al. (2018, see fig. 9b of their paper), where they are explained as high-frequency variability from the inner disc affecting variability at larger radii, due to outward propagating waves; in contrast, inward-propagating high-frequency fluctuations from large radii are damped before they reach the inner disc, according to the model. The picture from our thick-disc simulations is less clear, however, as we only see negative lags in some of the simulations. In principle, in regions of backflow (which are present in simulations A and C), mass accretion rate fluctuations may also be simply transmitted outwards by the fluid moving away from the black hole.

One issue with Fig. 13 is that for frequencies below the viscous one we do not find a well-defined frequency dependence in the time lags. In our analysis, the time lags simply correspond to the propagation times between $15\,r_{\mathrm{g}}$ and the inner radii, which are independent of the Fourier frequency. It could be that the dissipative processes that convert $\dot{m}$ into luminosity in real discs are selective to certain frequencies (perhaps set by the local dissipation time-scale). This could potentially be the source of the frequency dependence

observed in time lags measured from actual light curves. Going by this argument, $\dot{m}$ may not be a good proxy for luminosity when studying timing properties that involve dissipative processes. Propagating fluctuation models (Kotov et al. 2001; Arévalo & Uttley 2006; Mahmoud & Done 2018a) get around this problem and recover frequency-dependent time lags by weighting the propagation time of the fluctuations by an emissivity profile that accounts for the conversion of mass accretion rate into luminosity. We will perform a similar procedure in Section 5.

4.4 The rms–flux relationship

Observed light curves for several black hole binaries and AGNs display a linear relationship between the rms and the mean of the flux (Uttley & McHardy 2001), indicating that the brighter the source, the more variable it is. This linear rms–flux relation is considered to be a more important and fundamental characteristic of X-ray variability than power spectra for two main reasons: (a) This relationship is observed during all spectral states of BHXRBs, while
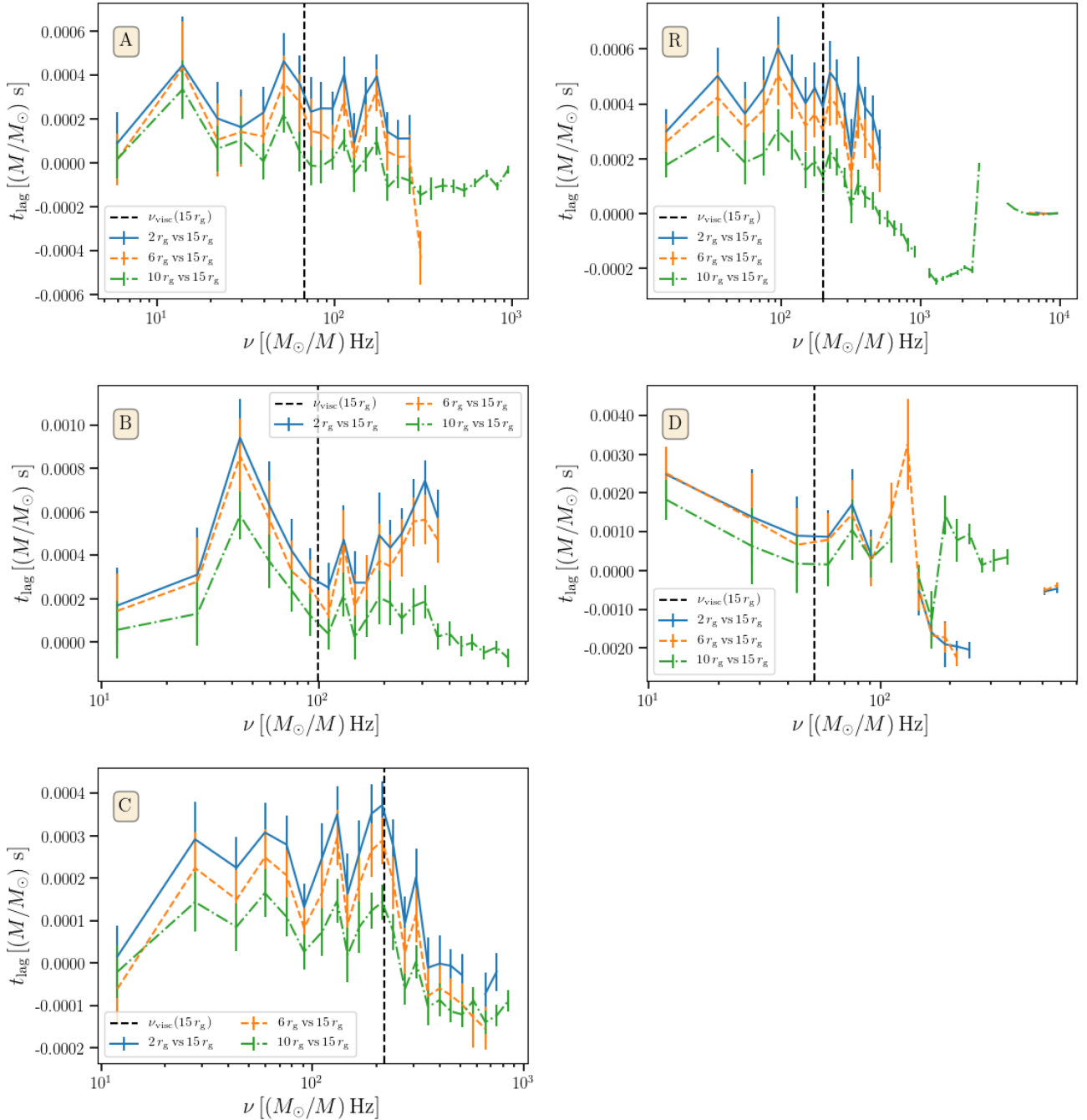
Figure 13. Time lags of the $\dot{m}$ fluctuations for radii 2, 6, and $10\,r_{\mathrm{g}}$ with respect to $15\,r_{\mathrm{g}}$ for all five simulations. The dashed line represents the viscous frequency at $15\,r_{\mathrm{g}}$. Lags with coherence less than 0.1 are omitted.

the PSD shape evolves during these spectral transitions (Gleissner et al. 2004); and (b) PSD alone cannot distinguish between different variability models, while the rms–flux relation can.

Even a casual examination of Fig. 1 reveals that the amplitude of $\dot{m}$ variability in all our simulations increases and decreases in proportion to the magnitude of $\dot{m}$, consistent with an rms–mass flux relationship. To test this formally, we compute the rms–mean flux relationship for $\dot{m}$ at the ISCO, (which is $6\,r_{\mathrm{g}}$ for all simulations except simulation D, which has its ISCO at $4.24\,r_{\mathrm{g}}$). The usual way to compute the rms–flux relation is to divide the $\dot{m}$ data into a certain number of bins, and then compute the mean and absolute rms of $\dot{m}$ in each bin, which can then be plotted to get the relationship. This

method obviously does not discriminate between the propagating fluctuations assumed in the model and possible non-dissipative, high-frequency fluctuations. One way we could filter out the non-dissipative fluctuations while computing the rms–mean relationship is to compute the rms using power spectra. Since we compute the root-mean square normalized power spectra, one can obtain the rms by simply integrating the power over the desired frequency range and taking the square root of it. Our radial coherence plots and time lag plots strongly suggest that below the local viscous frequency, dissipative fluctuations propagate inwards, which sets the upper limit on the relevant frequency range. Following a procedure similar to Uttley & McHardy (2001), we divide the $\dot{m}$ data into a certain
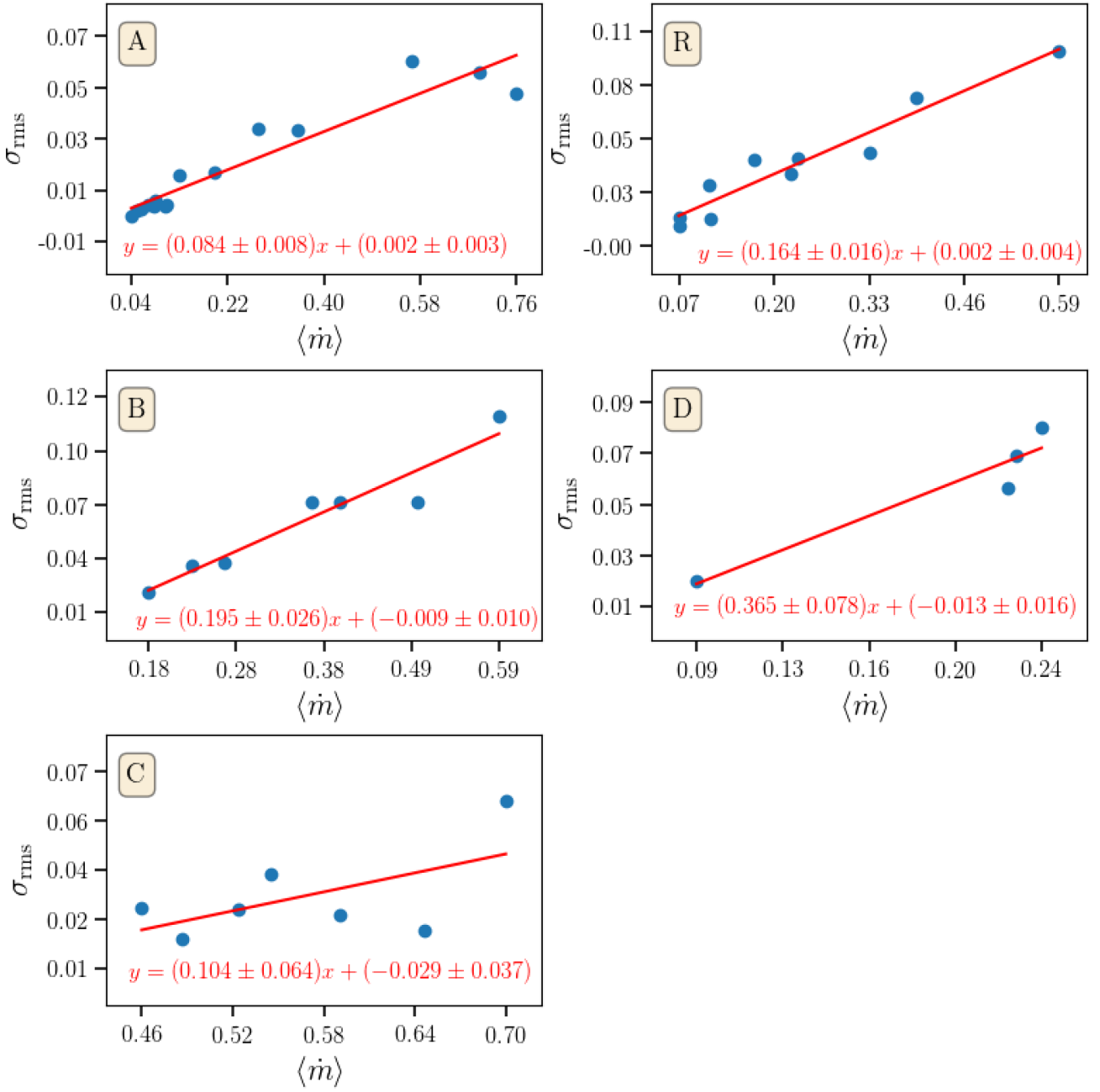
Figure 14. rms–mean relation computed for $\dot{m}$ at the ISCO for all five simulations. Fits using equation (5) are provided for each case.

number of bins and for each bin we compute its periodogram, as described in Section 4.1, except that now we do not average the periodograms obtained over all the segments, but we do average the periodograms over each logarithmically spaced frequency bin to obtain the (rms/mean)^2 power spectra. Next, we multiply the spectrum by the squared, mean value of $\dot{m}$ in that bin and integrate over all the frequencies below the viscous frequency. Finally, we take the square root of the result to recover the rms value. We repeat this procedure for each bin and then plot the results in Fig. 14. For all simulations except D, we use the same binning as for their radius-frequency power spectra, i.e. segments of length $0.13\,(M/M_\odot)$ s for simulations A, B, and C, and $0.11\,(M/M_\odot)$ s for simulation R. Since we need more than two points to look for a trend, we consider smaller segments of length $0.06\,(M/M_\odot)$ s for simulation D. Data

from each simulation are fit with the following linear function using a least-squares method (Uttley & McHardy 2001):

$$\sigma_{\rm rms} = k\langle\dot{m}\rangle + C. \qquad (5)$$

The resulting relations along with their least-squares fits are reported in Fig. 14.

Simulations A, B, and R, seem to show strong linear rms–mass flux relations, as observed in nature. However the slopes are smaller than what is typically observed in BHXRBs. For Cygnus X-1, for example, the observed slope in the low/hard state is close to 0.3, and only decreases to around ∼0.16 in the high/soft state (Gleissner et al. 2004). Simulation D exhibits the highest slope at ≈0.4 (but perhaps, this is not reliable as it is anchored by a single low-frequency point), followed by simulations B and R with slopes at ≈0.2. Simulations A
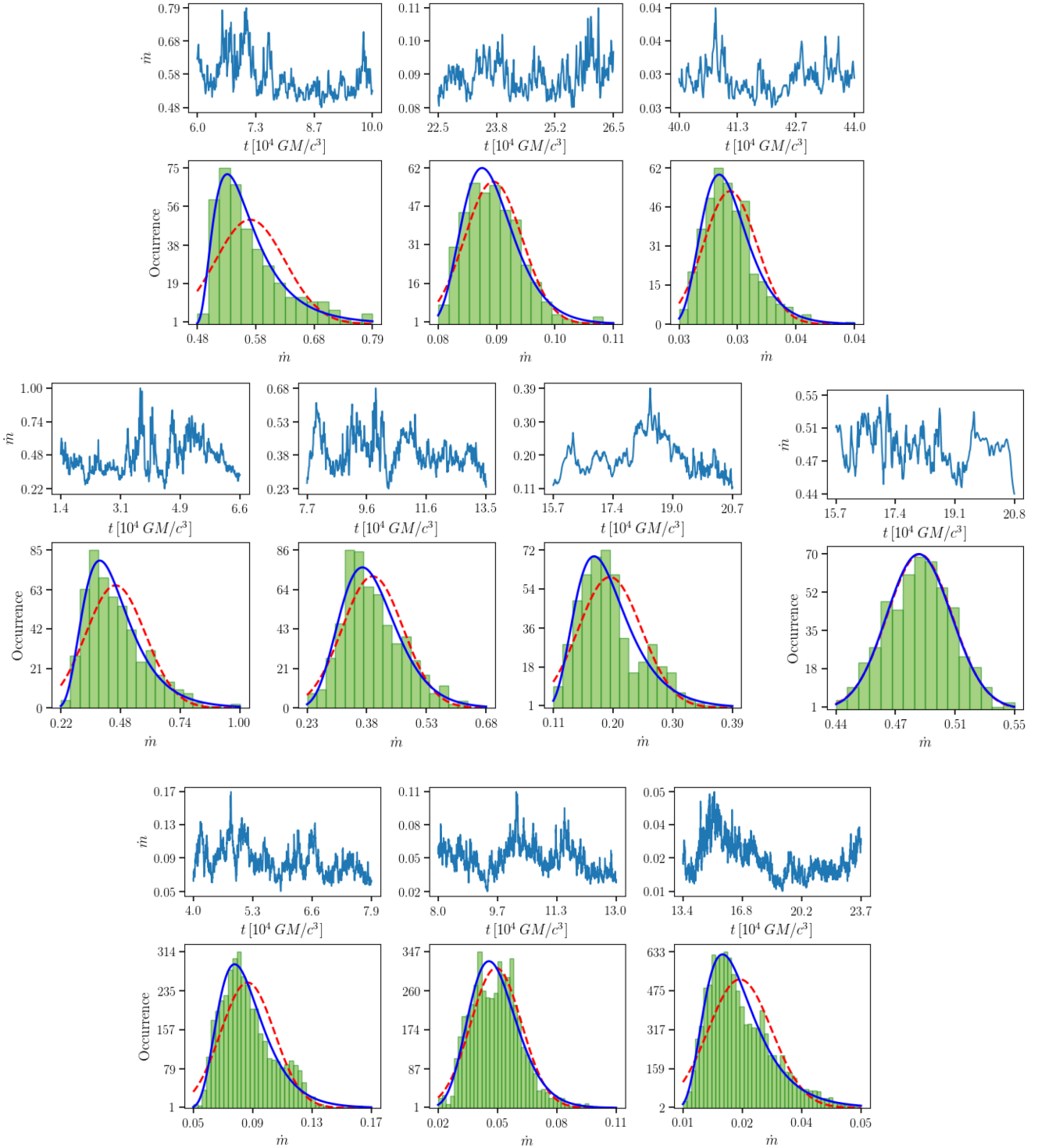
Figure 15. Distribution of $\dot{m}$ for simulations A, B, C, and R for different time segments during which $\dot{m}$ is reasonably stationary. The best fits of normal and lognormal distributions are shown in red dashed and blue solid curves, respectively.

and C appear to show linear rms–$\dot{m}$ relations, although their slopes are quite small. For simulation A, this could be the result of the secular decline in $\dot{m}$. For simulation C, this could possibly be due to the initial rise followed by a decline in $\dot{m}$. We note that upon using the corrected $\dot{m}_{\mathrm{cor}}$ curves, the rms–$\dot{m}$ relation is actually more scattered, possibly due to residuals between the actual decay and the exponential fit.

4.5 Lognormal distribution

Another signature of an underlying non-linear variability process is a lognormal distribution of the observed flux (Uttley et al. 2005). The presence of a lognormal distribution indicates that the variability is caused by a multiplicative process, which here happens to be the coupling between fluctuations at different radii. Before testing our distributions of $\dot{m}$ for lognormality, it is important to note

Table 3. Parameters for the normal and lognormal fits to the mass flux histograms, corresponding to the plots in Fig. 15.

Simulation	Normal			Lognormal			
	μ	σ	χ^2/d.o.f.	μ	σ	τ	χ^2/d.o.f.
A	0.57	0.06	252.4/13	-2.44	0.58	0.47	23.8/12
	0.09	0.005	182.5/14	-4.0	0.28	0.07	14.7/13
	0.03	0.002	609.4/17	-5.0	0.30	0.03	13.8/16
B	0.46	0.13	277.8/16	-1.25	0.41	0.15	16.0/15
	0.39	0.08	71.8/16	-1.16	0.24	0.07	28.1/15
	0.2	0.05	86.1/16	-2.11	0.38	0.07	32.1/15
C	0.49	0.02	11./13	-0.38	0.03	-0.2	11.1/12
R	0.18	0.04	1459.1/38	-2.29	0.36	0.07	217.0/37
	0.11	0.02	1257.4/42	-2.1	0.2	-0.02	278.2/41
	0.05	0.02	1726.1/42	-3.38	0.42	0.01	216.8/41

that the phenomenological models used to explain the lognormal distribution of flux assume that the light curve is at least weakly stationary, i.e. the mean and variance do not change significantly within the time window of interest, while the higher 'moments' may change. As we noted in earlier sections, $\dot{m}$, for most of our simulations, undergoes a secular decline, implying it is not stationary over the period we wish to analyse. For this reason, we compute the distributions of $\dot{m}$ at the horizon only for data segments during which $\dot{m}$ is reasonably stationary[6] as shown in Fig. 15. In Appendix B, we show what the distributions look like if the entire simulation duration is considered.

In Fig. 15, in the top row of each panel, we show the $\dot{m}$ segments used for each simulation. Below that, we show the resulting histograms, fitted with both normal (red dashed curve) and lognormal (blue solid curve) distributions. The lognormal fit is made using

$$f(x; \mu, \sigma, \tau) = \frac{1}{\sqrt{2\pi}\sigma(x-\tau)} \exp\left\{-\frac{\left[\log(x-\tau)-\mu\right]^2}{2\sigma^2}\right\}, \quad (6)$$

with τ as an offset parameter. Best-fitting parameters for these distributions are provided in Table 3.

Although simulation A shows significant decline in $\dot{m}$, there are sufficiently long time segments during which $\dot{m}$ is stationary enough to reasonably expect a well-defined distribution. We found that, indeed, the $\dot{m}$ distributions in these segments are statistically well fit by a lognormal distribution, with χ^2/d.o.f. = 1.98, 1.13, and 0.86. This is not true for the entire simulation data (see Fig. B1).

Similar to simulation A, the shorter time segments of simulation B show statistically significant lognormal distributions, with χ^2/d.o.f. = 1.10, 1.87, and 2.14. Even though, in this case, the secular decline is not very steep, the entire simulation data are still not well fit by a lognormal distribution (see Table B1). None of the data segments give an acceptable fit for a Gaussian distribution (see Table 3).

In the case of simulation C, the steady increase in $\dot{m}$ initially, followed by its gradual decline, makes it hard to find a reasonably long time segment in which $\dot{m}$ is stationary. In Fig. 15, we show a segment chosen towards the end of the simulation, where $\dot{m}$ is nearly stationary. In contrast to the previous results, we find this distribution to be well fitted by either a normal or lognormal distribution.

For different time segments in simulation R, we find that both visibly and based on $\Delta\chi^2$ values, a lognormal distribution fits better than a normal one. However, the obtained χ^2/d.o.f. for the lognormal fits are not statistically acceptable. A similar conclusion is reached when the entire duration is considered (see Table B1).
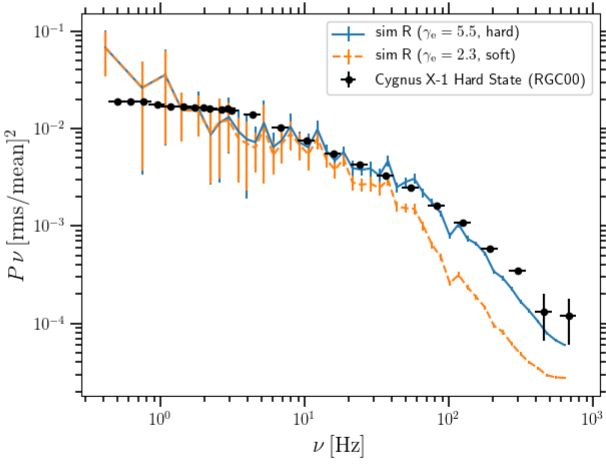
Simulation D does not exhibit as significant a decline as the other simulations, so we show its entire distribution of $\dot{m}$ in Fig. B1, along with the other simulations. This simulation is well fitted by a lognormal distribution with χ^2/d.o.f. = 1.12.

5 COMPARISON WITH OBSERVATIONS

One must take care when comparing the results of these simulations to light curves, as of course observed light curves are not a result of just the mass accretion rate profiles present in the flow, but a product of the $\dot{m}$ time series with their associated spectral emission components. Indeed, the mass accretion rate behaviour at a given radius may be effectively invisible to observers if there is no corresponding emission mechanism at that location, or the variability at a given radius may be greatly amplified in observations if the relevant emission mechanism at that radius happens to dominate the observed energy band. Drawing direct analogies to observed light curves is, therefore, risky, but we can begin to draw some qualitative comparisons nevertheless.

The power spectral profile exhibited by simulations A and R, in particular (Figs 5 and 9), show many interesting points of overlap with observation. As in these simulations, an abundance of power over a broad frequency range with a break at high-frequencies is commonly observed in X-ray binary light curves at low accretion rates (e.g. Gierlinski et al. 1997; Axelsson 2008). This high-frequency break has generally been attributed to the viscous frequency at the inner edge of the accretion flow, although interference effects may lower the actual frequency (Ingram & Done 2011). In this picture, it would be strange then for the power from 2, 10, and 20 r_g to have very similar break frequencies. However, we note that observations of light curves in different energy bands from a given source (Wilkinson & Uttley 2009; De Marco et al. 2015) exhibit high-frequency breaks in the same range, often with no apparent correlation with band centroid energy consistent with our simulation results.

The presence of inter-annular time lags also represents an excellent bridge between simulations and observations. The model for how inter-band time lags arise in observed accretion flows requires that fluctuations generated in the outer disc first liberate energy there, before propagating inwards to modulate emission at smaller radii and produce the observed lag (Lyubarskii 1997). For a typical

---

[6]We select these segments by 'eye', so the results may not be representative of the statistical results of the full data.

Figure 16. Power spectra of simulation R for hard and soft energy bands, overlayed with the observational data of Cygnus X-1 in the hard state, taken from Revnivtsev, Gilfanov & Churazov (2000) (RXTE ObsID P30157). Here, we assume $M_{\text{Cyg X-1}} = 15\,\text{M}_\odot$.
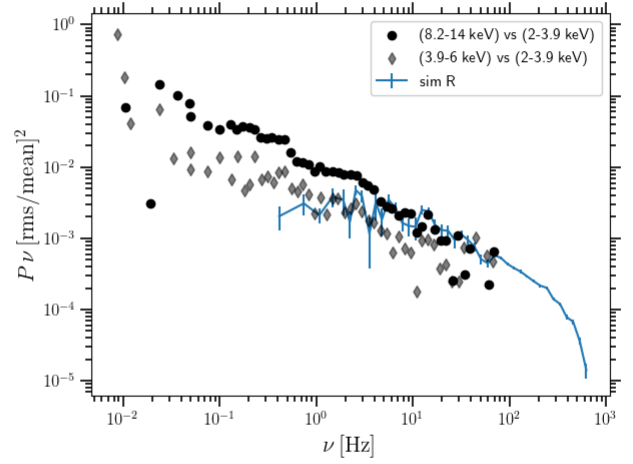

Figure 17. Lag spectrum of hard band versus soft band for simulation R, compared with the observed lags in low/hard state of Cygnus X-1 (Nowak et al. 1999; Poutanen 2001). Here, we assume $M_{\text{Cyg X-1}} = 15\,\text{M}_\odot$.

10-$\text{M}_\odot$ BH, Fig. 13 and Table 2 indicate lags of the order of 1–10 ms, which are comparable to the lags observed between low- and high-energy X-ray bands in many sources in the hard state (De Marco et al. 2017; Mahmoud & Done 2018b).

One aspect missing from the GRMHD results is the power-law decay in time lag with frequency commonly seen in observations. In our simulations, lags are simply explained by the propagation time from one radius to another and therefore are frequency-independent. However, the dissipative processes that convert $\dot{m}$ into luminosity could potentially introduce some frequency dependence in the lags. Often in models, these dissipative processes are well captured by radially dependent emissivity profiles (see for example Ingram & Done 2011; Ingram & van der Klis 2013). Here we follow a similar procedure and compute the emissivity-weighted flux observed in a particular energy band as

$$f(t) = \sum_{r=r_{\text{H}}}^{r_{\text{out}}} \epsilon(r)\,\dot{m}(r,t)\,, \tag{7}$$

where we take the emissivity profile $\epsilon(r) = (\mathrm{d}r/r)\,r^{2-\gamma_e}$, and γ_e is the emissivity index, which is a free parameter. The higher energy $r_{\text{out}} = 25\,r_g$ band is expected to have a steeper emissivity profile compared to the soft-energy band; therefore, we take $\gamma_e = 5.5$ and 2.3 for the hard and soft energy bands, respectively. Fig. 16 shows the power spectra of the thus-obtained light curves in the hard and soft energy bands for simulation R. Within the measurable range, the simulation hard band power spectrum is consistent with the power seen in, e.g. the hard states of Cygnus X-1 (Revnivtsev et al. 2000). Note that, due to the limited duration of these simulations, our power spectra can only go down to $\nu \sim 10\,(\text{M}_\odot/M)$ Hz. This means we cannot probe the range where one typically sees what is called the low-frequency break, $\nu \sim 0.1$ to $1\,(\text{M}_\odot/M)$ Hz.

We can also use our synthetic light curves to measure the time lags between the hard and soft bands. Results for simulation R are shown in Fig. 17. Unlike the lags measured from coherent $\dot{m}$ fluctuations between any two radii, which are frequency-independent (see Fig. 13), these lags vary with the frequency (e.g. declining monotonically, within error, between 5 and 100 Hz in Fig. 17) and match well with the lag spectra between different energy bands for Cygnus X-1 in the hard spectral state (Nowak et al. 1999; Poutanen 2001). This simple exercise indicates that dissipative processes

could play a vital role in modulating the underlying variability in $\dot{m}$, as it is imprinted on the light curve. GRMHD simulations that include radiative processes will be needed to explore this idea further.

Taken together, the presence of inter-annular time lags of magnitude matching the observations, the presence of high-frequency breaks in many of the power spectra, and the systematic trends in the coherence represent an excellent starting point from which observers may begin to interpret real light curves in terms of the underlying $\dot{m}$ behaviour.

6 CONCLUSIONS

In this work, we tested the hypothesis that the broad-band X-ray variability observed in black hole X-ray binaries and AGN is attributable to mass–flux variations in the accretion flow. We did this through analysis of a suite of long-duration, GRMHD simulations. We considered the mass accretion rate as a proxy for luminosity to identify multiple variability features. We found that, despite the differences in the initial set-ups and outcomes of the simulations, each one showed evidence for inward propagating fluctuations. Our findings include the following:

(i) In general, the power spectra from these simulations have two components: low-frequency power below the viscous frequency and high frequency power above the Keplerian frequency, with the exception of simulation C, which shows relatively less $\dot{m}$ variability.

(ii) Simulations show evidence for power along and above the Keplerian frequency curve. The presence of this power causes the high frequency power at larger radii to dominate that at smaller radii. While this is in contrast to X-ray observations, in which higher energy bands exhibit more high-frequency power compared to lower energy bands, the presence of the high frequencies only above the Keplerian curve strongly suggests they are associated with p modes, which are not likely to strongly modulate the light curve. Perhaps, with proper treatment of radiative processes (i.e. radiative GRMHD simulations), we would be able to filter out the non-dissipative, high-frequency fluctuations by obtaining the power spectra directly from the luminosity.

(iii) The $\dot{m}$ power spectra at a given radius exhibit strong similarity with spectra at smaller radii below the local viscous

frequency. This is in contrast to model assumptions that emission at each radius peaks at the local viscous frequency.

(iv) All simulations show remarkable radial coherence below the viscous frequency. This agrees well with how most models explain the strong coherence between energy bands.

(v) All simulations display positive time lags below the viscous frequency, when comparing the fluctuations of $\dot{m}$ at smaller radii with those at larger radii. This, together with the radial coherence, strongly supports the presence of inward propagating fluctuations in the accretion flow.

(vi) The time lags between highly coherent fluctuations of $\dot{m}$ between any two fixed radii are frequency-*independent*.

(vii) When they are measured between two synthetic energy bands, generated using power-law emissivity profiles, the same $\dot{m}$ fluctuations yield frequency-*dependent* time lags, consistent with X-ray observations.

(viii) All simulations show a linear rms–mean $\dot{m}$ relation, although the slopes obtained are smaller than typically observed from linear rms–mean flux relations in BHXRBs.

(ix) All simulations, except R, show lognormal behaviour within those time segments in which $\dot{m}$ is approximately stationary. This strongly supports the notion that the fluctuations arise from a multiplicative, stochastic process.

In conclusion, this work is a promising step toward confirming the propagating fluctuation model and connecting simulations with observations.

ACKNOWLEDGEMENTS

DATA AVAILABILITY

The data underlying this paper will be shared on a reasonable request to the corresponding author.

REFERENCES

Anninos P., Fragile P. C., Salmonson J. D., 2005, ApJ, 635, 723
Arévalo P., Uttley P., 2006, MNRAS, 367, 801
Axelsson M., 2008, in Axelsson M., ed., AIP Conf. Ser. Vol. 1054, Cool Discs, Hot Flows: The Varying Faces of Accreting Compact Objects. Am. Inst. Phys., New York, p. 135
Balbus S. A., Hawley J. F., 1991, ApJ, 376, 214
Blandford R. D., Begelman M. C., 1999, MNRAS, 303, L1
Chakrabarti S. K., 1985, ApJ, 288, 1

Churazov E., Gilfanov M., Revnivtsev M., 2001, MNRAS, 321, 759
Colella P., Woodward P. R., 1984, J. Comput. Phys., 54, 174
De Marco B., Ponti G., Muñoz-Darias T., Nandra K., 2015, MNRAS, 454, 2360
De Marco B. et al., 2017, MNRAS, 471, 1475
Done C., Gierliński M., Kubota A., 2007, A&AR, 15, 1
Fishbone L. G., Moncrief V., 1976, ApJ, 207, 962
Fragile P. C., Gillespie A., Monahan T., Rodriguez M., Anninos P., 2012, ApJS, 201, 9
Fragile P. C., Olejar A., Anninos P., 2014, ApJ, 796, 22
Gammie C. F., McKinney J. C., Tóth G., 2003, ApJ, 589, 444
Gaskell C. M., 2004, ApJ, 612, L21
Gierlinski M., Zdziarski A. A., Done C., Johnson W. N., Ebisawa K., Ueda Y., Haardt F., Phlips B. F., 1997, MNRAS, 288, 958
Gleissner T., Wilms J., Pottschmidt K., Uttley P., Nowak M. A., Staubert R., 2004, A&A, 414, 1091
Hogg J. D., Reynolds C. S., 2016, ApJ, 826, 40
Ichimaru S., 1977, ApJ, 214, 840
Ingram A., Done C., 2011, MNRAS, 415, 2323
Ingram A., van der Klis M., 2013, MNRAS, 434, 1476
King A. R., Pringle J. E., West R. G., Livio M., 2004, MNRAS, 348, 111
Kluzniak W., Kita D., 2000, preprint (astro–ph/0006266)
Kotov O., Churazov E., Gilfanov M., 2001, MNRAS, 327, 799
Lightman A. P., Shapiro S. L., 1975, ApJ, 198, L73
Lyubarskii Y. E., 1997, MNRAS, 292, 679
McHardy I. M., Papadakis I. E., Uttley P., Page M. J., Mason K. O., 2004, MNRAS, 348, 783
McKinney J. C., 2006, MNRAS, 368, 1561
McKinney J. C., Blandford R. D., 2009, MNRAS, 394, L126
McHardy I., 1988, Mem. Soc. Astron. Ital., 59, 239
Mahmoud R. D., Done C., 2018a, MNRAS, 473, 2084
Mahmoud R. D., Done C., 2018b, MNRAS, 480, 4040
Mishra B., Kluźniak W., Fragile P. C., 2019, MNRAS, in press
Miyamoto S., Kitamoto S., 1989, Nature, 342, 773
Mushtukov A. A., Ingram A., van der Klis M., 2018, MNRAS, 474, 2259
Mushtukov A. A., Lipunova G. V., Ingram A., Tsygankov S. S., Mönkkönen J., van der Klis M., 2019, MNRAS, 486, 4061
Narayan R., Yi I., 1994, ApJ, 428, L13
Narayan R., Yi I., 1995a, ApJ, 444, 231
Narayan R., Yi I., 1995b, ApJ, 452, 710
Narayan R., Mahadevan R., Grindlay J. E., Popham R. G., Gammie C., 1998, ApJ, 492, 554
Narayan R., Igumenshchev I. V., Abramowicz M. A., 2000, ApJ, 539, 798
Narayan R., Sądowski A., Penna R. F., Kulkarni A. K., 2012, MNRAS, 426, 3241
Noble S. C., Krolik J. H., 2009, ApJ, 703, 964
Noble S. C., Gammie C. F., McKinney J. C., Del Zanna L., 2006, ApJ, 641, 626
Nowak M. A., Vaughan B. A., Wilms J., Dove J. B., Begelman M. C., 1999, ApJ, 510, 874
Penna R. F., Kulkarni A., Narayan R., 2013, A&A, 559, A116
Philippov A. A., Rafikov R. R., 2017, ApJ, 837, 101
Porth O. et al., 2019, ApJS, 243, 26
Poutanen J., 2001, Adv. Space Res., 28, 267
Quataert E., Gruzinov A., 2000, ApJ, 539, 809
Rapisarda S., Ingram A., van der Klis M., 2017, MNRAS, 472, 3821
Rees M. J., Begelman M. C., Blandford R. D., Phinney E. S., 1982, Nature, 295, 17
Regev O., Gitelman L., 2002, A&A, 396, 623
Revnivtsev M., Gilfanov M., Churazov E., 2000, A&A, 363, 1013
Reynolds C. S., Miller M. C., 2009, ApJ, 692, 869
Scaringi S. et al., 2015, Sci. Adv., 1, e1500686
Scaringi S., Körding E., Groot P. J., Uttley P., Marsh T., Knigge C., Maccarone T., Dhillon V. S., 2013, MNRAS, 431, 2535
Shakura N. I., Sunyaev R. A., 1973, A&A, 500, 33
Shapiro S. L., Lightman A. P., Eardley D. M., 1976, ApJ, 204, 187
Spiteri R. J., Ruuth S. J., 2002, SIAM J. Numer. Anal., 40, 469
Stone J. M., Tomida K., White C. J., Felker K. G., 2020, ApJS, 249, 4

Thorne K. S., Price R. H., 1975, ApJ, 195, L101
Urpin V. A., 1984, Sov. Ast., 28, 50
Uttley P., McHardy I. M., 2001, MNRAS, 323, L26
Uttley P., McHardy I. M., Vaughan S., 2005, MNRAS, 359, 345
Uttley P., Cackett E. M., Fabian A. C., Kara E., Wilkins D. R., 2014, A&AR, 22, 72
Van de Sande M., Scaringi S., Knigge C., 2015, MNRAS, 448, 2430
van der Klis M., 1995, in Lewin W. H. G., van Paradijs J., van den Heuvel E. P. J., eds, X-ray Binaries, Cambridge Univ. Press, Cambridge, p. 252
Vaughan B. A., Nowak M. A., 1997, ApJ, 474, L43
Wellons S., Zhu Y., Psaltis D., Narayan R., McClintock J. E., 2014, ApJ, 785, 142
White C. J., Stone J. M., Gammie C. F., 2016, ApJS, 225, 22
White C. J., Quataert E., Gammie C. F., 2020, ApJ, 891, 63
Wijnands R., van der Klis M., 1999, ApJ, 514, 939
Wilkinson T., Uttley P., 2009, MNRAS, 397, 666
Yuan F., Narayan R., 2014, ARA&A, 52, 529

APPENDIX A: DETAILS OF SIMULATION D

This simulation is performed using a spherical-polar grid with the computational domain extending from 1.8 to $80^{1.5}\, r_g$ in the radial direction. We set small cut-outs near the poles with $\theta \in [0.02\pi, 0.98\pi]$ to keep the time-step reasonable. In the azimuthal direction, we simulate only a $\pi/2$ wedge. We use logarithmic spacing in the radial direction of the form

$$x_1 = 1 + \ln\left(\frac{r}{r_H}\right) . \tag{A1}$$

In the polar direction, we chose θ of the form (McKinney 2006)

$$\theta = x_2 + \frac{1}{2}[1 - q]\sin(2x_2) , \tag{A2}$$

where the parameter q (set to 0.5) determines the concentration of grid zones near the equator. We set outflow boundary conditions (copying scalar fields to ghost zones, while ensuring the velocity component normal to the boundary points outward) at the inner and outer edges of the domain in both the radial and poloidal directions. We use periodic boundary conditions in the ϕ-direction.

We set the poloidal magnetic field by using a purely azimuthal vector potential of the form

$$A_\phi = S\left(\frac{\rho}{u^t\sqrt{-g}} - 0.2\rho_{max}\right)^2 \sin\left[2\log\left(\frac{r}{1.1r_{in}}\right)\right] , \tag{A3}$$

where $S = 1$ if $\theta < \pi$ and $S = -1$ if $\theta > \pi$; ρ_{max} is the maximum density of the torus, located at r_{max}; r_{in} is the inner edge of the torus; and u^t is the time component of the four-velocity.

The COSMOS++ code uses an explicit five-stage, strong-stability-preserving Runge–Kutta time integration scheme (Spiteri & Ruuth 2002), set to third order. Conserved variables are updated at each time-step using the high-resolution shock-capturing (HRSC) method. The reconstruction of the primitive variables at different spatial locations is done through piecewise parabolic method (PPM) interpolation with a monotonized central limiter (Colella & Woodward 1984). This is followed by the calculation of flux terms at the zone faces using the Harten–Lax–van Leer (HLL) Riemann solver. In order to maintain a divergence-free magnetic field during the evolution, we use the staggered, constrained transport scheme described in Fragile et al. (2012). For the primitive inversion step, we primarily use the '2D' solver from Noble et al. (2006), with a 5D numerical inversion scheme as a backup. In cases where both solvers fail, we use the entropy instead of the conserved energy to recover the primitive variables.
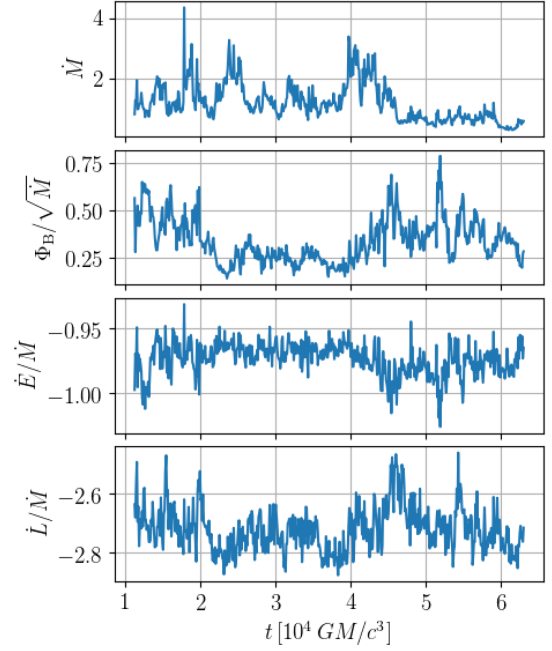
Figure A1. Evolution of mass accretion rate (arbitrary units; top panel), magnetic flux (second panel), energy flux (third panel), and angular momentum flux (bottom panel) through the horizon for simulation D.

Since this simulation has not been described elsewhere in the literature, we report some basic diagnostics here. First, in Fig. A1, we plot various fluxes through the event horizon. We define the magnetic flux (Φ_B), energy flux ($\dot{E}$), and angular momentum flux ($\dot{L}$) as

$$\Phi_B = \frac{1}{2}\oint |B^r|\sqrt{-g}\,\mathrm{d}\theta\mathrm{d}\phi , \tag{A4}$$

$$\dot{E} = -\oint T^r_t\sqrt{-g}\,\mathrm{d}\theta\mathrm{d}\phi , \tag{A5}$$

$$\dot{L} = \oint T^r_\phi\sqrt{-g}\,\mathrm{d}\theta\mathrm{d}\phi , \tag{A6}$$

where B^r is the radial component of the primitive magnetic field, which is already scaled by the $\sqrt{4\pi}$ factor. T^r_t and T^r_ϕ are components of the stress energy tensor (see equation 4 in Fragile et al. 2012). The modest value of the magnetization parameter, $\Phi_B/\sqrt{\dot{M}}$, throughout the simulation indicates that we maintain a SANE (standard and normal evolution) flow, even though we initiate the simulation with a single poloidal field loop. These fluxes generally agree well with the other simulations, especially R (Narayan et al. 2012). The one exception is that the magnetic flux through the horizon is somewhat lower than the others, likely due to the choice of boundary conditions in COSMOS++ (see, e.g. Porth et al. 2019).

In Fig. A2, we show the azimuthally and time-averaged velocity vectors superimposed on the averaged density. Time averaging is performed for the last $10\,000\,GM/c^3$ period of the simulation. The white dashed line represents the time average of the density scale height. The resulting accretion flow is clearly geometrically thick, with dominant inflow of matter at all latitudes within $\sim 20\,r_g$ unlike simulations A, B, and C that exhibit outflows/convective motions. Beyond this radius, there are signatures of outflows at higher latitudes. Small convective loops can be noticed in some locations. In general, these results are similar to simulation R.
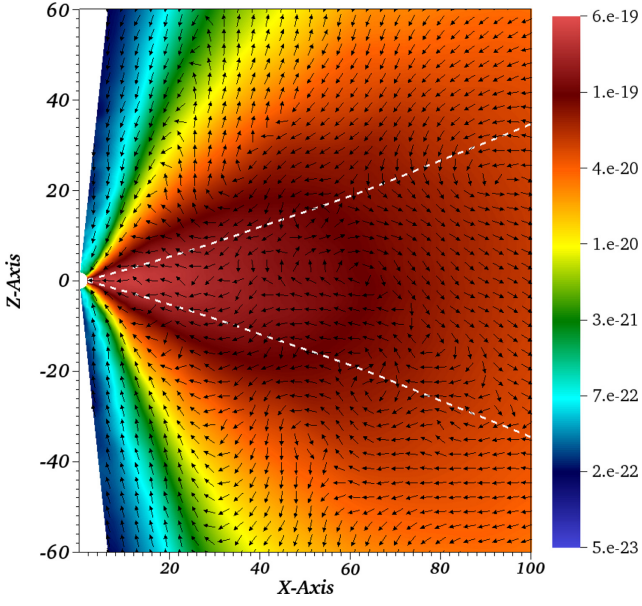
Figure A2. Azimuthally and time-averaged velocity vectors with the background colour representing the similarly averaged density. The white dashed line indicates the time average of the density scale height. Time averaging is done over the last $10\,000\,GM/c^3$ of the simulation.

APPENDIX B: LOGNORMAL DISTRIBUTION FOR FULL $\dot{m}$

In Section 4.5, we analysed histograms of $\dot{m}$ selected for periods when the mean accretion rate was reasonably constant. Here we repeat the analysis for the full distribution of $\dot{m}$ for every simulation, excluding the discarded initial transient data (see Fig. 1). Fig. B1 shows the resulting histograms. In the top panels, we show the distribution for the original $\dot{m}$ data, with the best fits for normal and lognormal distributions shown in red dashed and blue solid curves, respectively. We find that, except for simulation D, none of the fits have a statistically significant χ^2/d.o.f. value (see Table B1). To test whether subtracting off a simple exponential fit to the raw $\dot{m}$ could improve the fit, we also present histograms of $\dot{m}_{\rm cor}$ in the bottom panel of Fig. B1. Best-fitting parameters for all the distributions are provided in Table B1, along with the respective χ^2/d.o.f. values for the fits. Although the fits for $\dot{m}_{\rm cor}$ do show smaller χ^2/d.o.f. values, they are still not statistically acceptable. We re-emphasize though that Fig. 15 and Table 3 show that whenever $\dot{m}$ oscillates around a time-steady mean, the fluctuations *are* well fit by a lognormal distribution.
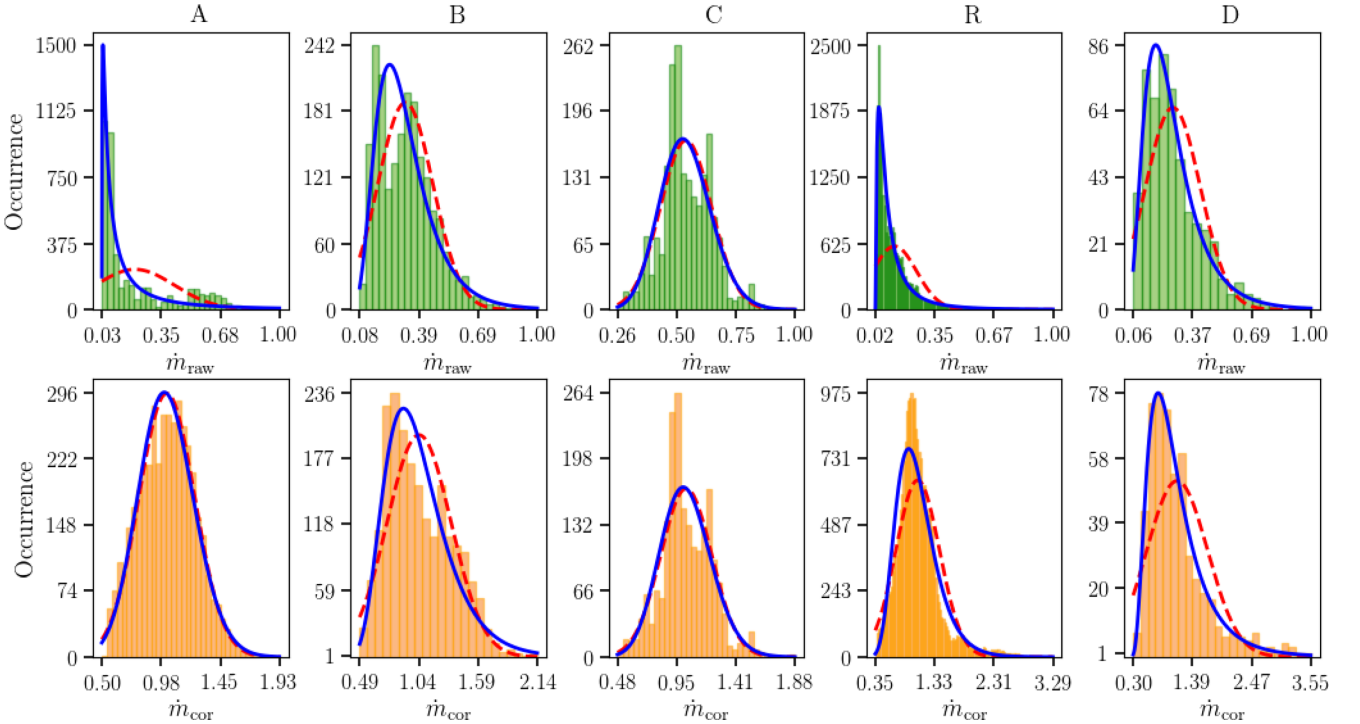
Figure B1. Histograms of the normalized accretion rate ($\dot{m}$) at the horizon ($r_{\rm H}$) for all five simulations. Top panels: histograms for the uncorrected $\dot{m}$. Bottom panels: same for the corrected accretion rates, $\dot{m}_{\rm cor}$. Best-fitting normal and lognormal distributions are shown in red dashed and blue solid curves, respectively.

Table B1. Parameters for the normal and lognormal fits to the mass flux histograms in Fig. B1.

Simulation		Normal			Lognormal			
		μ	σ	χ^2/d.o.f.	μ	σ	τ	χ^2/d.o.f.
A	$\dot{m}$	0.21	0.22	9880.4/30	-2.64	1.57	0.03	2067.1/29
	$\dot{m}_{cor}$	1.03	0.22	117.8/33	1.32	0.06	-2.72	127.3/32
B	$\dot{m}$	0.32	0.14	1632.3/25	-1.19	0.43	-0.01	216.2/24
	$\dot{m}_{cor}$	1.04	0.30	281.5/20	-0.22	0.35	0.19	150.3/19
C	$\dot{m}$	0.54	0.11	509.1/31	0.24	0.08	-0.74	368.1/30
	$\dot{m}_{cor}$	1.02	0.20	491.4/31	0.93	0.08	-1.51	351.7/30
R	$\dot{m}$	0.13	0.12	532 778 977.8/122	-2.77	1.07	0.02	1288.5/121
	$\dot{m}_{cor}$	1.05	0.36	729 349.7/113	0.02	0.31	-0.02	6454.4/112
D	$\dot{m}$	0.27	0.14	2353.8/18	-1.4	0.52	-0.01	19.1/17
	$\dot{m}_{cor}$	1.11	0.55	792.8/21	-0.27	0.57	0.21	25.8/20

This paper has been typeset from a TeX/LaTeX file prepared by the author.